



HAL
open science

Structural characterization of thin non-crystalline layers for low thermal noise optic

Élodie Coillet

► **To cite this version:**

Élodie Coillet. Structural characterization of thin non-crystalline layers for low thermal noise optic. Optics [physics.optics]. Université de Lyon, 2017. English. NNT : 2017LYSE1132 . tel-01626513

HAL Id: tel-01626513

<https://theses.hal.science/tel-01626513>

Submitted on 30 Oct 2017

HAL is a multi-disciplinary open access archive for the deposit and dissemination of scientific research documents, whether they are published or not. The documents may come from teaching and research institutions in France or abroad, or from public or private research centers.

L'archive ouverte pluridisciplinaire **HAL**, est destinée au dépôt et à la diffusion de documents scientifiques de niveau recherche, publiés ou non, émanant des établissements d'enseignement et de recherche français ou étrangers, des laboratoires publics ou privés.



N° d'ordre NNT : xxx

THÈSE DE DOCTORAT DE L'UNIVERSITÉ DE LYON

opérée au sein de

l'Université Claude Bernard Lyon 1

École Doctorale ED52

Physique et Astrophysique de Lyon

Spécialité de doctorat : Physique

Soutenue publiquement le 20/07/2017, par :

Elodie Coillet

Structural characterization of thin non-crystalline layers for low thermal noise optic

(Caractérisations structurales de couches minces vitreuses pour
l'optique à bas bruit thermique)

Devant le jury composé de :

Boukenter Aziz, Professeur, Université Jean Monnet Saint Étienne

Faivre Annelise, Professeure, Université Montpellier II

Canepa Maurizio, Professeur, Università degli Studi di Genova

Ollier Nadège, Ingénieure-Chercheur, École Polytechnique

Cagnoli Gianpietro, Professeur, Université Claude Bernard Lyon 1

Rapporteur

Rapporteuse

Examineur

Examinatrice

Examineur

Mermet Alain, Professeur, Université Claude Bernard Lyon 1

Martinez Valérie, Maître de Conférences, Université Claude Bernard Lyon 1

Directeur de thèse

Co-directrice de thèse

UNIVERSITE CLAUDE BERNARD - LYON 1

Président de l'Université

Président du Conseil Académique

Vice-président du Conseil d'Administration

Vice-président du Conseil Formation et Vie Universitaire

Vice-président de la Commission Recherche

Directrice Générale des Services

M. le Professeur Frédéric FLEURY

M. le Professeur Hamda BEN HADID

M. le Professeur Didier REVEL

M. le Professeur Philippe CHEVALIER

M. Fabrice VALLÉE

Mme Dominique MARCHAND

COMPOSANTES SANTE

Faculté de Médecine Lyon Est - Claude Bernard

Faculté de Médecine et de Maïeutique Lyon Sud - Charles
Mérieux

Faculté d'Odontologie

Institut des Sciences Pharmaceutiques et Biologiques

Institut des Sciences et Techniques de la Réadaptation

Département de formation et Centre de Recherche en Bi-
ologie Humaine

Directeur : M. le Professeur G. RODE

Directeur : Mme la Professeure C.
BURILLON

Directeur : M. le Professeur D.
BOURGEOIS

Directeur : Mme la Professeure C.
VINCIGUERRA

Directeur : M. X. PERROT

Directeur : Mme la Professeure A-M.
SCHOTT

COMPOSANTES ET DEPARTEMENTS DE SCIENCES ET TECHNOLOGIE

Faculté des Sciences et Technologies

Département Biologie

Département Chimie Biochimie

Département GEP

Département Informatique

Département Mathématiques

Département Mécanique

Département Physique

UFR Sciences et Techniques des Activités Physiques et
Sportives

Observatoire des Sciences de l'Univers de Lyon

Polytech Lyon

Ecole Supérieure de Chimie Physique Electronique

Institut Universitaire de Technologie de Lyon 1

Ecole Supérieure du Professorat et de l'Education

Institut de Science Financière et d'Assurances

Directeur : M. F. DE MARCHI

Directeur : M. le Professeur F.
THEVENARD

Directeur : Mme C. FELIX

Directeur : M. Hassan HAMMOURI

Directeur : M. le Professeur S. AKKOUCHE

Directeur : M. le Professeur G. TOMANOV

Directeur : M. le Professeur H. BEN
HADID

Directeur : M. le Professeur J.C. PLENET

Directeur : M. Y. VANPOULLE

Directeur : M. B. GUIDERDONI

Directeur : M. le Professeur E. PERRIN

Directeur : M. G. PIGNAULT

Directeur : M. le Professeur C. VITON

Directeur : M. le Professeur A.
MOUGNIOTTE

Directeur : M. N. LEBOISNE

Contents

Symbols and abbreviations	1
Introduction	3
Bibliography	9
1 Theory and Experiments	13
1.1 Non-crystalline solids	13
1.1.1 Definition	13
1.1.2 Fabrication processes	16
1.2 Deposition process	16
1.3 Mechanical losses	19
1.3.1 Theory	19
1.3.2 Mechanical losses measurements	21
1.4 Vibrational Spectroscopies	23
1.4.1 Physical principles	23
1.4.2 Raman spectroscopy	26
1.4.3 Brillouin spectroscopy	30
1.4.4 Infrared spectroscopy	33
1.4.5 Conclusion	37
1.5 High pressure measurements	38
1.6 Rutherford Backscattering Spectroscopy	40
1.7 Conclusion	43
Bibliography	45
2 Silica glass	49
2.1 Silica Glass structure	49
2.1.1 Molecular structure	49
2.1.2 Comparison between fused silica and Ion-Beam sputtered thin layers	53

2.2	Effects of the processing method	57
2.2.1	Interaction between substrates and silica layers	57
2.2.2	Deposition parameters effects	59
2.3	Effect of the annealing on the structure	64
2.3.1	Annealing of a Spector sample	64
2.3.2	Annealing of a Grand Coater sample	73
2.3.3	Conclusion on the general effect of the annealing	78
2.4	Conclusion	79
Bibliography		81
3	Tantalum pentoxide	87
3.1	Crystalline and amorphous structure	87
3.2	Annealing	94
3.2.1	Evolution with annealing time	94
3.2.2	Evolution with temperature of annealing	96
3.3	Reference Ta ₂ O ₅	98
3.3.1	Fused Ta ₂ O ₅	98
3.3.2	Thick Ion Beam Sputtered sample	99
3.4	High pressure study	102
3.4.1	Structural evolution by Raman and Brillouin spectroscopy	102
3.5	TiO ₂ doping	111
3.5.1	Structure	111
3.5.2	Doping effect	115
3.6	Conclusion	123
Bibliography		125
Conclusion		131
Bibliography		133
A	Band analysis	135
A.1	Silica glass spectra	135
A.2	Amorphous Tantalum oxide spectra	135

Symbols and abbreviations

AdV	Advanced Virgo
ATR-FTIR	Attenuated Total Reflection Fourier Transform Infrared
DAC	Diamond Anvil Cell
D_1, D_2	Defects bands in Silica Raman spectra
DWP	Double Well Potential
EXAFS	Extended X-ray absorption fine structure
FP	Fabry-Pérot cavity
GC	Grand Coater deposition chamber
GeNS	Gentle Nodal Suspension system
GW	Gravitational Wave
HWHM	Half Width at Half Maximum
IBS	Ion Beam Sputtering
LIGO	Laser Interferometer Gravitational-wave Observatory
MB	Main Band
PVD	Physical Vapor Deposition
RBS	Rutherford Backscattering
TLS	Two-Level System
VDOS	Vibrational Density of States
XANES	X-ray absorption near edge structure
a	Crystalline cell parameter
c, c_n	Speed of light in vacuum and in a material
C_{11}, C_{44}	Elastic coefficients
D	Dilution factor
d_p	penetration depth
Δ	Energy difference between the two minima of a DWP
e	Layers thickness
E, E_0	Electric field and its amplitude
E_i	Energy
F	Finesse of a Fabry-Pérot cavity
$g(\omega)$	Vibrational density of states
$h = 2\pi\hbar$	Planck constant

$I(\omega)$	Scattering intensity
k	Wave-vector
k_B	Boltzmann constant
λ	Wavelength
M	Molar Mass
m_i, M_i	Masses
μ	reduced mass
NA	Numerical Aperture
N_A	Avogadro's number
n	Refractive index
N	Atoms number
$n(\omega)$	Bose-Einstein factor
ν_k	Resonant frequency of a disk shaped resonator
ω	Angular frequency
Ω	Phonon angular frequency
p	Pressure
P	Polarizability
q	Phonon wave-vector
φ	Loss angle (mechanical losses)
Q	Quality factor
R	Reflectivity
ρ	Density
S_{xx}	Thermal noise power spectral density
t	Time
T	Transmission
T_{fus}	Melting temperature
T_g	Glass-transition temperature
T_a	Annealing temperature
τ	Characteristic time of evolution
θ	Scattering angle
V	Height of the barrier in an asymmetric double well potential
$V_{L/T}$	Longitudinal and Transverse speed of sound
V_i	Particle's velocity
χ	Dielectric susceptibility tensor
Y	Young modulus

Introduction

Einstein predicted the existence of gravitational waves in 1916, as solutions to the field equations of the general relativity [Einstein, 1916, Einstein, 1918] .

Following the theory of General Relativity, the space-time becomes a deformable media: mass (or energy) can alter the metric of the space-time, affecting then the trajectories of massive particles, as well as massless ones, like photons. In this media, perturbations respect the classical equation of waves where the speed is equal to the speed of light. These propagating perturbations of space-time are called Gravitational Waves (GW). GW of sufficient amplitude to be detected may come from coalescence of compact binaries, like neutron stars and black holes, asymmetric explosion of supernovae, pulsars instabilities and cosmic GW background created during the inflation epoch. The detection of GW represents the ultimate test of General Relativity and the beginning of a new type of astronomy based on the GW probe, that will be complementary of the traditional electromagnetic one. Indeed, each gravitational wave contains information on the event it originates from, added to information on the nature of gravity.

The indirect proof of the existence of GW was found by [Hulse and Taylor, 1975, Taylor and Weisberg, 1982], with the discovery of a binary pulsar which is the exact kind of system supposed to emit gravitational waves. Via the measurements of the period of the stars orbits which changes over time, they found that they were getting closer, exactly as predicted by Einstein's theory of general relativity, which indirectly proved the existence of GW.

One hundred years after the predictions of Einstein, the LIGO collaboration associated with the VIRGO collaboration announced the first direct detection of a GW. On September 14, 2015, the two LIGO detectors observed the passing of a gravitational wave corresponding to the merging of two black holes, approximately 1.3 billion light-years away [Abbott et al., 2016b]. Two more signals were detected later, originating from smaller mass binaries, the last one being further away than the two initial detections. The three signals are presented on figure 0.1.

Different kinds of GW detectors have been proposed: pulsar timing arrays is operating in the extremely low frequency band; space-based detectors like LISA are still in the phase of development; and ground based interferometers using laser interferometry, which are the ones that detected the signals. In figure 0.2, the sensitivity curves of

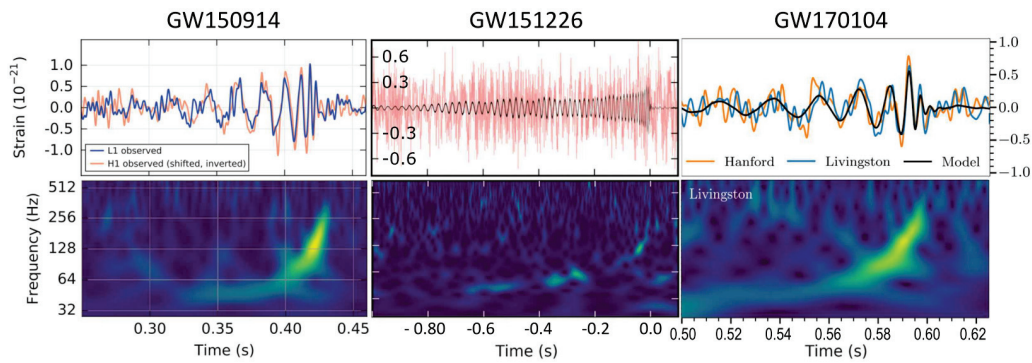


Figure 0.1 – Gravitational Wave signals detected so far. At left the first ever detected signal GW150914. In the upper plot the signals detected from the two LIGO detectors at Hanford and Livingston are shown. For the second signal GW151226, at center, only the signal from Hanford is represented. The right plot corresponds to the last signal detected, GW170104, with both Handford and Livingston signals represented. In the lower plots one can see how the energy of the signal is distributed on frequency for each detection.

the different type of detectors are represented as a function of frequency. The detectors we are interested in are the ground based interferometers, operating between 10^1 Hz and 10^4 Hz. In this band, GW signals come from the merging phase of compact objects binaries, core collapse of supernovae and pulsars. These detectors cannot measure low frequency signals as there is too much noise on Earth (seismic noise and gravity gradient noise).

The interferometric detectors design was first proposed in the 1960s and 1970s [Gertsenshtein and Pustovoit, 1963, Moss et al., 1971]. The actual detectors, such as advanced LIGO and advanced Virgo, rely on a modified Michelson interferometer setup. As a gravitational wave pass through them, it creates a difference in length of the two orthogonal arms which can be detected.

Figure 0.3 presents a schematic view of the advanced Virgo (AdV) detector. Each arm is 3 km long, with test mass mirrors at each end creating a resonant optical cavity in which the light travels approximately 100 km before exiting. Cavities are illuminated by a Nd:YAG laser operating at 1064 nm, and a power-recycling mirror at the input allows to reach 4.9 kW on the beam splitter and 650 kW in the cavities (assuming 125 W of input power).

At present, as shown on figure 0.4, one of the major sensitivity limitation of the GW detectors comes from the coating Brownian noise of the test-mass mirrors, in the 30-500 Hz region, which is the most sensitive band of the interferometers. This thermal noise is directly linked to the mechanical losses (the internal friction, Q^{-1}) via the fluctuation-

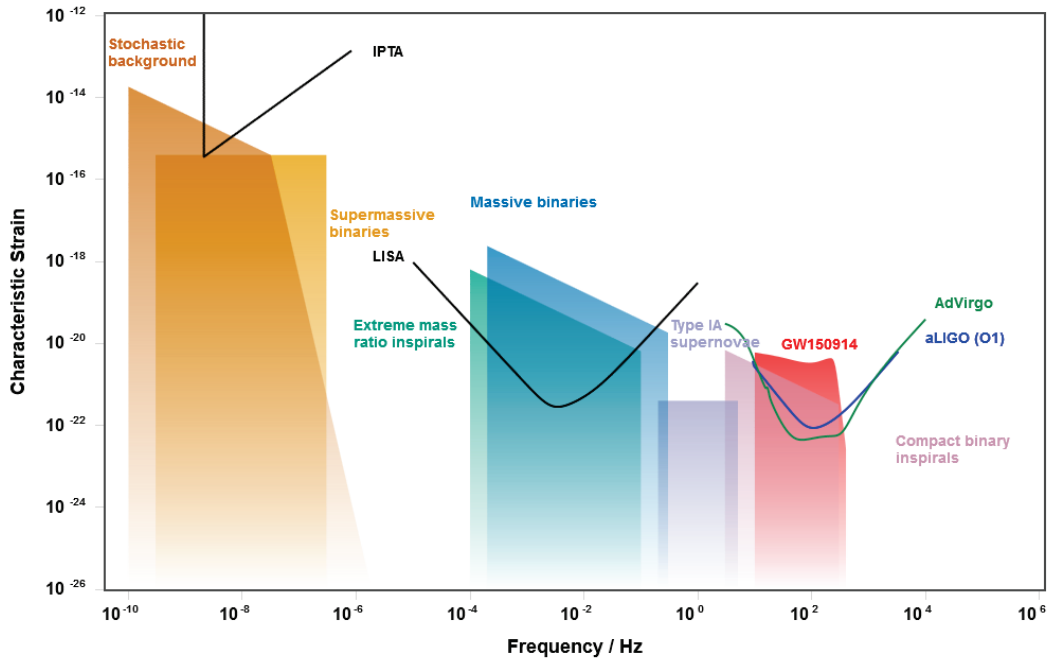


Figure 0.2 – Different gravitational wave detectors frequency range of detection with the events we expect to see at these frequencies [Moore et al., 2015]. At low frequency, the International Pulsar Timing Array (IPTA) can detect super-massive binaries and the stochastic background. The LISA pathfinder project aims the detection of massive events, like extreme mass ratio inspirals, massive binaries during merging, or any compact objects binaries far from the merging phase. The advanced Virgo and LIGO collaborations detect higher frequencies, i.e. smaller events like GW150914, the merging of two black holes detected by the LIGO interferometers in september 2015 [Abbott et al., 2016b].

dissipation theorem [Saulson, 1990]. Thermal noise is also one of the ultimate limiting factors to improve technologies such as quantum computing [Martinis et al., 2005], optomechanics [Kippenberg and Vahala, 2007], or frequency standards [Notcutt et al., 2006].

The mirrors forming the Fabry-Perot cavities are Bragg mirrors composed of alternating thin films made of amorphous SiO_2 as low-index material, and TiO_2 -doped Ta_2O_5 as high-index material. These coatings are deposited by Ion Beam Sputtering (IBS) on a fused silica substrate and the oxides were chosen mainly for their low absorption properties at 1064 nm and thermal noise level [Beauville et al., 2004, Harry et al., 2007]. After the deposition process, the mirrors are annealed to release the stress induced by the IBS process, lower the absorption and decrease the thermal noise [Granata et al., 2016].

Thermal noise arises from random relaxation processes that distribute the thermal

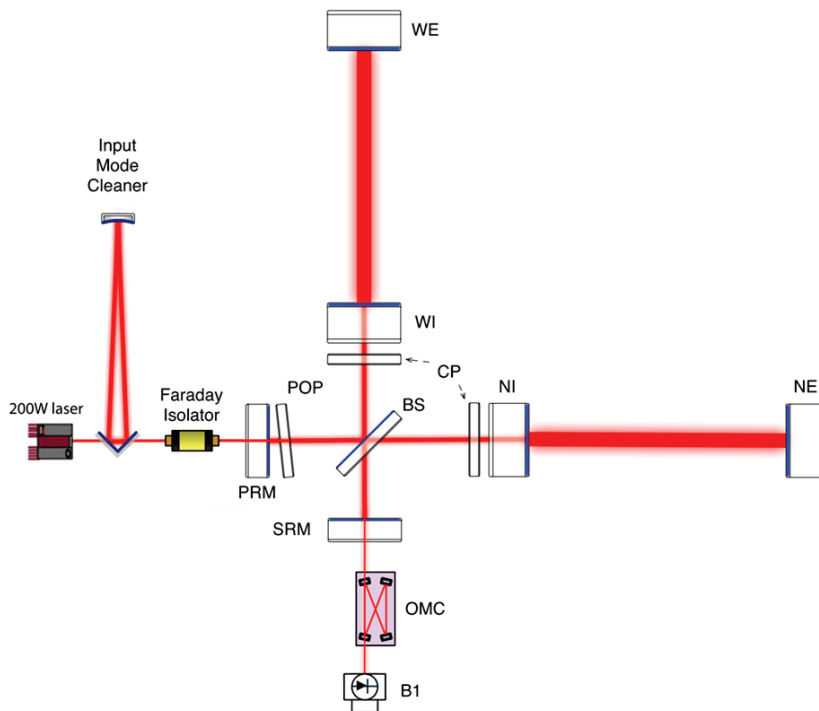


Figure 0.3 – Optical layout of Advanced Virgo. In order to increase the sensitivity to displacements, the traditional Michelson interferometer has been modified installing two Fabry-Perot cavities along the arms, with finesse around 440. The two input mirrors, WI and NI for the West and North arm respectively, and the end mirrors, WE and NE, form the set of test masses that sense the passage of a GW signals. Details of the interferometer can be found in [Acernese et al., 2015].

energy of the atoms over all frequencies. In non-crystalline materials, the features of these unknown relaxations processes are fairly well explained by two-level systems (TLS), with transitions thermally activated at ambient temperature [Gilroy and Phillips, 1981]. However, no model explains why fused silica presents losses about four orders of magnitude lower than any other non-crystalline materials at room temperature, or why amorphous Silicon evaporated by e-beam on a high temperature substrate (400 °C) has mechanical losses approximately three orders of magnitude lower than other materials at cryogenic temperatures (represented on figure 0.5). The required maximum limit for the thermal noise of the future Gravitational Wave Detectors corresponds to the green dashed line, the TiO₂-doped Ta₂O₅ and IBS-Silica composing the mirrors being at present higher than this limit.

In order to understand the structural origin of the losses in the optical coatings, we carried out an extensive study of the layers structures probed by vibrational spectroscopies, looking for possible correlations between energy dissipation and structures.

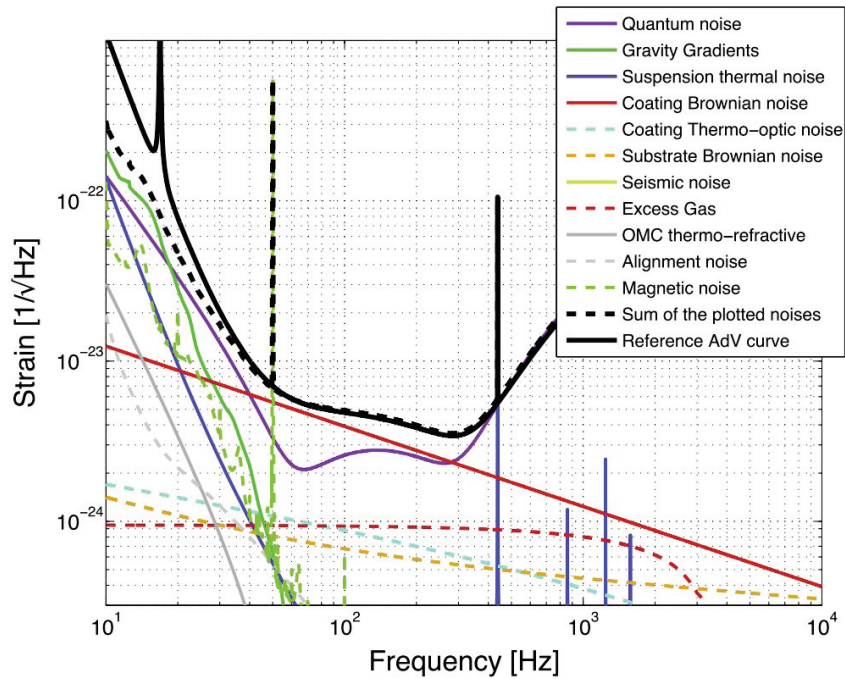


Figure 0.4 – Sensitivity limits for the AdV detector with noise sources [Acernese et al., 2015].

The first Chapter will present the structure and fabrication processes of non-crystalline solids. Along this presentation of the material at stake, the different parameters of interest and analysis techniques used will be described. In a second Chapter, the structure of the silica coatings will be discussed compared to fused silica. Then, the effect of the deposition technique and of the post-deposition annealing of this structure will be investigated. Besides the SiO_2 measurements, a similar study on Ta_2O_5 will be presented in the third Chapter with the effect of annealing. To pursue the characterization of this oxide, an analysis of the structural evolution of its structure under isotropic pressure was conducted. The effects of the titanium oxide doping on the structure of the Ta_2O_5 will also be discussed.

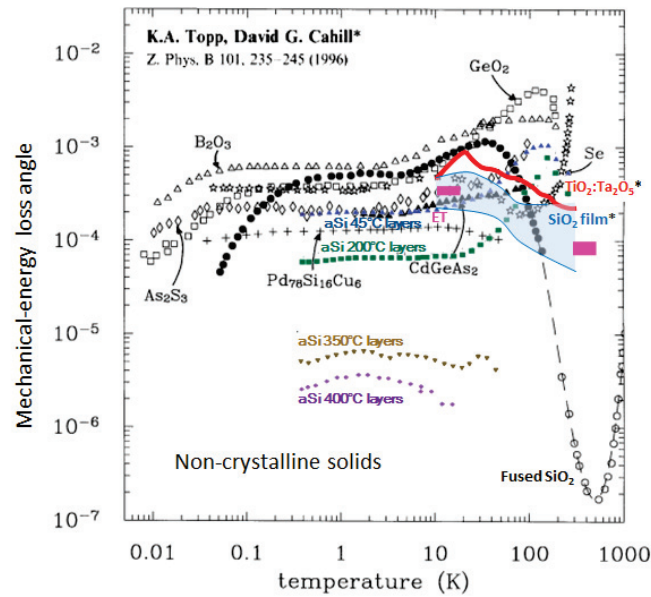


Figure 0.5 – Mechanical loss angle of different amorphous materials measured over a wide range of temperature and from a few kHz to a few MHz [Topp and Cahill, 1996]. The amorphous silicon mechanical losses were added for comparison, the temperatures corresponding to the substrate temperature during deposition. The values corresponding to the mirrors coatings are in red for the TiO_2 -doped Ta_2O_5 and in blue for silica layers. The pink lines are the Einstein Telescope requirements, corresponding to the maximum losses limit required for the next gravitational wave detectors generation.

Bibliography

- [Abbott et al., 2016a] Abbott, B., Abbott, R., Abbott, T., Abernathy, M., Acernese, F., Ackley, K., Adams, C., Adams, T., Addesso, P., Adhikari, R., et al. (2016a). GW151226: Observation of gravitational waves from a 22-solar-mass binary black hole coalescence. *Physical Review Letters*, 116(24):241103.
- [Abbott et al., 2016b] Abbott, B. P., Abbott, R., Abbott, T., Abernathy, M., Acernese, F., Ackley, K., Adams, C., Adams, T., Addesso, P., Adhikari, R., et al. (2016b). Observation of gravitational waves from a binary black hole merger. *Physical review letters*, 116(6):061102.
- [Acernese et al., 2015] Acernese, F., Agathos, M., Agatsuma, K., Aisa, D., Allemandou, N., Allocca, A., Amarni, J., Astone, P., Balestri, G., et al. (2015). Advanced VIRGO: a second-generation interferometric gravitational wave detector. *Classical and Quantum Gravity*, 32(2):024001.
- [Beauville et al., 2004] Beauville, F., Buskulic, D., Flaminio, R., Marion, F., Masserot, A., Massonnet, L., Mours, B., Moreau, F., Ramonet, J., Tournefier, E., et al. (2004). The VIRGO large mirrors: a challenge for low loss coatings. *Classical and Quantum Gravity*, 21(5):S935.
- [Einstein, 1916] Einstein, A. (1916). Approximative integration of the field equations of gravitation. *Sitzungsberichte der Koniglich Preussischen Akademie der Wissenschaften*, 1916:688–696.
- [Einstein, 1918] Einstein, A. (1918). Concerning gravitational waves. *Sitzungsberichte der Koniglich Preussischen Akademie der Wissenschaften*, 1:154–67.
- [Gertsenshtein and Pustovoit, 1963] Gertsenshtein, M. and Pustovoit, V. (1963). On the detection of low frequency gravitational waves. *Soviet Physics JETP*, 16(2):433–435.
- [Gilroy and Phillips, 1981] Gilroy, K. S. and Phillips, W. A. (1981). An asymmetric double-well potential model for structural relaxation processes in amorphous materials. *Philosophical Magazine B*, 43(5):735–746.

- [Granata et al., 2016] Granata, M., Saracco, E., Morgado, N., Cajgfinger, A., Cagnoli, G., Degallaix, J., Dolique, V., Forest, D., Franc, J., Michel, C., et al. (2016). Mechanical loss in state-of-the-art amorphous optical coatings. *Physical Review D*, 93(1):012007.
- [Harry et al., 2007] Harry, G. M., Abernathy, M. R., Becerra-Toledo, A. E., Armandula, H., Black, E., Dooley, K., Eichenfield, M., Nwabugwu, C., Villar, A., Crooks, D. R. M., Cagnoli, G., Hough, J., How, C. R., MacLaren, I., Murray, P., Reid, S., Rowan, S., Sneddon, P. H., Fejer, M. M., Route, R., Penn, S. D., Ganau, P., Mackowski, J.-M., Michel, C., Pinard, L., and Remillieux, A. (2007). Titania-doped tantala/silica coatings for gravitational-wave detection. *Classical and Quantum Gravity*, 24(2):405.
- [Hulse and Taylor, 1975] Hulse, R. A. and Taylor, J. H. (1975). Discovery of a pulsar in a binary system. *Astrophys J.*, 195:L51–L53.
- [Kippenberg and Vahala, 2007] Kippenberg, T. J. and Vahala, K. J. (2007). Cavity optomechanics. *Optics Express*, 15(25):17172–17205.
- [Liu et al., 2014] Liu, X., Queen, D. R., Metcalf, T. H., Karel, J. E., and Hellman, F. (2014). Hydrogen-free amorphous silicon with no tunneling states. *Phys. Rev. Lett.*, 113:025503.
- [Martinis et al., 2005] Martinis, J. M., Cooper, K., McDermott, R., Steffen, M., Ansmann, M., Osborn, K., Cicak, K., Oh, S., Pappas, D., Simmonds, R., et al. (2005). Decoherence in josephson qubits from dielectric loss. *Physical Review Letters*, 95(21):210503.
- [Moore et al., 2015] Moore, C. J., Cole, R. H., and Berry, C. P. L. (2015). Gravitational-wave sensitivity curves. *Classical and Quantum Gravity*, 32(1):015014.
- [Moss et al., 1971] Moss, G., Miller, L., and Forward, R. (1971). Photon-noise-limited laser transducer for gravitational antenna. *Applied Optics*, 10(11):2495–2498.
- [Notcutt et al., 2006] Notcutt, M., Ma, L.-S., Ludlow, A. D., Foreman, S. M., Ye, J., and Hall, J. L. (2006). Contribution of thermal noise to frequency stability of rigid optical cavity via hertz-linewidth lasers. *Physical Review A*, 73(3):031804.
- [Saulson, 1990] Saulson, P. R. (1990). Thermal noise in mechanical experiments. *Physical Review D - Particles and Fields*, 42(8):2437–2445.
- [Taylor and Weisberg, 1982] Taylor, J. H. and Weisberg, J. M. (1982). A new test of general relativity-Gravitational radiation and the binary pulsar PSR 1913+ 16. *The Astrophysical Journal*, 253:908–920.

[Topp and Cahill, 1996] Topp, K. A. and Cahill, D. G. (1996). Elastic properties of several amorphous solids and disordered crystals below 100 K. *Zeitschrift für Physik B*, 101:235–245.

Chapter 1

Theory and Experiments

The mirrors of the gravitational wave detectors are composed of non-crystalline oxide thin layers deposited on fused silica. This chapter will first present the properties and structures of non-crystalline solids, before describing the samples and their fabrication process. Then, the link between the mechanical losses and the thermal noise will be investigated along the experimental techniques to measure this parameter. The vibrational spectroscopic theory and experimental setup will be described, as well as how high pressure measurements can be done to explore the structure under extreme conditions. Finally, Rutherford Backscattering spectroscopy will be presented, as it allows the quantitative estimation of the elements present in thin layers.

1.1 Non-crystalline solids

1.1.1 Definition

Solids with no periodicity and symmetry in their structure (no long-range order) are defined as non-crystalline solids. They can be divided in two categories : glasses and amorphous solids, as described as follows [Zarzycki, 1982, Zachariasen, 1932].

Glasses

Zarzycki defined a glass as a non-crystalline solid presenting the glass transition temperature phenomenon [Zarzycki, 1982]. When a liquid is cooled, a phase transition happens at the solidification temperature from the liquid state to the crystalline state. This transition is characterized by a discontinuity in the specific volume of the material. To reach a glassy state, crystallization, which is thermodynamically favored, should be avoided. For certain liquids with an initial temperature higher than the melting temperature (T_{fus}), if the cooling rate is high enough, crystallization can be bypassed; this process is called quenching. During cooling, below the melting temperature, the viscosity of the liquid is continuously increasing. The stable liquid then becomes a metastable

super-cooled liquid down to the glass transition temperature. At this point, the viscosity reaches 10^{13} Pa.s, corresponding to the glass transition temperature (T_g) area, characteristic of the composition of the sample. Below T_g , the material is a solid while keeping the structure of the liquid. Depending on the cooling rate different structures can be obtained for the same composition. To characterize these structures, the fictive temperature can be defined, associating the structure of the glass to the extrapolated super-cooled liquid state as shown on figure 1.1. A high cooling rate corresponds to a high fictive temperature.

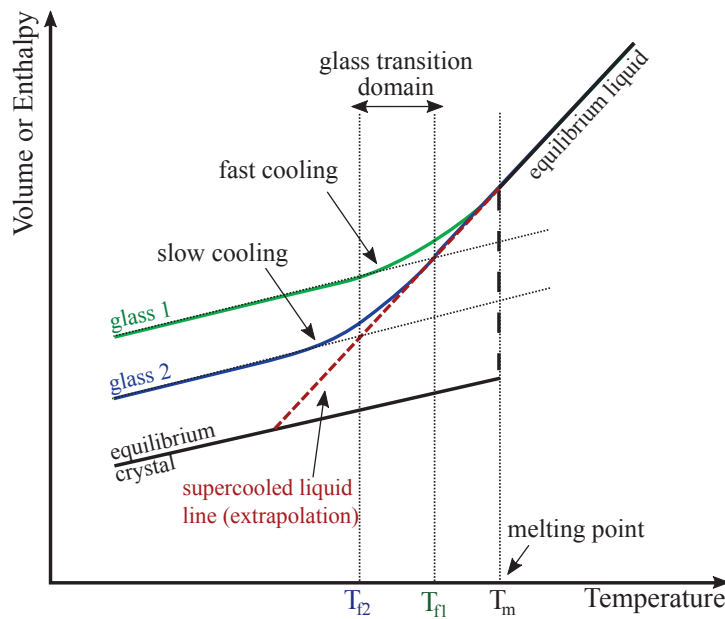


Figure 1.1 – Schematic view of the glass transition for one composition : volume (or enthalpy) as a function of the temperature. Glasses 1 and 2 present two different fictive temperatures depending on their cooling rates. T_m corresponds to the melting point.

Different kinds of chemical elements can form glasses : inorganic oxides (silicon, boron... oxides), halides, chalcogenides, metallic glasses or organic glasses. Most usual glasses are composed of silica (SiO_2) as it is the most commonly found around us.

The formation of a glass depends on its composition and on its cooling rate. Usually, for oxides, the glass components can be divided in three groups : forming, modifier and intermediate glasses. Forming oxides can form glasses by themselves through the melt/quench fabrication process. They present a structure of corner-shared structural motifs based on triangles or tetrahedra. From [Zachariasen, 1932], any oxide forming a glass should satisfy the following rules :

- The number of oxygen atoms surrounding a cation should be small (3 or 4);

- No oxygen can be linked to more than two cations;
- Polyhedra can share apex, but never share edges or faces;
- At least three apex of each polyhedra should be shared with other polyhedra.

Network modifiers don't form a glass under classic conditions, but can be introduced in multi-component systems to modify their properties. They can depolymerize the network. Intermediate oxides, depending on the structure around them and the proportion of the different components of the glass, act either as forming oxide or modifiers. However, with the technological progresses of the last few years, this definition can be nuanced as glasses with only intermediate and modifiers oxides were successfully processed [Neuville et al., 2010]. Glasses can also be obtained through other fabrication processes, but they need to present the glass transition temperature phenomenon to be called glasses.

Amorphous solids

By opposition to glasses, an amorphous solid does not present the glass transition phenomenon [Zarzycki, 1982]. The amorphous structure is not as stable as a glass. One way to differentiate an amorphous solid from a glass is to heat it. When heated, the structure of a glass is slowly softening towards a more liquid state. On the opposite, an amorphous solid, when heated, crystallizes before reaching the melting temperature due to a less stable structure compared to glass.

Structures

As previously stated, non-crystalline solids lack long-range order. However, their structure presents a short and medium range order which can be characterized. At short range (from 1 to 5 Å), corresponding to the basic structural units of the material, the structure is composed of polyhedra defined by their coordination number, their bond lengths, and angles inside these polyhedra. The medium range order (from 5 Å to 20 Å) corresponds to the arrangement of the polyhedra between themselves and can be decomposed in three ranges [Elliott, 1992]. Around 5 Å, this order is characterized by the inter-polyhedral angles. In the case of glasses, polyhedra are only linked by their vertex, but they can be linked by edges or faces in the case of amorphous solids. Between 5 and 8 Å, polyhedra can organize themselves in bigger items to form cycles for example. At longer range, between 5 Å and 20 Å, polyhedra can form chain-like structures, or repeated structural motifs.

1.1.2 Fabrication processes

The most common way to produce a glass is by the melt-quench process. The compounds are heated up to a temperature higher than the melting point, then quenching allows the freezing of the structure of the liquid.

Certain fabrication processes allow the production of thin layers, like vapor deposition processes or sol-gel techniques. In the chemical vapor deposition (CVD) processes, the substrate is exposed to gaseous precursors which react or decompose to obtain a thin film. Physical vapor deposition corresponds to the vacuum deposition on a substrate of a flux of atoms (or molecules). This flux can correspond for example to sputtered particles extracted from a target by an ion beam (Ion Beam Sputtering), an intense laser beam (Pulsed Laser Ablation), evaporated atoms (Molecular Beam Epitaxy) or vaporized atoms by a strong current (Arc-PVD). These techniques usually process highly stressed materials [Pauleau, 2001, Obraztsov et al., 2007, Ager III and Drory, 1993].

The sol-gel fabrication process allows the fabrication of dense films or ceramics, ceramic fibers, xerogel or aerogel. A solution is prepared from precursors (chemical reagents) and contains colloidal particles. An hydrolysis drives a reaction and allows the formation of a gel, i.e. a 3D solid network containing the solvent molecules in pores. Then, different kinds of heat treatments favor the evacuation of the solvent with a reduction of the volume sample (densification). Bulk materials can be obtained but the sol-gel process is essentially used to get thin films.

After most of the fabrication processes, glasses are usually annealed. The aim of this thermal treatment is to lower the stresses generated. For example, after the quenching of a glass, high temperature gradients induce stresses in the structures. Annealing allows to release these stresses with a slow controlled cooling and increases the sturdiness of the medium. In the case of thin layers deposited by PVD, as for the VIRGO and LIGO mirrors, an annealing step can reduce the absorption properties as well as the thermal noise of the layers [Li et al., 2014].

The definition of non-crystalline solids was presented and the different fabrication processes were quickly overviewed. In the next part, the non-crystalline samples studied in this work and the way they were processed will be described in details.

1.2 Deposition process

The mirrors used in Gravitational Wave detectors are made of a superposition of thin amorphous oxide layers deposited by Ion Beam Sputtering on a fused silica substrate. These layers are composed of non-crystalline silica and titania-doped tantalum oxide. To get a better understanding of the multi-layer properties, a layer by layer analysis was

chosen. Each composition, either silica, tantalum oxide alone or titania-doped tantalum oxide, was deposited individually on different substrates. Then, the annealing is done at $T_a = 500\text{ }^\circ\text{C}$ during 10 hours. The temperature cannot be increased as the amorphous TiO_2 -doped Ta_2O_5 layers crystallize easily, deteriorating the optical properties needed for the mirrors.

To measure the mechanical losses, layers were deposited on a fused silica disk-shaped mechanical resonator (Corning 7980), 3 inches diameter and 1 mm thick. The disks are annealed during 10 hours at $900\text{ }^\circ\text{C}$ before any coating deposition, to relax any residual stress due to the fabrication process. For other characterizations, coatings are deposited on fused silica tablets as shown on figure 1.2, 1 inch in diameter and 6 mm thick. These coatings are polished ($\lambda/10$ flatness, roughness $< 0.5\text{ nm rms}$) to reach as closely as possible the specifications of the substrates used for the gravitational wave detectors mirrors. For silica samples, a 100 nm thick metallic Tantalum layer is deposited prior to the oxide coating on the substrate. As metallic Tantalum has no active Raman vibrational mode, this layer allows the study of the coating only without any post-measurement processing to discriminate the substrate and the coating signals. No metallic Tantalum layers are deposited below the Tantalum pentoxide amorphous layers as annealing induces a reaction between the two layers. Indeed, a difference in their thermal expansion coefficient induces a reaction during annealing and the formation of crystalline Ta_2O_5 .

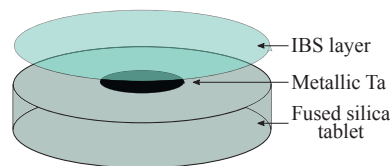


Figure 1.2 – Schematic view of a sample with the IBS-coating on top of a metallic Tantalum layer, both deposited on a fused silica substrate. The metallic Ta layer is deposited only in the case of a silica coating.

The deposited layers are composed of SiO_2 , Ta_2O_5 or TiO_2 -doped Ta_2O_5 . They are between 500 nm and $3\text{ }\mu\text{m}$ thick and are deposited by Ion Beam Sputtering (IBS) at the Laboratoire des Matériaux Avancés (LMA).

A schematic view of an Ion Beam Deposition chamber is represented on figure 1.3. Argon Ions are extracted and accelerated from a plasma by molybdenum grids. The voltage applied on the grids allows to tune the energy of the ions, and the intensity allows a control of the deposition rate. The plume exiting from the ion source strikes a target (SiO_2 , metallic Ta or metallic Ti in our case), where atoms are ejected and deposited onto a substrate. An additional electron flux between the ion source and the targets neutralizes the ion beam to avoid a charge accumulation on the target and in the coating chamber. An oxygen source in the chamber allows stoichiometry to be reached

during the deposition process. Uniformity masks protect certain areas to improve the uniformity on the substrate, while the substrates rotate up to 300 turns/min. A quartz oscillator controls the thickness of the deposited material. The residual pressure in the chamber is 10×10^{-7} mbar before deposition, and 2.4×10^{-4} mbar when Argon (Ar) and oxygen (O_2) gases are fed into the chamber. The temperature of the substrate during the deposition process is approximately 80°C .

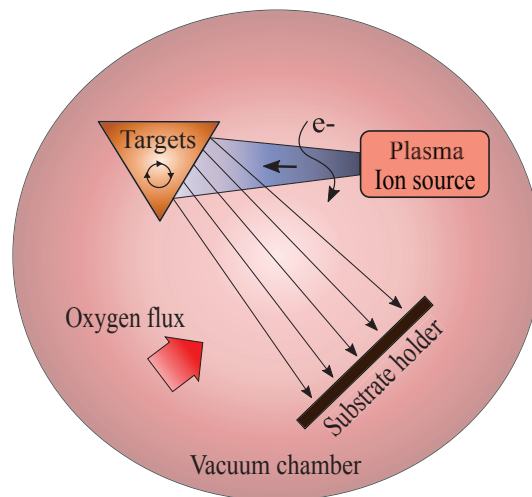


Figure 1.3 – Schematic view of an Ion Beam Sputtering coater.

The LMA possesses two coating chambers : the Grand Coater (GC) with a chamber volume around 10 m^3 , and a Veeco SPECTOR dual-IBS chamber ($V = 0.5\text{ m}^3$) (figure 1.4). Samples studied in this work are all deposited in the Spector except if specified otherwise.



Figure 1.4 – Photos of the two coating chambers at the LMA, the Grand Coater on the left and the Spector on the right [Fresillon, 2016].

1.3 Mechanical losses

1.3.1 Theory

One of the fundamental limitations for a wide number of precision experiments comes from thermal noise in amorphous dielectric materials. This kind of noise is a limit for experiments such as interferometric gravitational wave detectors [Adhikari, 2014], optomechanical resonators [Aspelmeyer et al., 2014], laser frequency standards [Kessler et al., 2012], quantum super computers [Martinis et al., 2005] and atomic clocks [Ludlow et al., 2015].

Thermal energy is distributed over all the degrees of freedom following the equipartition theorem. In a solid, the degrees of freedom correspond to the normal modes of vibration, and so, each of them vibrates with an energy of $k_B T$, k_B being the Boltzmann constant and T the temperature. Although the surface of a solid, like the reflecting one on the test masses of a GW detector, vibrates due to the thermal energy, we cannot talk of thermal noise yet because the spectrum of motion is discrete, i.e. it is limited to the normal mode frequencies. A solid like that is ideal. In a real solid, the elastic moduli fluctuate randomly in space and in time, and this process breaks the displacement correlation between different atoms of the solid. The result is that normal modes no longer exist and the thermal energy is distributed all over the frequencies. In this case, we are in the presence of thermal noise. In a linear system, at the thermal equilibrium, the processes of fluctuations and dissipation of any observable of the system are correlated, as stated by the so called Fluctuation-Dissipation Theorem [Callen and Welton, 1951]. The work of P. R. Saulson gives a useful introduction to the problem of thermal noise in mechanical experiments, and in particular for the GW detectors [Saulson, 1990]. As demonstrated in the work of [Harry et al., 2002], the power spectral density of thermal noise sensed by the laser beam on a free mirror is :

$$S_{xx}(\omega) = \frac{4k_B T}{\omega} \frac{1}{Stiffness} [\varphi_{sub} + D \cdot \varphi_{coat}] \quad (1.1)$$

where the Stiffness is proportional to the substrate Young's modulus and the laser beam diameter, φ is the loss angle of the materials (in our case the substrate and coating materials). D is the so called dilution factor which represents the fraction of strain energy stored in the coating, with respect to the total strain energy of the mirror. D is proportional to the ratio of coating thickness to the laser beam diameter. Far below the first resonance that is around 5 kHz, the Stiffness and the dilution factor are constant on frequency. For a coating stack, we can assume here that the total loss angle is the linear combination of the loss angles of the two used materials where the coefficients are the fractions in thickness. The existence of a boundary effect between layers is still

controversial [Granata et al., 2016]. The loss angle, or more precisely the trigonometric tangent of it, is the ratio between the imaginary and the real parts of the material Young's modulus. It can be demonstrated that in an harmonic oscillation the loss angle is related to the dissipated energy in one cycle, through the following relation :

$$E_{\text{dis}} = 2\pi \cdot E_{\text{max}} \cdot \varphi \quad (1.2)$$

where E_{max} is the maximum elastic energy. Considering that the fused silica substrate has a loss angle of about 10^{-8} [Penn et al., 2006] and the typical coating thickness of $5.9 \mu\text{m}$, the laser beam diameter of about 12 cm and the loss angle of the coating of 2.1×10^{-4} , the coating contribution to the mirror noise (equation 1.1) is about 100 times larger than the substrate one. The thermal noise of coatings is the dominant source of noise in the GW detectors in the frequency band where the detector is most sensitive.

The origin of energy dissipation (and hence of thermal noise) remains unexplained, coming from unknown relaxation mechanisms in the structure. In the amorphous structures, the characteristics of these thermally activated relaxations are fairly well explained by the asymmetric double-well-potential model [Gilroy and Phillips, 1981]. Amorphous materials present a random potential energy landscape. Structural relaxations, causing the dissipation phenomena, correspond to local structural changes between two metastable states separated by a barrier of height V (figure 1.5), with a typical relaxation time τ proportional to $\exp(V/k_B T)$.

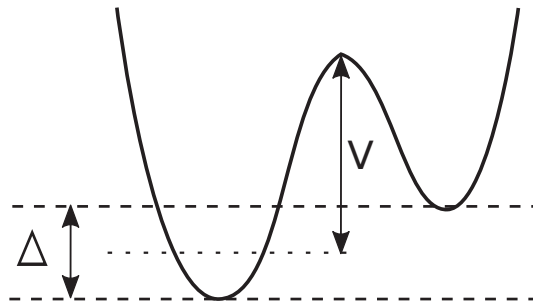


Figure 1.5 – Shape of an asymmetric double well potential. Δ is the Energy difference between the two minima, V the height of the barrier.

Thermal noise originates from unknown relaxation mechanisms in the structure. The main goal of this work is to look for the micro-structural origin of the thermal noise, by studying the structure of the coatings of the test mass mirrors used in the Gravitational Wave Detectors. In order to get an evaluation of the thermal noise level, the mechanical losses of the samples are measured through the method described below.

1.3.2 Mechanical losses measurements

The coatings mechanical losses are measured at the LMA using the resonance method. As stated earlier, to measure the mechanical losses, the coatings are deposited on a silica disk resonator. Part of the setup is shown on figure 1.6. The resonator is suspended from the center using a Gentle Nodal Suspension system (GeNS [Cesarini et al., 2009]). In this method, the disk (1.6-(a)) is supported by a sphere (1.6-(c)) allowing a minimal surface of contact and providing a mechanically stable support. The GeNS system requires no clamping, meaning there are no additional sources of damping, allowing a good reproducibility of the measurements. The resonator is excited at the frequency of its vibrational modes ν_k . To that end, a comb-shape capacitor (1.6-(b)), placed at some distance from the sample avoiding any contact, applies an AC voltage on the substrate (from 0.2 to 3 kVpp [Cadez and Abramovici, 1988]).

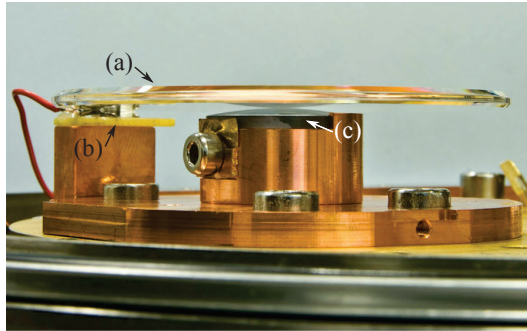


Figure 1.6 – Photo of a Gentle Nodal Suspension system [Granata et al., 2016] with a silica resonator (a) on it. The disk, placed on a spherical surface (c), is excited at the frequency ν_0 with the comb-shaped capacitor (b).

All the vibrational modes k of the resonator are excited one by one. When the excitation is turned off, the resonator is free to ring-down. The amplitude of the vibrations is read through an optical-lever system (more details in [Granata et al., 2016]). The optical signal undergoes then a fast Fourier Transform and is filtered (1Hz band pass centered on ν_0). The exponential fit of the envelope $A(t) = A_0 \exp(-t/\tau_k)$ of the free decay amplitude of the filtered signal is computed, allowing the extraction of the ring-down time τ_k . From the measurement of τ_k for each vibrational mode, the loss angle is calculated :

$$\varphi_k = Q_k^{-1} = (\pi\tau_k\nu_k)^{-1} \quad (1.3)$$

with Q the quality factor and ν_k the resonant frequency of the vibrational mode considered.

The measurements are done in vacuum at $p \leq 10^{-6}$ mbar to avoid any residual gas damping. The modes measured on the disks are typically in the $10^2 - 10^4$ Hz band.

For each sample before and after the deposition of a coating stack, the ring-down time τ_k is measured for several vibrational modes, such that the loss angle φ_k can be averaged to provide the measured losses $\langle\varphi_k\rangle$ with their standard deviation.

The measured mechanical losses are the ones of the entire sample, coating and substrate. To discriminate the losses of the substrate and of the coating, the dilution factor D is needed. This dilution factor can either be computed by the Finite Element Analysis (FEA) numerical method, or measured using the frequency shift of the resonator caused by the deposition of the coating (resonant method) [Li et al., 2014]. In the case of a disk resonator [Granata et al., 2015]:

$$D = 1 - \left(\frac{\nu^u}{\nu^c}\right)^2 \frac{\mu_{\text{sub}}}{\mu_{\text{coat}} + \mu_{\text{sub}}} \quad (1.4)$$

with μ the surface mass densities (kg/m^2) of the substrate (sub) and the coating (coat). ν^u and ν^c are the resonant frequencies of the un-coated and coated resonator.

From the dilution factor, the losses from the coating can be discriminated from the one of the substrate alone [Granata et al., 2015]:

$$\varphi_{\text{res}} = D\varphi_{\text{coat}} + (1 - D)\varphi_{\text{sub}} \quad (1.5)$$

with φ_{res} the total resonator losses.

The resonance method used with the GeNS system allows a characterization of the layers by their mechanical losses, hence thermal noise. To characterize the structure of the samples and look at a possible link with the thermal noise, Infrared, Raman and Brillouin spectroscopies were used.

1.4 Vibrational Spectroscopies

Different spectroscopic techniques were used in this work to analyze the amorphous coatings. Raman and Infrared spectroscopies probe matter at a molecular scale, while Brillouin spectroscopy gives insight on the elastic properties of the material under investigation. The physical principles behind these three types of spectroscopies, and the different spectrometers used for the measurements, will be presented.

1.4.1 Physical principles

Different types of interactions exist between light and matter : absorption, scattering and emission. Light can be represented as photons with an energy $h\nu$ or as an electromagnetic wave with an electric field E :

$$E = E_0 \cos(\omega t - kx) \quad (1.6)$$

where E_0 is the amplitude of the electric field, ω the angular frequency ($\omega = 2\pi\nu$ with ν the frequency), k the wave-vector ($k = 2\pi/\lambda$ with λ the wavelength). Matter can be described in quantum mechanics as a set of discrete energy levels coming from different contributions (electronic, vibrational and rotational). Then for any light and matter interaction to happen, the energy of the incident (or emitted) light must match one of the energy level difference of the considered matter:

$$h\nu = \Delta E \quad (1.7)$$

with ΔE corresponding to the energy difference between two levels of energy.

Absorption The absorption of a photon happens when the incident light energy corresponds to the difference of two distinct energy levels of the molecules, which excites the molecule encountered (equation 1.7). The transmitted light presents then a lower intensity than the incident light at this specific wavelength. Infrared (IR) spectroscopy is based on this process.

Emission The emission of a photon happens when a molecule in a higher energy state converts to a lower one, like fluorescence or luminescence.

Scattering Scattering corresponds to a change in direction when the light interacts with a material. In scattering processes, when a molecule is excited by a light wave, it can re-emit a photon of the same energy, i.e. same wavelength, corresponding to elastic scattering (such as Rayleigh scattering). The incident photon can also exchange

energy with the medium in the case of inelastic scattering (such as Raman and Brillouin scattering). The incident and emitted photons will therefore have different wavelengths.

To respect the energy conservation law, in the case of an exchange of energy, the excess (or lack) of energy is transferred towards (from) the molecule with the emission (annihilation) of a phonon. A phonon is a quasi-particle which can be associated with an elementary vibrational quantum of energy.

As sketched on figure 1.7, Stokes scattering corresponds to the case where a phonon is emitted, and the scattered photon is therefore less energetic. On the contrary, when the scattered photon is more energetic, the process is called Anti-Stokes scattering and a phonon is annihilated.

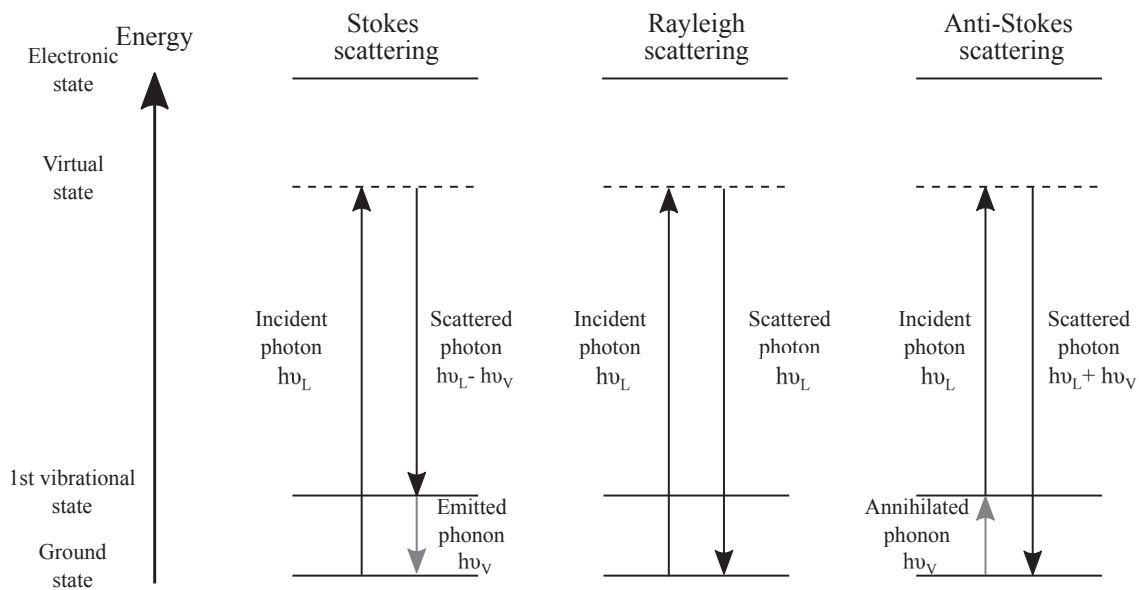


Figure 1.7 – Schematic view of the energy levels involved in the inelastic scattering (Stokes and Anti Stokes) and the elastic scattering (Rayleigh).

These processes can be described through quantum mechanics. During scattering, the energy $\hbar\omega$ and the wave-vector \mathbf{k} are preserved. For an incident photon of wave-vector k_0 and angular frequency ω_0 (figure 1.8) interacting with a material, leading to a scattered photon (\mathbf{k}, ω) and to the creation - plus sign - (or annihilation - minus sign) of a phonon (\mathbf{q}, Ω), we can write :

$$\omega_0 = \omega \pm \Omega \quad (1.8)$$

$$\mathbf{k}_0 = \mathbf{k} \pm \mathbf{q} \quad (1.9)$$

If we focus on the Stokes effect (plus sign) to ease the reading, the transferred wave-vector q can be expressed as :

$$q^2 = k_0^2 + k^2 - 2k_0k \cos(\theta) \quad (1.10)$$

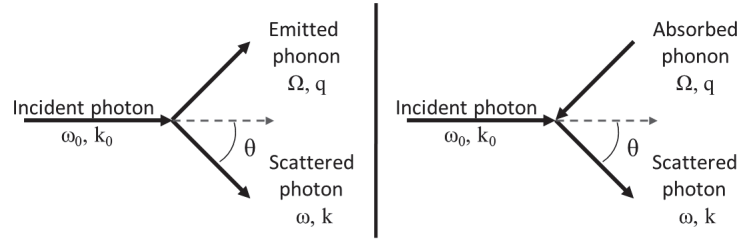


Figure 1.8 – Schematic view of the Stokes (left) with the creation of a phonon, and Anti-Stokes (right) with the annihilation of a phonon, inelastic scattering processes.

With θ the angle between the incident photon and the emitted one. Considering the case where the wave-number dependency on the refractive index corresponds to $k_0 = n\omega_0/c$ and $k = n\omega/c$, we get :

$$q^2 c^2 = n^2 \omega_0^2 + n^2 (\omega_0 - \Omega)^2 - 2n^2 \omega_0 (\omega_0 - \Omega) \cos \theta \quad (1.11)$$

Equivalent to :

$$\frac{q^2 c^2}{n^2 \omega_0^2} = \frac{\Omega^2}{\omega_0^2} + 4 \left(1 - \frac{\Omega}{\omega_0}\right) \sin^2 \left(\frac{\theta}{2}\right) \quad (1.12)$$

In the case of inelastic scattering, the energy exchange is very small compared to the incident energy, leading to $\Omega \ll \omega_0$ ((GHz - THz) $\ll 10^{15}$ Hz). In this case, the equation 1.12 can be simplified in :

$$\frac{qc}{n\omega_0} = 2 \sin \left(\frac{\theta}{2}\right) \quad (1.13)$$

Which, by introducing the incident wavelength λ_0 , leads to :

$$q = 2k_0 \sin \frac{\theta}{2} = \frac{4\pi n}{\lambda_0} \sin \frac{\theta}{2} \quad (1.14)$$

The equation 1.14 links the wavenumber q of the phonon, to the incident wavelength λ_0 and scattering angle θ .

A simplified dispersion curve for a crystal of cell parameter a is represented on figure 1.9, allowing a general view of the two kinds of scattering used in this work. Raman and Brillouin scattering both result from the scattering of phonons, with small wavenumber q , compared to the limit of the Brillouin zone at π/a (a the cell parameter). The frequency related to Raman scattering corresponds to optical phonons. The slope of the dispersion curve of the optical phonons in the Raman frequency area is close to zero, leading to a trivial dependency on θ , i.e. non-dispersive phonons in the area of interest for Raman scattering. In the case of Brillouin scattering, the frequencies of the considered phonons correspond to acoustic phonons. The linear dependency of the

wavenumber with the frequency has a non-zero slope, which implies dispersive acoustic phonons. Hence, the frequency of the Brillouin scattering will depend on the scattering geometry (i.e. on the angle θ).

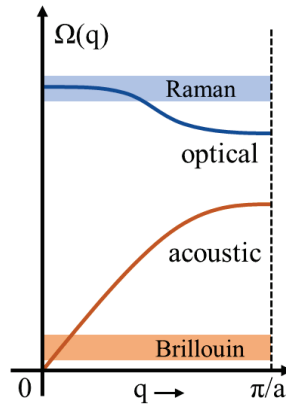


Figure 1.9 – Schematic dispersion curves in a crystal with cell parameter a . Raman (blue zone) and Brillouin (orange zone) result from the scattering of the phonons of zone center, with the Raman scattering corresponding to optical phonons and the Brillouin scattering to acoustic phonons.

The equations driving Raman scattering will be presented along the setup used for the measurement, then Brillouin scattering will be also developed.

1.4.2 Raman spectroscopy

Raman spectroscopy is a non-destructive method which probes the structure at short and medium range order [Coussa-Simon, 2008, Deschamps, 2009, Mermet, 1996, Ferraro, 2003, Schrader, 1995]. It is based on the inelastic scattering of an incident monochromatic wave which can probe the vibrational energy levels of the sample, by annihilation or creation of an optical phonon. Raman scattering was predicted in 1923 by A. Smekal and was first observed by Indian physicists [Raman and Krishnan, 1928], in parallel to G. Landsberg and L. Mandelstam. Raman spectroscopy considerably developed with the apparition of lasers, introducing more powerful light sources, thus generating a more intense Raman signal. As it probes the vibrations of the structure, this type of spectroscopy is particularly well-suited to study glass structures compared to X-ray diffraction which needs a periodic network. Raman spectroscopy also proved to be a useful tool to follow in situ evolution of glasses under thermodynamic changes (Pressure, Temperature).

In Raman spectroscopy the sample is illuminated by a monochromatic laser light (usually in the visible range). Using a classical approach, Raman scattering originates in

the fluctuation of the polarizability of the material, due to the interaction with the electric field of the incident light. When light and matter interact, we can consider that only the electrons in the material oscillate with the frequency ν_0 of the incident electromagnetic wave, inducing fluctuations of the polarizability at every point \mathbf{r} of the material. In a medium, the polarizability by a volume unit $\mathbf{P}(\mathbf{r},t)$ is defined as :

$$\mathbf{P}(\mathbf{r},t) = \chi(\mathbf{r},t)\mathbf{E}(\mathbf{r},t) \quad (1.15)$$

with $\chi(\mathbf{r},t)$ the dielectric susceptibility tensor and $\mathbf{E}(\mathbf{r},t)$ the electric field.

The polarizability oscillations produce, in turn, a new electric field. From the Maxwell equations and in a volume $d^3\mathbf{r}$ around \mathbf{r} , this scattered electric field at a point \mathbf{R} can be expressed as :

$$d\mathbf{E}(\mathbf{R},t) = \frac{1}{4\epsilon_0 c^2 \pi \|\mathbf{R} - \mathbf{r}\|} \left(\frac{\delta^2 \mathbf{P}(\mathbf{r},t')}{\delta t'^2} \wedge \mathbf{u} \right) \wedge \mathbf{u} \, d^3\mathbf{r} \quad (1.16)$$

with $t' = t - \|\mathbf{R} - \mathbf{r}\|/c_n$ corresponding to the retarded time (where c_n is the light speed in the material) and \mathbf{u} is the unit vector colinear to $(\mathbf{R} - \mathbf{r})$. This equation 1.16 indicates that the intensity of the scattered wave comes from the time dependence of the polarizability. From equation 1.15, two origins can explain this time dependency : the oscillations of the incident electric field $\mathbf{E}(\mathbf{r},t)$ or the oscillations of $\chi(\mathbf{r},t)$.

As the dielectric susceptibility can be decomposed as a constant value χ_0 and a fluctuating one $\delta\chi(\mathbf{r},t)$:

$$\chi(\mathbf{r},t) = \chi_0 + \delta\chi(\mathbf{r},t) \quad (1.17)$$

the polarizability can be expressed as :

$$\mathbf{P}(\mathbf{r},t) = [\chi_0 + \delta\chi(\mathbf{r},t')]\mathbf{E}_0 \exp i(\mathbf{k}_0 \cdot \mathbf{r} - \omega_0 t') \quad (1.18)$$

In our case, the frequency of the incident electromagnetic wave is much larger than the characteristic frequency variation of the dielectric susceptibility, $\omega \ll \omega_0$, such that we can write :

$$\frac{\delta^2 \mathbf{P}(\mathbf{r},t)}{\delta^2 t^2} \approx -\omega_0^2 \quad (1.19)$$

The scattered electric field can then be written as:

$$\mathbf{E}(\mathbf{R},t) \propto \omega_0 \int [\chi_0 + \delta\chi(\mathbf{r},t')] \exp i((\mathbf{k}_0 \cdot \mathbf{R} - \omega_0 t) \cdot \mathbf{r}) \exp i((\mathbf{k}_0 - \mathbf{k}) \cdot \mathbf{r}) d^3\mathbf{r} \quad (1.20)$$

In the case where there is no susceptibility fluctuations, the scattered field is null except when $\mathbf{k}=\mathbf{k}_0$. The χ_0 term indicates that the incident light wave propagates through the medium with a frequency $\omega = \omega_0$ in the incident direction $\mathbf{k}=\mathbf{k}_0$. When there is no susceptibility fluctuations ($\delta\chi_j(\mathbf{r},t') = \delta\chi(\mathbf{r})$), only elastic scattering occurs (Rayleigh scattering), and no new frequencies are generated. The inelastic scattering originates

from the spatiotemporal fluctuations of the dielectric susceptibility, induced by the vibrational waves.

In this case, the dielectric susceptibility fluctuation for a vibration mode j is written as:

$$\delta\chi_j(\mathbf{r}, t') = \delta\chi_j(\mathbf{q}) \exp i(\mathbf{q} \cdot \mathbf{r} \pm \omega_j(\mathbf{q})t') \quad (1.21)$$

The corresponding electric field induced by these fluctuations is therefore :

$$\mathbf{E}_j(\mathbf{R}, t) \propto \exp i(\mathbf{k} \cdot \mathbf{R} - (\omega_0 \pm \omega_j(\mathbf{q}))t) \int \delta\chi_j(\mathbf{q}) \mathbf{E}_0 \exp i[(\mathbf{k}_0 - \mathbf{k} + \mathbf{q}) \cdot \mathbf{r}] d^3\mathbf{r} \quad (1.22)$$

The scattering is non-zero only for $\mathbf{q} = \mathbf{k} - \mathbf{k}_0 \neq 0$, giving a scattered wave frequency $\omega = \omega_0 \pm \omega_j(\mathbf{q})$. In the case of Raman spectroscopy, the incident wavelength is usually between 400 nm and 800 nm. For the highest q possible, i.e. taking the two limit values for k and k_0 , the phonon wavenumber is around $q = 8 \times 10^{-3} \text{ nm}^{-1}$. Compared to the typical Brillouin zone in crystals ($\approx \pi/a$ with a the crystallographic cell size), this wavenumber is very small. The only phonons detected by inelastic light scattering are then those with a wavenumber \mathbf{q} close to zero (or equal to zero for $\theta = 0$).

Considering Raman scattering, the phonons with a wavenumber close to zero are optical phonons ($\omega > 1 \text{ cm}^{-1}$), corresponding to non propagative vibrational modes. On the other hand, acoustic phonons near the Brillouin zone center ($\omega < 1 \text{ cm}^{-1}$) correspond to propagative modes. Hence, the typical frequencies corresponding to Raman scattering cover the range from a few cm^{-1} to 4000 cm^{-1} .

The optical phonon distribution at thermal equilibrium obeys the Bose-Einstein statistic. As the ground state is the most populated state and the Stokes/Anti-Stokes intensity ratio depends on the thermal population factor, the Stokes Raman scattering is the most intense. The Stokes scattering intensity can be expressed as :

$$I(\omega) \propto (n(\omega) + 1) \frac{g(\omega)C(\omega)}{\omega} \quad (1.23)$$

with C a coupling coefficient, $g(\omega)$ the vibrational density of states, and $n(\omega)$ the Bose-Einstein factor :

$$n(\omega) = \frac{1}{\exp(\hbar\omega/kT) - 1} \quad (1.24)$$

Raman experimental setup

Raman spectra were recorded with a micro-Raman spectrometer LabRAM HR Evolution (figure 1.10), with an excitation wavelength at 532 nm emitted by a YAG:Nd³⁺ laser.

From figure 1.10, the monochromatic light emitted by the laser goes through a polarizer (P1), a filter (F) and different lenses (L1 and L2) focusing the beam with a confocal hole (H1). The first super-notch filter (SNF) totally reflects the incident light towards a

confocal microscope. The light diffused by the sample then goes through the SNF and towards the spectrograph. The LabRAM spectrometer presents three super-notch filters (Volume Holographic Bragg Grating VHBG - Optigrade) allowing to measure low frequencies down to only $5\text{-}10\text{ cm}^{-1}$ around the Rayleigh line. A polarizer (P2) allows to analyze the scattered signal. At this point, in the spectrograph, a grating (G) disperses the signal onto a Peltier cooled charge-coupled system (CCD).

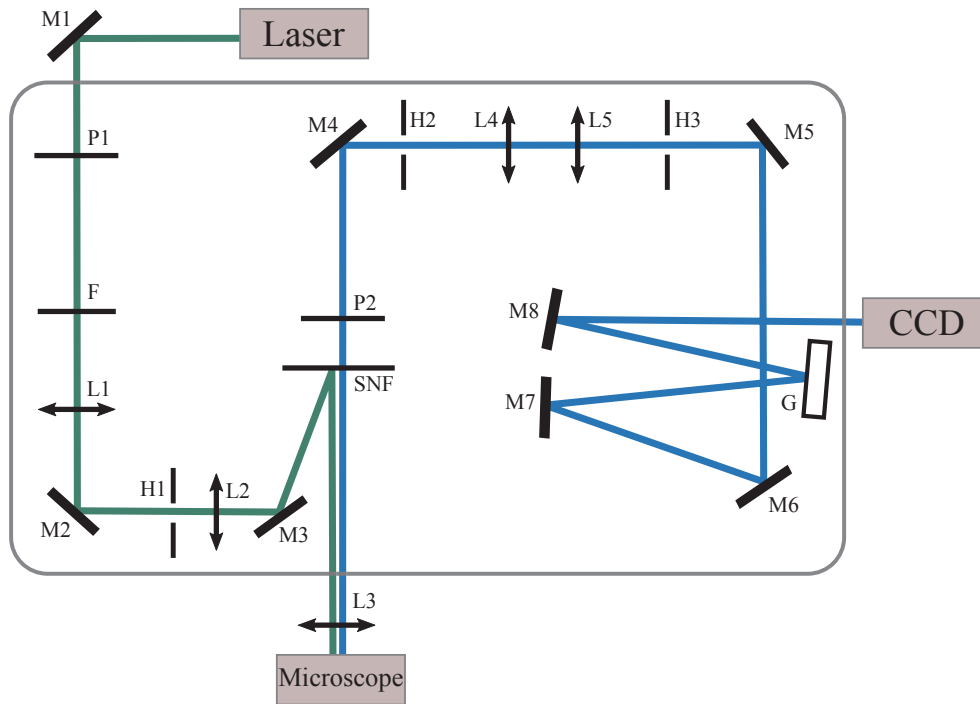


Figure 1.10 – Schematic view of the LabRAM spectrometer. M correspond to Mirrors, F to filters, L to Lenses, H to holes, P to Polarizers, G to the grating and SNF to the super-notch filter.

In the case of thin layers, the depth of field is an important parameter to be sure we are probing only the material of interest and not its substrate. The depth of field depends on the incident laser wavelength λ , on the refractive index of the medium where the light travels ($n = 1$) and on the numerical aperture ($NA = n \sin \alpha$ with α the maximal half-angle of the cone of light that can enter or exit the lens) :

$$\Delta z = n \frac{4\lambda}{NA^2} \quad (1.25)$$

The objectives used in this work were OLYMPUS x100, one MPlanN with $NA = 0.90$ and the other SLMPlan ($NA=0.60$) corresponding to $\Delta z_{MPlan} = 2.6\ \mu\text{m}$ and $\Delta z_{SLMPlan} = 5.9\ \mu\text{m}$ respectively.

1.4.3 Brillouin spectroscopy

Brillouin scattering was predicted in 1922 by Léon Brillouin [Brillouin, 1922], and was experimentally observed in 1930 [Gross, 1930]. Brillouin spectroscopy probes the acoustic vibration modes in matter and can give access to its macroscopic properties: elastic constants, Young modulus, Bulk modulus... [Sonneville et al., 2012, Girard, 2016]

For $\Omega \ll \omega_0$ (figure 1.8), phonons are close to the center of the Brillouin zone (linear q dependency in first approximation). The dispersion relation can be written as $\Omega = V_{L/T}q$ where $V_{L/T}$ are the longitudinal and transverse speeds of sound, respectively. Transverse phonons are polarized perpendicularly to their propagation direction while longitudinal phonons are polarized alongside their propagation direction.

The Brillouin frequency, corresponding to the phonon frequency, can be expressed from 1.14 :

$$v_B = \frac{\Omega}{2\pi} = \frac{2nV_{L/T}}{\lambda_0} \sin\left(\frac{\theta}{2}\right) \quad (1.26)$$

As Brillouin measurements are often done in the back-scattering disposition ($\theta = 180^\circ$), the Brillouin frequency can then be simplified as :

$$v_B = \frac{2nV_{L/T}}{\lambda_0} \quad (1.27)$$

For an isotropic medium, the Brillouin frequency allows to compute the longitudinal and transverse acoustic speed :

$$V_L = \sqrt{\frac{C_{11}}{\rho}} \quad (1.28)$$

$$V_T = \sqrt{\frac{C_{44}}{\rho}} \quad (1.29)$$

C_{11} and C_{44} correspond to the elastic coefficients representing the deformation across the applied stress. From the two elastic coefficients C_{11} and C_{44} , the Young modulus Y can be deduced :

$$Y = \frac{C_{44}(3C_{11} - 4C_{44})}{C_{11} - C_{44}} \quad (1.30)$$

The Brillouin spectrum of a material presents a peak with a certain Full Width at Half Maximum (FWHM), usually larger than the apparatus resolution. In general, for bulk homogeneous materials, the broadening of the Brillouin band comes from sound attenuation. However for smaller volumes, like thin films, an additional component due to sample thickness produces a larger broadening effect [Vacher et al., 2006]. For example, for silica glass, the additional broadening of the signal in the case of a 100 μm thick layer is around 50 MHz while the same effect is approximately 500 MHz for a 10 μm thick layer [Vacher et al., 2006]. This effect prevents any analysis of the broadening of

the Brillouin line in the case of thinner films, the induced broadening being of the order of 2 GHz for 3 μm thick samples as the one we studied.

Brillouin experimental setup

Brillouin spectroscopy probes much lower frequencies than Raman spectroscopy, typically around $1 \text{ cm}^{-1} \approx 30 \text{ GHz}$. The intensity of the Brillouin signal is also much lower, around 10^{-10} to 10^{-12} of the Rayleigh line intensity. A usual Raman spectrometer cannot reach these frequencies, as they are too close to the Rayleigh line for a super Notch filter to be spectrally resolved enough. Hence, another setup is needed to approach these frequencies. J.R. Sandercock developed a tandem Fabry-Pérot interferometer, allowing the measurement of frequency shifts between 3 GHz and $\sim 500 \text{ GHz}$ (equivalent to 0.1 cm^{-1} to $\sim 15 \text{ cm}^{-1}$). The spectrometer is based on the association of two Fabry-Pérot interferometers filtering the elastic scattering, coupled with a microscope to study microscopic samples in the backscattering geometry.

Fabry-Pérot interferometer A Fabry-Perot interferometer consists of two plane mirrors mounted in parallel one to the other, with a distance L_1 between them [Sandercock., 1999]. This optical spacing determines the only possible transmitted wavelengths λ , as expressed by :

$$T = \frac{\tau_0}{1 + (4F^2/\pi^2) \sin^2(2\pi L_1/\lambda)} \quad (1.31)$$

with T the transmission function of the interferometer, $0 < \tau_0 < 1$ the maximum possible transmission determined by losses in the system, and F the finesse. The finesse F characterizes the energy losses of the cavity and depends on the mirror reflectivity and flatness. This characteristic of the Fabry-Perot interferometer can be expressed as :

$$F = \frac{\Delta\nu}{\delta\nu} = \frac{\pi\sqrt{R}}{1-R} \quad (1.32)$$

with $\Delta\nu$ the free spectral range (spacing between two consecutive transmitted wavelengths), $\delta\nu$ the width of a peak, and R the reflectivity. When the finesse is high enough, the cavity only transmits wavelengths λ that verify the following relation :

$$L_1 = p\lambda/2 \quad (1.33)$$

where p is an integer, which can also be expressed as :

$$\nu = \frac{pc}{2L_1} \quad (1.34)$$

On figure 1.11.B, an example of two Fabry-Pérot cavities and three orders passing through the cavities are presented.

The contrast of the cavity, corresponding to the ratio between the intensity of one transmission peak to the minimum intensity can be expressed for n round trips in the cavity as :

$$C = \left[\frac{1 + R}{1 - R} \right]^{2n} \quad (1.35)$$

One limitation of using a single Fabry-Pérot cavity is the mixing of higher orders. To avoid this mixing of p and $(p + 1)$ orders, J.R. Sandercock developed a setup using two Fabry-Pérot cavities.

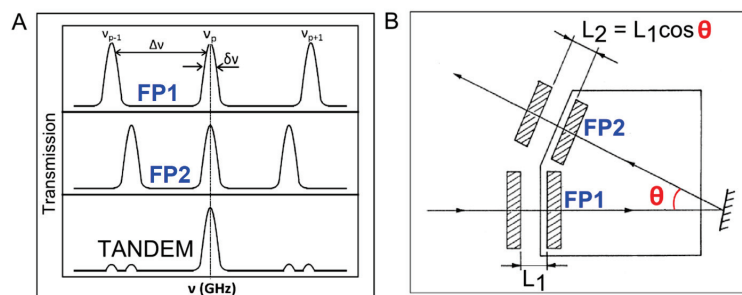


Figure 1.11 – Transmitted intensity by both cavities FP1 and FP2 and by the tandem (A). Schematic view of a Fabry-Pérot tandem with the two cavities (B) [Girard, 2016].

Tandem Fabry-Pérot A Brillouin spectrometer consists of two coupled Fabry-Pérot cavities where the second is spaced with a slightly different direction from the first one. Different optical paths are obtained with the geometry presented on figure 1.11.B, with $L_2 = L_1 \cos \theta$. With these two different lengths, the transmitted light is reduced to the coinciding signals as shown on 1.11.A. The remaining intensity of superior orders can, under certain circumstances, generate a peak with a really low intensity on the Brillouin spectra called "ghost".

Figure 1.12 presents the light path in a Brillouin spectrometer such as the one used in this work. Part of the beam is removed as a reference signal. The laser beam is going through the microscope holding the sample, and the backscattered light is focused by two lenses via a beam splitter in the spectrometer itself. The mirrors M1 and M2 send the light through the first Fabry-Pérot (FP1) cavity, another mirror M3 deflects it through the second cavity (FP2). A 90° prism sends the light back on the same path, and the mirror M4 allows a third crossing of the FP1 and FP2. Then, a mirror M5 sends the light on a 60° prism, a last reflection happens on M6 and the light travels towards the photomultiplier after a hole and focusing lens. The spectrometer used in this work has an incident light at $\lambda = 532$ nm.

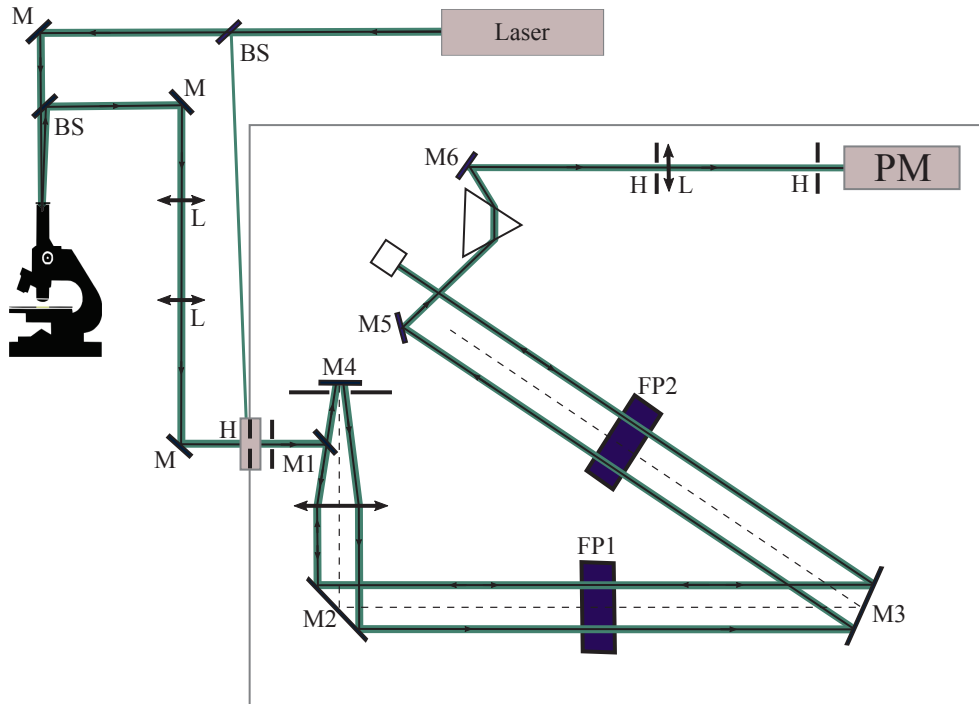


Figure 1.12 – Schematic view of the Brillouin spectrometer. M corresponds to Mirrors, BS to Beam-Splitters, L to Lenses, H to holes and FP1 and 2 to the two Fabry-Pérot cavities.

1.4.4 Infrared spectroscopy

Infrared spectroscopy is based on the absorption of some wavelengths of the incident light by matter, in the 700 nm and 1000 nm range. This spectroscopic technique is mainly used to characterize chemical components. One way to describe the process is to use classical mechanics with the model of a harmonic oscillator.

Model of a harmonic oscillator

A simple way of describing a vibrating molecule is to consider two masses m_A and m_B at a distance r from each other, connected by a spring of force constant k (figure 1.13), and vibrating at a given frequency ν . The distance between the two atoms at equilibrium is r_{eq} .

Applying Newton's law while considering the center of mass of the two atoms, we can write :

$$\mu \frac{d^2(r - r_{eq})}{dt^2} = -k(r - r_{eq}) \quad (1.36)$$

with $\mu = m_A m_B / (m_A + m_B)$, the reduced mass.

The solution of the second order differential equation is $r(t) = r_0 \cdot \cos(\omega t + \phi)$ with ϕ

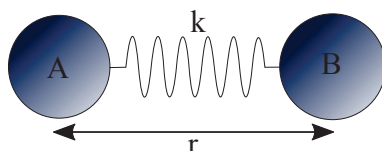


Figure 1.13 – Model of a harmonic oscillator with two atoms A and B of masses m_A and m_B respectively, connected by a spring of constant k and at a distance r from each other.

the phase, r_0 the amplitude (both determined by the initial conditions) and ω :

$$\omega = \sqrt{\frac{k}{\mu}} = 2\pi\nu \quad (1.37)$$

Consequently, we get :

$$\nu = \frac{1}{2\pi} \sqrt{\frac{k}{\mu}} \quad (1.38)$$

The equation describes the frequency of the vibration of a diatomic molecule, depending on μ and on k the force constant of the spring which characterizes the bond between the two atoms.

Hence, if an incident electromagnetic wave encounters the spring with a frequency ν , the bond vibrates.

Active vibrations

These phenomena can also be described by Quantum mechanics. The absorption of a photon corresponds to a change of the energy levels of a molecule, implying selection rules. These selection rules determine if an incident photon will be absorbed or not by a sample, allowing -or not- a transition between different vibrational states. With Infrared techniques, a vibration can be detected if it induces a variation of the molecule dipole moment.

When a molecule vibrates, the dipole moment can oscillate. According to classical theory of the electromagnetic radiation, for a given frequency of oscillation, a dipole can emit or absorb an electromagnetic wave having the same frequency. It is then needed that a vibration drives a dipole moment oscillation at a frequency ν_0 to get light absorption at the same frequency ν_0 . When the incident light encounters the molecules, the electric field pulls away the centers of mass of the positive and negative charges inducing an oscillation of the dipole moment at the same frequency ν_0 .

For illustration purposes, we will focus on the CO_2 molecule, which presents a planar and linear geometry, and has three vibrational modes (as shown on figure 1.14). The carbon atoms electronegativity is lower than the one of the oxygen atoms, but due to the

molecule geometry, the dipole moment at equilibrium is non-existent. For symmetric stretching, the center of mass does not evolve with the vibrations such that the dipole moment of the molecule remains non-existent. However, for asymmetric stretching and bending, the center of mass evolves with the vibrations inducing dipole moment variations. Hence, these two vibrations modes can be analyzed with Infrared spectroscopy, in contrast with the symmetric stretching case.

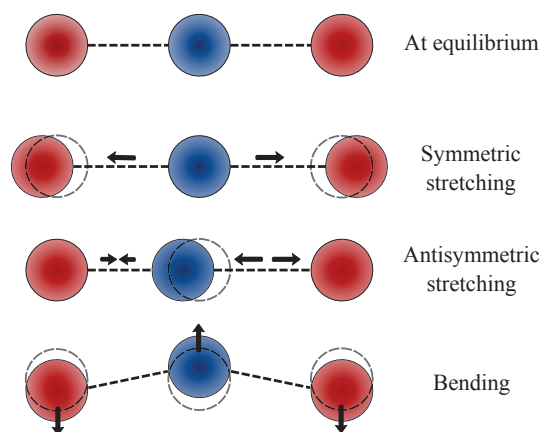


Figure 1.14 – Vibration modes of a CO₂ molecule.

Attenuated Total Reflection Fourier Transform Infrared (ATR-FTIR) Techniques

As seen previously in section 1.2, samples studied in this work are thin layers deposited on a thick fused silica substrate. The geometry of our samples prevents an analysis via transmission Infrared spectroscopy, which measures directly the absorption through the sample. Hence, spectra in this work were all acquired by Attenuated Total Reflection Fourier Transform Infrared spectroscopy (ATR-FTIR).

ATR-FTIR spectroscopy allows the characterization of solids or liquids with no preparation beforehand, and can easily be used when only the surface of a sample needs to be analyzed, as it probes only a few microns depth. This is therefore a perfect technique for opaque samples, thin films or samples too thick to be transparent enough with transmission.

By illuminating with a given angle a crystal with high refractive index, the incident infrared light can be coupled inside this crystal, thus generating an evanescent wave at the surface of the crystal (figure 1.15). In our case, the crystal is a Germanium crystal with a refractive index $n = 4$ at the considered wavelengths. The angle of incidence on the sample is defined by the geometry of the setup (45° in our case), and spectra are really close to these acquired by transmission. If the sample is placed along the surface, the electric field of the evanescent wave can interact with the vibrational modes, and be

absorbed by the sample. The reflectance R (percentage of reflected light) is given by :

$$R = \frac{I_R}{I_0} \quad (1.39)$$

with I_R the reflected light by the sample and I_0 the reflected light by a non-absorbent medium taken as reference. For each acquisition, the spectrum of the crystal alone is subtracted to the signal of the sample.

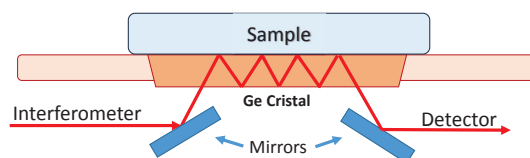


Figure 1.15 – Diagram of the ATR sample holder. The light coming from the interferometer is reflected towards the Germanium crystal, with a 45° angle. The light is coupled inside the crystal which is in contact with the sample. Then, after emerging from the crystal, the light carries out the information towards the detector via a last mirror.

The depth of penetration into the sample corresponds to the distance at which the electric field decays to e^{-1} of its initial value and usually corresponds to 1/5 to 1/20 of the incident wavelength λ . The depth of penetration also depends on the incidence angle φ , the refractive index of the crystal n_1 and of the sample n_2 [Schrader, 1995]

$$d_p = \frac{\lambda_1}{[2\pi(\sin^2\varphi - n_2^2/n_1^2)^{1/2}]} \quad (1.40)$$

with $\lambda_1 = \lambda/n_1$ the effective wavelength in the crystal.

IR spectrometer

The ATR-FTIR setup used in this work is an Infrared Perkin-Elmer Fourier Transform GXFT-IR, whose schematic description is given on figure 1.16. The light source of the IR-spectrometer is a Tungsten filament with a quartz cover. First, the incident light beam goes through two apertures : the field stop is a beam spreading aperture which fixes the size of the beam going through the spectrometer. The second is an aperture stop, a Jacquinot aperture, limiting the divergence and controlling the resolution of the spectrometer. The light is reflected into a Michelson interferometer (Dynascan interferometer) with a KBr beam splitter allowing to scan the entire spectrum in a very short time. Another mirror sends the beam through the sample, or the ATR-FTIR setup in our case, and the signal is then detected by a Media Infrared Triglycine Sulfate (MIRDTGS) detector.

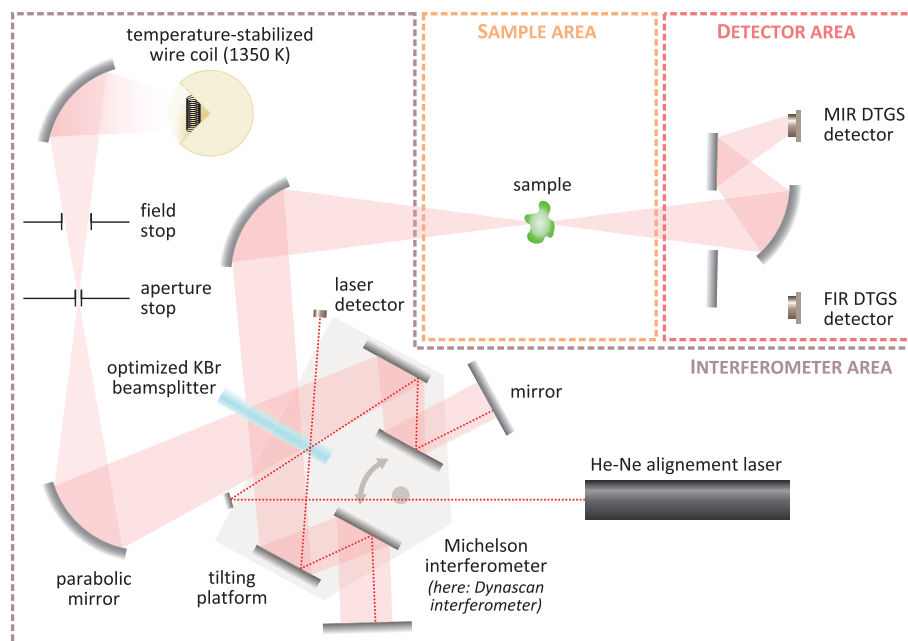


Figure 1.16 – Diagram of the FTIR spectrometer (E. Guillaud, ILM). The ATR-FTIR setup is placed in the sample area during acquisitions.

1.4.5 Conclusion

The three vibrational spectroscopies used in this work to characterize the non-crystalline layers were presented and are based on absorption and scattering phenomena. Infrared and Raman spectroscopies probe the vibrations at a molecular scale with different selection rules while Brillouin spectroscopy probes the elastic properties of the materials, at a macroscopic level.

Infrared spectroscopy originates from changes in the dipole moments, Raman scattering is sensitive to polarizability fluctuations while Brillouin scattering derives from the dielectric susceptibility of the material.

All of these techniques are non destructive and allow the characterization of small samples ($\approx \mu\text{m}^2$). In situ characterizations following the structural evolution with pressure or temperature of the vibrational spectra of the samples are also possible.

1.5 High pressure measurements

The diamond anvil cell (DAC) allows to study microscopic samples subjected to pressures up to a few tens of GPa. The advantage of this device comes from its size allowing in situ spectroscopic measurements as the diamonds are transparent on a large spectral band from Infrared to gamma rays. This device is essential in the fundamental physics and chemistry of condensed matter. Indeed, inducing changes due to pressure in the molecular structure and elastic properties enables a better understanding of the system. Moreover, high pressure measurements are also used in geology to reproduce the extreme conditions found in the Earth mantle.

The cell used in this work is composed of two identical cut diamonds (type IA, 4 mm, 0.4 mm, 1.8 mm) whose two cylindrical planes are facing each other (figure 1.17). A metallic seal (stainless steel) is caught in vice by the two diamonds, the hole drilled in the seal by electrical discharge machining is defining the experimental volume. High pressure can be reached thanks to the conical cut of the diamonds, insuring an important ratio between the surfaces of the two parallel sides of the diamonds.

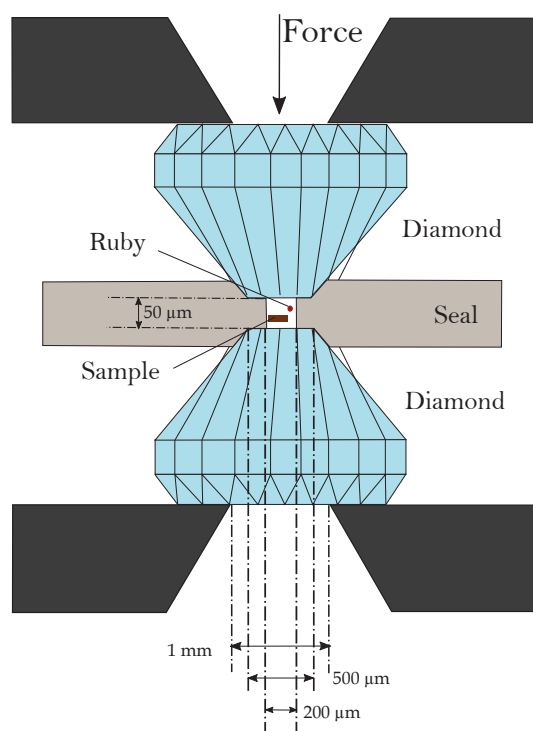


Figure 1.17 – Schematic view of a Diamond Anvil Cell. The sample and a ruby chip are placed inside a drilled seal with a transmitting medium. The pressure is applied via an annular membrane allowing an isotropic distribution of the force on the diamonds.

The lower diamond is set in a cylinder in which a piston is sliding, with the upper

diamond set in it. The cell used for the experiments presented in this thesis, is the one developed by [Chervin et al., 1995]. The pressure is applied via an annular metallic membrane, allowing an isotropic distribution of the force on the piston, which is deformed by the insertion of an inert gas. By this way, the pressure can be checked at any time without moving the cell (opposed to the screwed cells). In our setup, pressure up to 30-50 GPa can be reached, the final pressure depending on the size of the hole in the seal and the size of the culets. The typical size of the hole in the seal for our experiments was between 100 μm and 200 μm , with a thickness of the metallic tablet between the diamonds close to 50 μm .

A transmitting media is then added to transform the uni-axial constraint from the diamonds into an hydrostatic or quasi-hydrostatic constraint. The transmitting media used in our experiments are either a methanol/ethanol/water (16/3/1) mix or argon. Argon is quasi-hydrostatic for pressures up to 19 GPa, while the methanol/ethanol/water mix is hydrostatic only up to 10.5 GPa [Klotz et al., 2009].

The ruby chip ($\text{Al}_2\text{O}_3:\text{Cr}^{3+}$) deposited in the experimental volume allows to measure the pressure inside the cell via its luminescence spectrum. Indeed, Cr^{3+} luminescence spectrum presents two intense bands R1 and R2 (${}^2\text{E} \rightarrow {}^4\text{A}_2$) with an emitting wavelength depending on the pressure. The empirical relationship between the wavelength λ (nm) and the pressure p (GPa) in our setup is the following [Mao et al., 1978]:

$$p = 380.8 * \left(\left(\frac{\lambda}{\lambda_0} \right)^5 - 1 \right) \quad (1.41)$$

with λ_0 the emitting wavelength of R1 at ambient pressure and λ its emitting wavelength at the pressure p . The equation 1.41 allows to precisely determine the pressure inside the experimental volume by following the R1 luminescence band for a ruby excited by a laser of smaller wavelength (532 nm in our case).

1.6 Rutherford Backscattering Spectroscopy

As previously explained, the gravitational wave detectors mirrors are composed of SiO_2 and TiO_2 -doped Ta_2O_5 layers. To analyze the latter, we need to know the concentrations of TiO_2 and Ta_2O_5 in the thin films. For this purpose, Rutherford Backscattering Spectrometric (RBS) measurements were conducted. The RBS technique allows a quantitative analysis of the concentrations of different elements in a structure. This elastic scattering of particles (usually high energy ions) by the nucleus of the target atoms was first observed and explained by [Rutherford, 1911, Geiger and Marsden, 1909]. Later on, the RBS was described as a method for material analysis by Rubin et al., 1957.

RBS is based on the detection of the energy of scattered particles by a target. As schematized on figure 1.18, an incident particle of mass m_1 and velocity \mathbf{V}_1 hits a target, i.e. the nucleus of an atom of mass M_2 . After the impact, the incident particle is scattered with an angle θ and presents a new velocity \mathbf{V}'_1 . The nucleus, initially motionless ($\mathbf{V}_2 = 0$), is moving at \mathbf{V}'_2 after the collision.

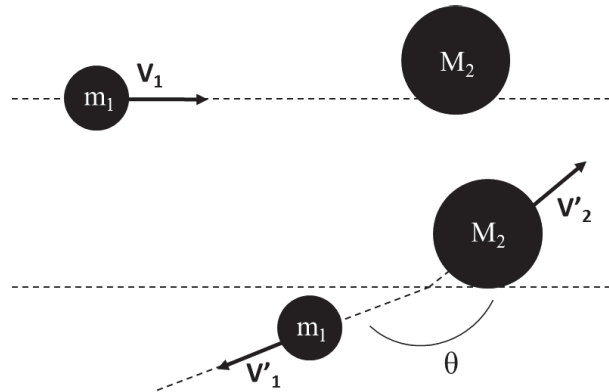


Figure 1.18 – Schematic view of the scattering process observed by RBS. A particle of mass m_1 with an initial velocity \mathbf{V}_1 is scattered with an angle θ after an encounter with a particle of mass M_2 . Both particles present non-zero velocity \mathbf{V}'_1 and \mathbf{V}'_2 , respectively, after the scattering process.

As the nucleus has no initial velocity, i.e. no initial energy, and the energy $E = (1/2)mV^2$, we can write the energy conservation law :

$$\frac{1}{2}m_1\mathbf{V}_1 = \frac{1}{2}m_1\mathbf{V}'_1 + \frac{1}{2}M_2\mathbf{V}'_2 \quad (1.42)$$

From this, the energy E of the scattered particle after the interaction with the target can be developed as :

$$E = k^2E_0 \quad (1.43)$$

with E_0 the energy of the incident particle before hitting the target and k a kinematic factor expressed as :

$$k = \frac{m_1 \cdot \cos \theta + (M_2^2 - m_1^2 \cdot \sin^2 \theta)^{1/2}}{m_1 + M_1} \quad (1.44)$$

where θ stands for the scattered angle, m_1 the mass of the incident particle and M_2 the mass of the target atom. From these equations, the maximum sensitivity is obtained in the backscattering geometry.

The selectivity of the technique, i.e. the differentiation of the target atoms by their mass, depends on two main parameters : the mass of the incident particles m_1 and their energy E_0 . Indeed, the heavier the incident particle is, the better the selectivity. Moreover, the equation 1.43 implies that the selectivity will be better for higher energies.

The sensitivity of the technique, i.e. the number of atoms encountered during the measurements, also depends on the energy and the nature of the incident particles. The number of backscattered particles N is given by :

$$N = N_i \cdot N_c \cdot \frac{d\sigma}{d\Omega} \cdot \Delta\Omega \quad (1.45)$$

with N_i the number of incident particles, and N_c the number nucleus by surface units (at.cm^{-2}). The differential cross section over the solid angle $\Delta\Omega$, can be expressed by :

$$\frac{d\sigma}{d\Omega} = \left(\frac{Z_1 Z_2 e^2}{8\pi\epsilon_0 E_0} \right)^2 \frac{\left(\cos \theta + \sqrt{1 - \left(\frac{m_1}{M_2} \sin \theta \right)^2} \right)}{\sin^4 \theta \sqrt{1 - \left(\frac{m_1}{M_2} \sin \theta \right)^2}} \quad (1.46)$$

where $e = 1.6 \times 10^{-19} \text{C}$ is the elementary charge. From the cross-section, the more the energy of the incident particle increases, the more the sensitivity decreases. Moreover, if the size of the incident particles or target atoms increases, then, according to the dependency on $(Z_1 Z_2)^2$ of the cross-section, the sensitivity increases.

Therefore, to get the best sensibility and sensitivity, a compromise must be found between the energy and the nature of the incident particles. In our case, Helium ions (He^+) were accelerated up to an energy of 2.50 MeV and 3.00 MeV using the particle accelerator at the Institut de Physique Nucléaire at Lyon (IPNL). The detector is a silicon diode oriented at 172° from the incident beam.

Figure 1.19 presents a typical RBS spectrum for a thin layer composed of heavy elements b deposited on a thick substrate, composed of an element a of atomic number Z_a lower than Z_b . The high energy band (blue) corresponds to the layer, whose width depends on its thickness. The highest energy part of the band is linked to the surface of the layer. The band at lower energy (orange) corresponds to the substrate. As the substrate is composed of lighter elements, its energy is lower than the one of the layers. An additional shift of the beginning of the step is due to the depth that the incident ions have

to cross before interacting with the substrate. The energy of the step for the substrate can be expressed as $E'_a = k^2 E_l$, with E_l the energy of the incident particles after going through the thin layer of thickness l . The SIMNRA software developed by [Mayer et al., 1999], allows to extract compositions and surface density (at.cm^{-2}) of the compounds analyzed from the spectrum recorded on the instrument.

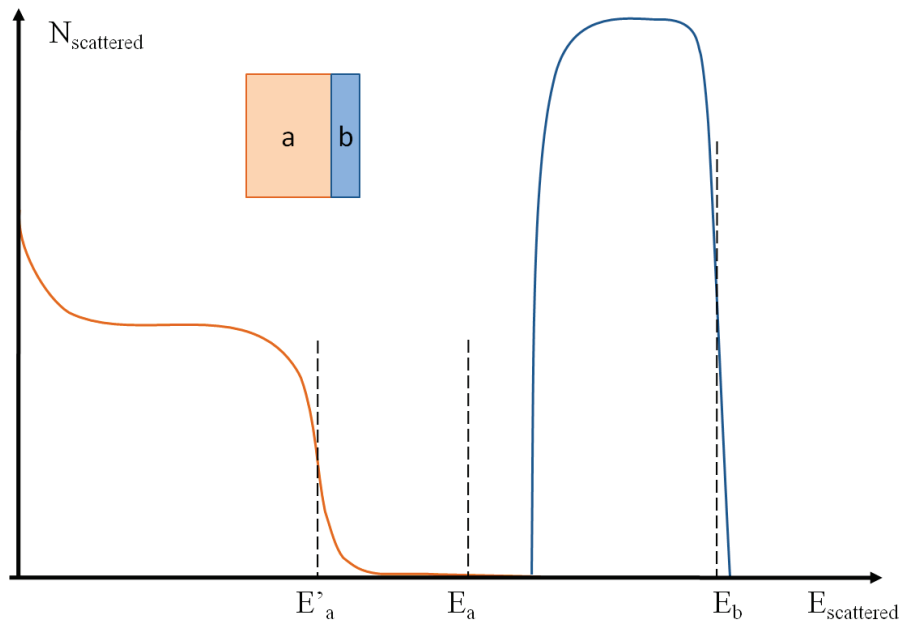


Figure 1.19 – Typical spectrum for a thin layer composed of a heavy element b on a thick substrate a with $Z_a < Z_b$. The energy $E'_a = k^2 \cdot E_l$, with E_l the energy of the incident particles after going through the thin layer of thickness l .

From the simulated surface density of the layer α (given in at.cm^{-2}) and its composition, the density can be extracted via :

$$\alpha = \frac{N_A \cdot N}{M} \rho \cdot e \quad (1.47)$$

with N_A the Avogadro's number, N the number of atoms, M the molar mass (g.mol^{-1}), ρ the density (g.cm^{-3}) and e the thickness of the layers (cm).

To summarize, the energy of the backscattered particles depends on the mass and depth of the encountered atoms. The number of scattered particles at a given energy depends on the number of scattering atoms in the target and allows to get the concentration of an element depending on the depth in the target. The main advantage of the Rutherford Backscattering technique is its sensitivity to heavy elements, but the mass resolution is decreasing when Z is increasing. The best case is when we have a heavy element in light surroundings, which makes the technique perfect to analyze the concentration in Ti and Ta atoms surrounded by oxygen atoms.

1.7 Conclusion

The GWD mirrors are thin non-crystalline layers deposited by Ion Beam Sputtering. In this work, the samples studied will be separate layers composed of SiO_2 , Ta_2O_5 and TiO_2 -doped Ta_2O_5 , deposited by Ion Beam Sputtering on fused silica substrates. The mechanical losses are measured via the resonant method with a GeNS setup at the Laboratoire des Matériaux Avancés. To characterize the structure and look for a microstructural origin of the thermal noise, Raman, Brillouin and ATR-FTIR spectroscopic techniques will be used. The vibrational spectroscopies probe the structure at short and medium range order with Raman and ATR-FTIR method, and the elastic properties of the material with the Brillouin scattering. The in situ high pressure experimental setup used later on was also presented.

In the next part, characterization of the low index material composing the mirrors, SiO_2 coatings, will be explored, followed in the last chapter by the characterization of the high-index material, namely Ta_2O_5 and TiO_2 -doped Ta_2O_5 . To estimate the TiO_2 dopant concentrations, Rutherford Backscattering spectroscopic measurements will be introduced.

Bibliography

- [Adhikari, 2014] Adhikari, R. X. (2014). Gravitational radiation detection with laser interferometry. *Reviews of Modern Physics*, 86(1):121.
- [Ager III and Drory, 1993] Ager III, J. W. and Drory, M. D. (1993). Quantitative measurement of residual biaxial stress by Raman spectroscopy in diamond grown on a Ti alloy by chemical vapor deposition. *Physical Review B*, 48(4).
- [Aspelmeyer et al., 2014] Aspelmeyer, M., Kippenberg, T. J., and Marquardt, F. (2014). Cavity optomechanics. *Reviews of Modern Physics*, 86(4):1391.
- [Brillouin, 1922] Brillouin, L. (1922). Diffusion of light and x-rays by a transparent homogeneous body. *Ann. Phys.(Paris)*, 17:88.
- [Cadez and Abramovici, 1988] Cadez, A. and Abramovici, A. (1988). Measuring high mechanical quality factors of bodies made of bare insulating materials. *Journal of Physics E: Scientific Instruments*, 21(5):453.
- [Callen and Welton, 1951] Callen, H. B. and Welton, T. A. (1951). Irreversibility and generalized noise. *Physical Review*, 83(1):34.
- [Cesarini et al., 2009] Cesarini, E., Lorenzini, M., Campagna, E., Martelli, F., Piergiovanni, F., Vetrano, F., Losurdo, G., and Cagnoli, G. (2009). A “gentle” nodal suspension for measurements of the acoustic attenuation in materials. *Review of Scientific Instruments*, 80(5):053904.
- [Chervin et al., 1995] Chervin, J., Canny, B., Besson, J., and Pruzan, P. (1995). A diamond anvil cell for ir microspectroscopy. *Review of scientific instruments*, 66(3):2595–2598.
- [Coussa-Simon, 2008] Coussa-Simon, C. (2008). *Étude du verre d’oxydes LBG : des propriétés optiques non linéaires au comportement sous haute pression*. PhD thesis, Université Claude Bernard Lyon 1.
- [Deschamps, 2009] Deschamps, T. (2009). *Étude des déformations élastique et plastique des verres de silice et silico-sodo-calciques sous hautes-pressions hydrostratigiques et indentation par spectrométrie Raman*. PhD thesis, Université Claude Bernard Lyon 1.

- [Elliott, 1992] Elliott, S. R. (1992). A unified model for the low-energy vibrational behaviour of amorphous solids. *EPL (Europhysics Letters)*, 19(3):201.
- [Ferraro, 2003] Ferraro, J. R. (2003). *Introductory raman spectroscopy*. Academic press.
- [Fresillon, 2016] Fresillon, C. (2016). Lma/cnrs photothèque.
- [Geiger and Marsden, 1909] Geiger, H. and Marsden, E. (1909). On a diffuse reflection of the α -particles. *Proceedings of the Royal Society of London. Series A, Containing Papers of a Mathematical and Physical Character*, 82(557):495–500.
- [Gilroy and Phillips, 1981] Gilroy, K. S. and Phillips, W. A. (1981). An asymmetric double-well potential model for structural relaxation processes in amorphous materials. *Philosophical Magazine B*, 43(5):735–746.
- [Girard, 2016] Girard, A. (2016). *Étude du confinement acoustique dans des nanostructures métalliques et semiconductrices par diffusion Raman basse fréquence*. PhD thesis, Université Claude Bernard Lyon 1.
- [Granata et al., 2015] Granata, M., Balzarini, L., Degallaix, J., Dolique, V., Flaminio, R., Forest, D., Hofman, D., Michel, C., Pedurand, R., Pinard, L., Sassolas, B., Straniero, N., Teillon, J., and Cagnoli, G. (2015). Internal friction and young’s modulus measurements on SiO₂ and Ta₂O₅ films done with an ultra-high Q silicon-wafer suspension. *Archives of Metallurgy and Materials*, 60(1):365–370.
- [Granata et al., 2016] Granata, M., Saracco, E., Morgado, N., Cajgfinger, A., Cagnoli, G., Degallaix, J., Dolique, V., Forest, D., Franc, J., Michel, C., et al. (2016). Mechanical loss in state-of-the-art amorphous optical coatings. *Physical Review D*, 93(1):012007.
- [Gross, 1930] Gross, E. (1930). Change of wave-length of light due to elastic heat waves at scattering in liquids. *Nature*, 126(201):400.
- [Harry et al., 2002] Harry, G. M., Gretarsson, A. M., Saulson, P. R., Kittelberger, S. E., Penn, S. D., Startin, W. J., Rowan, S., Fejer, M. M., Crooks, D. R. M., Cagnoli, G., Hough, J., and Nakagawa, N. (2002). Thermal noise in interferometric gravitational wave detectors due to dielectric optical coatings. *Classical and Quantum Gravity*, 19(5):897.
- [Kessler et al., 2012] Kessler, T., Hagemann, C., Grebing, C., Legero, T., Sterr, U., Riehle, F., Martin, M., Chen, L., and Ye, J. (2012). A sub-40-mhz-linewidth laser based on a silicon single-crystal optical cavity. *Nature Photonics*, 6(10):687–692.

- [Klotz et al., 2009] Klotz, S., Chervin, J.-C., Munsch, P., and Marchand, G. L. (2009). Hydrostatic limits of 11 pressure transmitting media. *J. Phys. D: Appl. Phys.*, 42(7):75413.
- [Li et al., 2014] Li, T., Aguilar Sandoval, F. A., Geitner, M., Bellon, L., Cagnoli, G., Degallaix, J., Dolique, V., Flaminio, R., Forest, D., Granata, M., Michel, C., Morgado, N., and Pinard, L. (2014). Measurements of mechanical thermal noise and energy dissipation in optical dielectric coatings. *Physical Review D - Particles, Fields, Gravitation and Cosmology*, 89(9):1–8.
- [Ludlow et al., 2015] Ludlow, A. D., Boyd, M. M., Ye, J., Peik, E., and Schmidt, P. O. (2015). Optical atomic clocks. *Reviews of Modern Physics*, 87(2):637.
- [Mao et al., 1978] Mao, H., Bell, P., Shaner, J. t., and Steinberg, D. (1978). Specific volume measurements of Cu, Mo, Pd, and Ag and calibration of the ruby R1 fluorescence pressure gauge from 0.06 to 1 Mbar. *Journal of applied physics*, 49(6):3276–3283.
- [Martinis et al., 2005] Martinis, J. M., Cooper, K., McDermott, R., Steffen, M., Ansmann, M., Osborn, K., Cicak, K., Oh, S., Pappas, D., Simmonds, R., et al. (2005). Decoherence in josephson qubits from dielectric loss. *Physical Review Letters*, 95(21):210503.
- [Mayer et al., 1999] Mayer, M., Duggan, J. L., Stippec, B., and Morgan, I. L. (1999). SIM-NRA, a simulation program for the analysis of NRA, RBS and ERDA. In *AIP Conference Proceedings*, volume 475, pages 541–544. AIP.
- [Mermet, 1996] Mermet, A. (1996). *Nanostructure de verres de polymères et déformation plastique: apports de la diffusion Raman basse fréquence et de la diffusion inélastique de neutrons*. PhD thesis, Université Claude Bernard Lyon 1.
- [Neuville et al., 2010] Neuville, D. R., Henderson, G. S., Cormier, L., and Massiot, D. (2010). The structure of crystals, glasses, and melts along the cao-al₂o₃ join: Results from raman, al l-and k-edge x-ray absorption, and 27al nmr spectroscopy. *American Mineralogist*, 95(10):1580–1589.
- [Obraztsov et al., 2007] Obraztsov, A. N., Obraztsova, E. A., Tyurnina, A. V., and Zolotukhin, A. A. (2007). Chemical vapor deposition of thin graphite films of nanometer thickness. *Carbon*, 45(10):2017–2021.
- [Pauleau, 2001] Pauleau, Y. (2001). Generation and evolution of residual stresses in physical vapour-deposited thin films. *Vacuum*, 61(2):175–181.

- [Penn et al., 2006] Penn, S. D., Ageev, A., Busby, D., Harry, G. M., Gretarsson, A. M., Numata, K., and Willems, P. (2006). Frequency and surface dependence of the mechanical loss in fused silica. *Physics Letters A*, 352(1):3–6.
- [Raman and Krishnan, 1928] Raman, C. V. and Krishnan, K. S. (1928). A New Type of Secondary Radiation. *Nature*, 121(3048):501–502.
- [Rubin et al., 1957] Rubin, S., Passell, T., and Bailey, L. (1957). Chemical analysis of surfaces by nuclear methods. *Analytical Chemistry*, 29(5):736–743.
- [Rutherford, 1911] Rutherford, E. (1911). Lxxix. the scattering of α and β particles by matter and the structure of the atom. *The London, Edinburgh, and Dublin Philosophical Magazine and Journal of Science*, 21(125):669–688.
- [Sandercock., 1999] Sandercock., J. (1999). *Operator manual "Tandem Fabry-Pérot Interferometer"*, JRS Sci. Instrum. edition.
- [Saulson, 1990] Saulson, P. R. (1990). Thermal noise in mechanical experiments. *Physical Review D - Particles and Fields*, 42(8):2437–2445.
- [Schrader, 1995] Schrader, B. (1995). *Infrared and Raman Spectroscopy: Methods and Applications*, chapter 6.4.4.3. Wiley-VCH Verlag GmbH, Weinheim, Germany.
- [Sonneville et al., 2012] Sonneville, C., Mermet, A., Champagnon, B., Martinet, C., Margueritat, J., de Ligny, D., Deschamps, T., and Balima, F. (2012). Progressive transformations of silica glass upon densification. *The journal of Chemical Physics*, 137:124505.
- [Vacher et al., 2006] Vacher, R., Ayrinhac, S., Foret, M., Rufflé, B., and Courtens, E. (2006). Finite size effects in Brillouin scattering from silica glass. *Physical Review B*, 74:012203.
- [Zachariasen, 1932] Zachariasen, W. H. (1932). The atomic arrangement in glass. *Journal of the American Chemical Society*, 54(10):3841–3851.
- [Zarzycki, 1982] Zarzycki, J. (1982). *Les verres et l'état vitreux*. Masson.

Chapter 2

Silica glass

As we have seen earlier, the low refractive-index material used for the current Gravitational Wave detectors mirrors is Ion Beam Sputtered Silica glass (IBS-silica). At ambient temperature, fused silica presents mechanical losses of $\varphi \approx 5 \times 10^{-9}$, i.e. four orders of magnitude lower than any other non crystalline oxide [Topp and Cahill, 1996]. Yet, if amorphous silica is processed by Ion Beam Sputtering, the losses are much higher, up to $\varphi \approx 5 \times 10^{-4}$ [Principe et al., 2015] [Granata et al., 2016]. Even though silica glass is widely studied, the micro-structural origin and the mechanisms responsible for these differences in the dissipation mechanisms are still unknown. Therefore, the aim of this part is to explore a possible connection between the structure of silica thin films and the mechanical losses.

In this chapter, the IBS-silica structure will be presented and compared to the fused silica structure. Then, the evolution through different fabrication and annealing parameters will allow us to exhibit structural parameters linked with the mechanical losses of this material.

2.1 Silica Glass structure

Fused silica glass has been widely studied over the past 50 years, and the basic aspects of its structure are well defined. The molecular structure of fused silica glass in connection with its Raman spectrum will be presented here, and then compared to the structure of IBS-silica and densified fused silica.

2.1.1 Molecular structure

Even though the glasses have no long-range order, a structure can be defined for the first neighbours at short (1-5 Å) and medium range order (5-20 Å).

At short range order, silica glass is organized as SiO_4 tetrahedra. These basic units are defined by their intra-atomic length $l_{\text{Si-O}} = 1.62 \text{ \AA}$ and dihedral angles $\widehat{\text{O-Si-O}}$,

$\phi = 109.5^\circ$ [Rino et al., 1993, Jin et al., 1994].

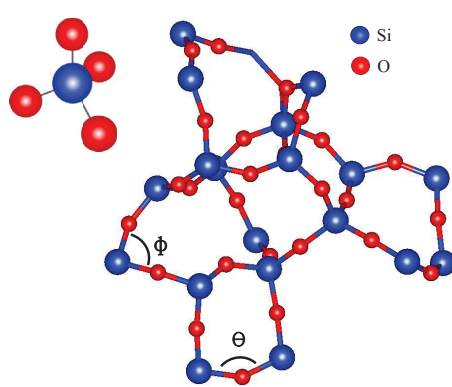


Figure 2.1 – Schematic molecular structure of silica glass and of the basic unit SiO_4 [T. Damart, ILM].

At medium range order, tetrahedra are randomly arranged in rings from 3 to 9 SiO_4 units with the distribution centered on 6-membered rings as shown on figure 2.2 [Jin et al., 1994]. The inter-tetrahedral angles are included between 120° and 180° , with the mean $\text{Si}-\text{O}-\text{Si}$ angle in fused silica at $\theta = 149^\circ \pm 11^\circ$ [Weigel et al., 2016].

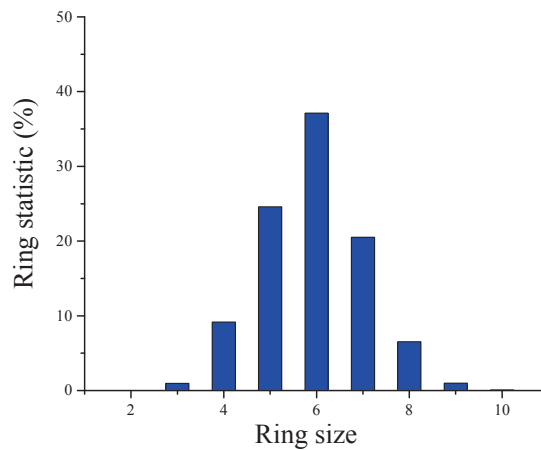


Figure 2.2 – Ring statistics for fused silica as derived from simulation [Jin et al., 1994].

The Raman spectrum of melt-quenched pure silica glass can be seen on the following figure 2.3. As seen earlier in Chapter 1.4.2, the Raman scattering intensity is linked with the vibrational density of states of the studied sample.

The spectroscopic features, seen on the Raman spectra, correspond to specific vibrations, giving information on the structure at short and medium range order. For silica

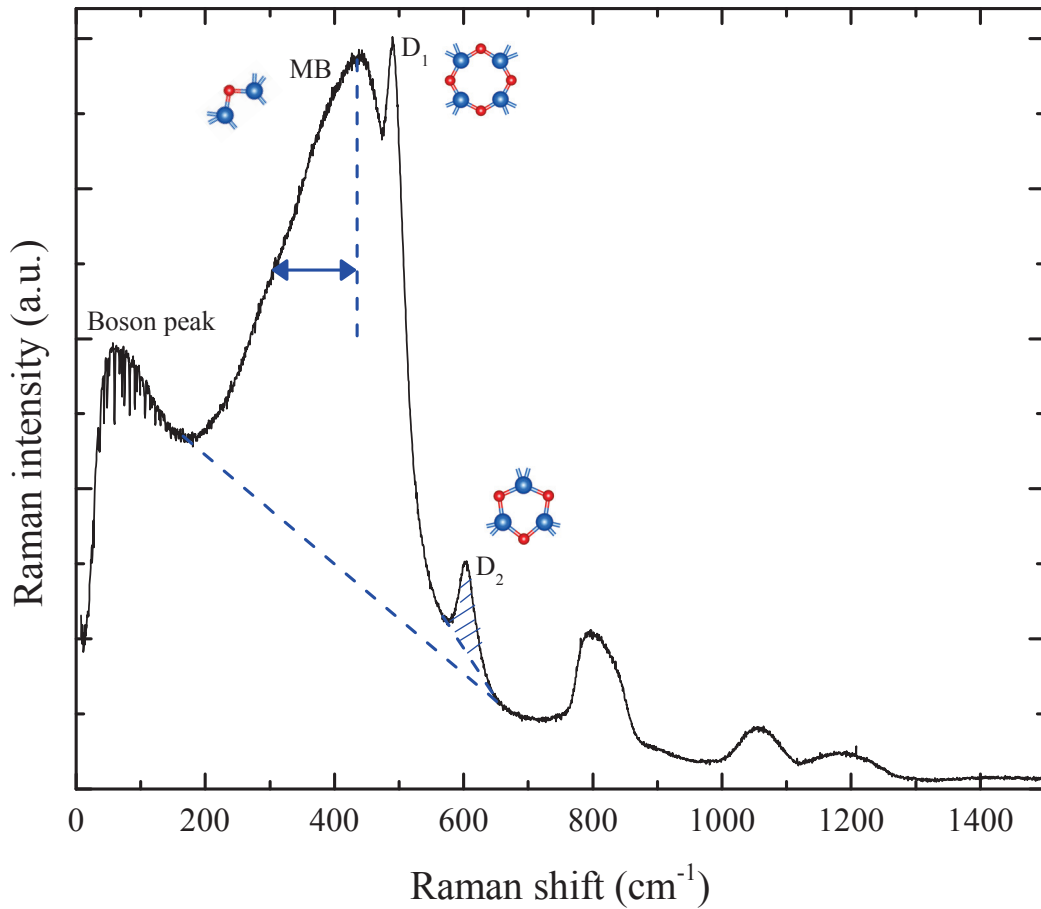


Figure 2.3 – Raman spectrum of fused silica glass (Suprasil 300).

glass, the spectrum on figure 2.3 presents a band at low frequency centered at 60 cm^{-1} . An asymmetric band exists around 440 cm^{-1} and is adjoined by two narrower bands at 490 cm^{-1} and 600 cm^{-1} . At higher frequencies, three larger bands of smaller intensities are present around 800 cm^{-1} , 1060 cm^{-1} and 1200 cm^{-1} .

The history of the band attribution for silica glass, summarized by McMillan, 1984, will not be discussed here. Only the mainly accepted attributions will be presented. The band around 440 cm^{-1} is called the main band (MB), corresponding to the Si-O-Si angle bending mode [Hehlen, 2010]. Using the central force model, the main band position can be linked to the mean value of the $\widehat{\text{Si-O-Si}}$ angle distribution [Sen and Thorpe, 1977] by :

$$\nu_{\text{MB}}^2 = \frac{\alpha_{\text{Si-O}}}{M_{\text{O}}} \times (1 + \cos \theta_{\text{Si-O-Si}}) \quad (2.1)$$

With $\alpha_{\text{Si-O}}$ the central force constant, for a fused silica glass at ambient pressure with a

density of 2.2 g cm^{-3} , $\alpha_{\text{Si-O}}$ is equal to $1.622 \times 10^{-7} \text{ g mol}^{-1} \text{ cm}^{-2}$ [Sen and Thorpe, 1977]. M_{O} is the Oxygen atom mass, ν_{MB} the position of the main band (cm^{-1}) and $\theta_{\text{Si-O-Si}}$ the inter-tetrahedral angle.

The bands at 490 cm^{-1} and 605 cm^{-1} are called "defect bands", D_1 and D_2 . These bands have long been described as attributed to the breathing modes of 4 and 3-membered rings respectively [Galeener and Mikkelsen, 1981].

On figure 2.3, the blue arrow indicates the measurement of the Half Width at Half Maximum of the Main band. The D_2 band area measured along this work corresponds to the hatched area normalized to the main band, D_1 and D_2 total area. The details of the signatures characterization are detailed in the appendix.

The quite large spectroscopic feature around 800 cm^{-1} is still a subject of controversy. Following McMillan, 1984, this band is attributed either to Si-O stretching or O-Si-O symmetric stretching. The two bands at 1060 cm^{-1} and 1200 cm^{-1} are attributed to LO-TO asymmetric Si-O stretching modes of the Si-O-Si bond [Sato and McMillan, 1987].

The low frequency band, centered at 60 cm^{-1} , is called the boson peak. This characteristic of disordered materials corresponds to an excess of vibrational density of states compared to the Debye theory. This excess was observed from specific heat measurements [Pohl, 1981] and low temperature thermal conductivity [Anderson, 1981, Zeller and Pohl, 1971], before being also evidenced by neutron - or light - inelastic scattering [Buchenau et al., 1984].

The origin of this anomaly is still on debate and different models were proposed to explain the excess of vibrational density of states in the amorphous solids [Karpov et al., 1983, Galperin et al., 1987, Buchenau et al., 1992, Elliott, 1992, Monaco et al., 2006].

In this thesis, the interpretation of the Boson peak will be based on the empirical model developed by Eugène Duval, based on the concept of a disrupted elastic network Duval et al., 1990. The Boson peak would have a structural origin linked to the presence of elastic inhomogeneities (approximately a few nanometer in size) in the amorphous structure (figure 2.4). In a few words, the vibrational modes of these inhomogeneities, corresponding to the intrinsic vibration frequency of these nanodomains, lead to a mode accumulation, then to a density of states excess, called the Boson peak. According to this model, the intensity of the Boson peak would be linked to the contrast between the cohesive domains and their surroundings: the higher the intensity of the Boson peak, the higher the contrast.

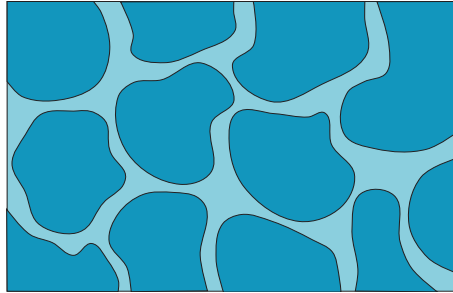


Figure 2.4 – Schematic illustration of a disrupted elastic network according to the model of Duval et al., 1990. Darker area correspond to nanometric inhomogeneities with higher elastic constants.

2.1.2 Comparison between fused silica and Ion-Beam sputtered thin layers

The amorphous silica of interest in this work is deposited by Ion Beam Sputtering (IBS), and its structure shows some drastic differences with the structure of fused silica.

Spectra of two fused silica and one sputtered silica are presented on figure 2.5. The second fused silica (in grey) is a recovered densified fused silica from hydrostatic cold compression up to 14 GPa, with a density of 2.46 g cm^{-3} . The comparison shows that the synthesis process has a strong impact on the glass structure, the IBS-silica featuring some similarities with densified fused silica.

The main band of sputtered silica is narrower and shifted towards higher frequencies than fused silica. Indeed, the main band for sputtered silica is centered at $477 \pm 1 \text{ cm}^{-1}$ with a half width at half maximum (HWHM), measured on the low frequency side of this band, about $69 \pm 5 \text{ cm}^{-1}$ compared to fused silica with a HWHM about $120 \pm 5 \text{ cm}^{-1}$ and centered at $434.7 \pm 0.5 \text{ cm}^{-1}$.

The Main Band HWHM and position of the sputtered layer are closer to the one of densified by cold compression silica ($\rho = 2.46 \text{ g cm}^{-3}$), which presents a HWHM of $60 \pm 4 \text{ cm}^{-1}$ and a position centered at $486 \pm 1 \text{ cm}^{-1}$. As shown by equation (2.1), the Main Band position of IBS-silica corresponds to an intertetrahedral angle $\widehat{\text{Si-O-Si}} = 140.7^\circ$, lower than the 144° of fused pristine silica. Martinet et al., 2015 found a similar angle value for bulk silica densified through hot compression (5 GPa, 750°C), with a 2.5 g cm^{-3} density. These two signatures, Main Band position and HWHM, are consistent with a denser structure of the deposited thin films. Indeed, the density of the layers can be deduced from the Main Band HWHM using the curve on figure 2.6 [Martinet et al., 2015]. The density was evaluated at $\rho = 2.37 \pm 0.02 \text{ g cm}^{-3}$ via this method, in agreement with the values directly estimated at $\rho = 2.33 \pm 0.04 \text{ g cm}^{-3}$ through measurements of the coating mass via a balance, and of the thickness (with a J. A. Woollam

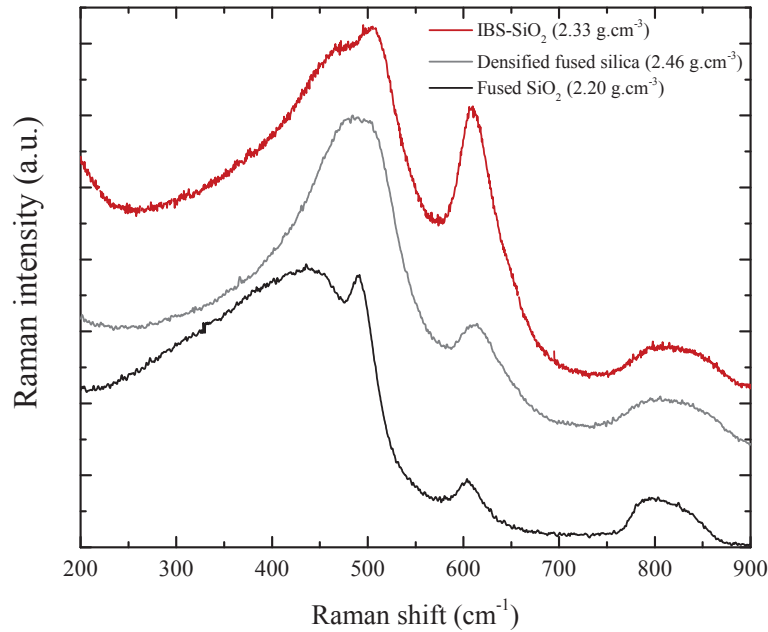


Figure 2.5 – Raman spectra of fused silica glass [2.20 g cm^{-3}](blue), densified fused silica [2.46 g cm^{-3}] (grey) and silica deposited by ion beam sputtering [2.33 g cm^{-3}](red).

VASE spectro-ellipsometer).

All of these spectroscopic indications, added to the direct measurement of the density, highlight the fabrication of dense silica structures by Ion Beam Sputtering compared to the melt-quenched silica.

The IBS silica glass also shows a strong overlap of the main band and of the D_1 band, and more intense defect bands which are also shifted towards higher frequencies compare to fused silica. As seen on figure 2.2, the ring statistics of fused silica is peaked on 6-membered rings. The normalized D_2 area of sputtered silica, with respect to the Raman spectrum area from 230 cm^{-1} to 700 cm^{-1} , is about 6 times larger than in fused silica, and also larger than the one of densified fused silica. The normalized D_2 area was shown by [Pasquarello and Car, 1998, Burgin et al., 2008] to be linked to the 3-membered ring population. A large area of this band indicates a less relaxed structure than in fused silica [Jin et al., 1994, Dávila et al., 2003]. Martinet et al., 2015 showed that for silica densified by hot compression, the D_2 band remains very small, while for densification via cold compression the area gets larger. Opposed to cold compression, the hot compression process allows the glass structure to relax during the augmentation of pressure. Then, the structure obtained through cold compression would be more stressed than the

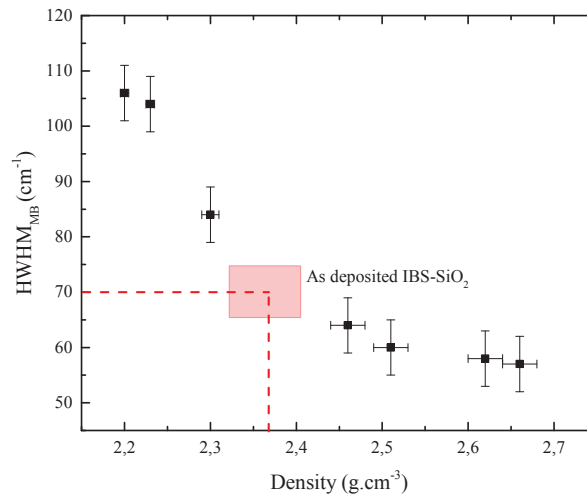


Figure 2.6 – HWHM of the Main Band for fused silica permanently densified via cold compression compared to their density from Martinet et al., 2015. The Main Band HWHM of the sputtered silica is highlighted in red. By referring to this curve, the density of the sputtered layers should be between 2.35 g cm^{-3} and 2.40 g cm^{-3}

one retrieved after hot compression and the D_2 band area was explained as a signature of this stress. Moreover, simulations show that shear stress implies a transformation of large rings into smaller ones [Shcheblanov et al., 2015]. This is particularly visible with an increase of the three-membered ring population, highlighted in Raman spectroscopy by an increase of the D_2 band area. This large relative area of the sputtered silica D_2 band then indicates over-stressed layers (internal stress as defined by Johari, 2014).

The D_2 band corresponding to the breathing mode of 3-membered rings, the Sen and Thorpe model (see equation 2.1) can also be applied to calculate the $\widehat{\text{Si-O-Si}}$ angle with the position of the band [Hehlen, 2010]. Using this method, the shift of 6.4 cm^{-1} towards higher frequencies indicates a threefold ring puckering, related with a 0.5° decrease of the $\widehat{\text{Si-O-Si}}$ mean angle.

Spectroscopic measurements point to a sputtered layer structure denser and over-stressed compared to fused silica. These results are consistent with previous studies showing that Ion Beam Sputtering deposition produces highly densified silica coatings [Hirose et al., 2006] [Weiss et al., 1996] [Martin et al., 1983] [Sainty et al., 1984]. The $\widehat{\text{Si-O-Si}}$ angle distribution is narrower and the corresponding average angle is smaller, the structure is closer to densified fused silica glass. The high intensity of the D_2 band seems also to be an important signature of the deposited silica, highlighting stressed layers.

As the mechanical losses of fused silica are four orders of magnitude lower than the one of sput-

tered silica [Topp and Cahill, 1996], a sputtered layer with a structure as close as possible to fused silica is desirable. In order to investigate how to reduce the stress and the density of the layers, a detailed analysis of the deposition parameter, thickness and annealing parameters, was conducted.

2.2 Effects of the processing method

2.2.1 Interaction between substrates and silica layers

The Ion-Beam sputtered silica of interest is deposited on a metallic tantalum tablet (figure 2.7), in order to eliminate any interfering silica substrate Raman signal as metallic tantalum has no active modes in Raman spectroscopy. In order to rule out any possible interpretation of future results in terms of interface effect, spectroscopic measurements were conducted on the same silica sample deposited on two different substrates : fused silica and metallic Tantalum.

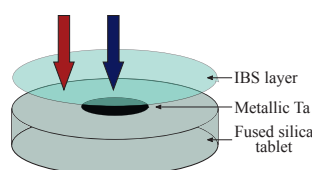


Figure 2.7 – Schematic view of a typical sample : an Ion Beam Sputtered layer is deposited on top of a fused silica tablet with an interfacial metallic Tantalum layer. The arrows indicate the two areas analyzed for comparison: layer on fused SiO_2 (red) or on metallic Ta (blue).

The limited thickness of the layers (between 1 and 3 μm) prevents an effective analysis of Raman spectra for the sputtered silica deposited on a fused silica substrate. The Raman spectra seen on figure 2.8 are obtained with the LabRAM HR spectrometer with a $\lambda = 532 \text{ nm}$ wavelength, a x100 OLYMPUS lens and a confocal hole set up at 75 μm . As shown by the differences between the spectra on figure 2.8, the Raman response of the layer cannot be clearly separated from the signal from the fused silica tablet. The Raman spectrum of IBS-silica deposited on fused silica does not correspond to the spectrum of the layer deposited on metallic Tantalum. The main band contribution from the substrate deforms the main band of the layer and prevents further analysis.

To check any substrate effect on the deposited glass, samples were then analyzed by ATR-FTIR spectroscopy allowing only the first micrometer to be probed compared to the 3 μm thick coating. Figure 2.9 displays infrared measurements conducted on the same sample, either deposited on a metallic tantalum tablet or a fused silica substrate. Following Zhang et al., 2015, the band at 800 cm^{-1} corresponds to the bending vibration of Si-O-Si bridges. The two superposed spectroscopic features around 1030 cm^{-1} and 1130 cm^{-1} are interpreted respectively in terms of transverse-optic (TO) and longitudinal-optic (LO) components of the asymmetric stretching vibration of Si-O-Si bonds.

The normalized two spectra show no differences between the two layers, indicating no structural differences at short distances. Therefore as the substrate has no structural impact on the

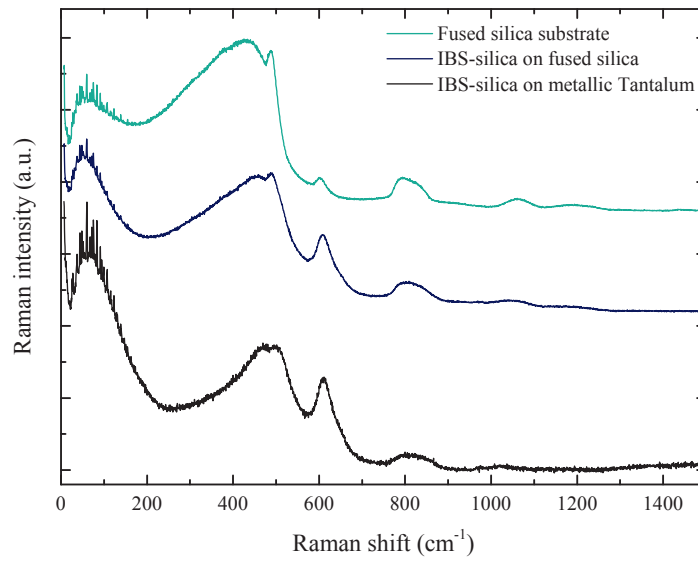


Figure 2.8 – Raman spectra of Ion Beam Sputtered silica layers deposited on metallic Tantalum (black) or on fused silica (dark blue) compared to the fused silica substrate spectrum (light blue).

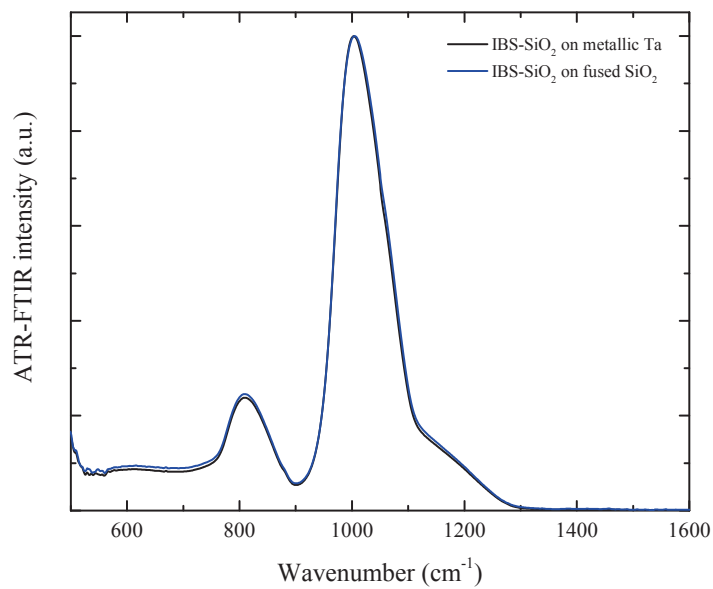


Figure 2.9 – ATR-FTIR spectra of 3 μm silica layers deposited on metallic tantalum (black) and on fused silica substrate (blue). Spectra are normalized to 1 for comparison.

layers, Raman measurements will be conducted for the silica layers on metallic tantalum tablets.

2.2.2 Deposition parameters effects

From [Topp and Cahill, 1996], mechanical losses of fused silica are four order of magnitude lower than many other oxides at room temperature. However, in order to get Bragg mirrors with the optical specification needed in the Gravitational Wave Interferometers, the IBS technique proved to be the most efficient. As seen earlier in 2.1.2, the structures of IBS and fused silica present some differences, and the aim of this part is to find out how we can improve the deposition parameters in order to get an IBS-silica with a structure as close as possible to the one of fused silica.

In the deposition process, a few parameters can be tuned to change the structure of the deposited compound. As seen in Chapter 1.2, the voltage and the intensity of the source of the coater allow to tune the energy and the flux of the atoms deposited on the substrate, respectively.

To understand the effect of these source parameters, 800 nm thick samples were deposited with the Spector for different source voltages V_b (V) and intensities I_b (mA) on fused silica substrates. Table 2.1 presents the four samples deposited using the Spector coater and their source parameters. The sample S16001 corresponds to the standard parameters used for every other sample deposited with the Spector in this thesis.

Sample name	Voltage V_b (V)	Intensity I_b (mA)
S16001 (std)	1250	600
S16009	1500	400
S16011	1500	700
S16013	250	150

Table 2.1 – Sample names and the corresponding source parameters (Voltage and Intensity) used for their processing. The S16001 (std) corresponds to the standard conditions used for the deposition of all the Spector samples studied in this work, if not specified otherwise.

The Raman spectra of these samples (figure 2.10) present differences depending on the source parameters. The D_2 band exhibits the high intensity characteristic of the sputtered silica layers, with still some variations which are dependent on the source intensity. The position and intensity of the boson peak are also changing with the different parameters of the source. The main band position, width and shape are evolving with the different kinds of silica layers. The most significant changes due to the differences in

the source parameters come from the sample S16009, which present a Raman spectrum with an uncommon shape compared to the others.

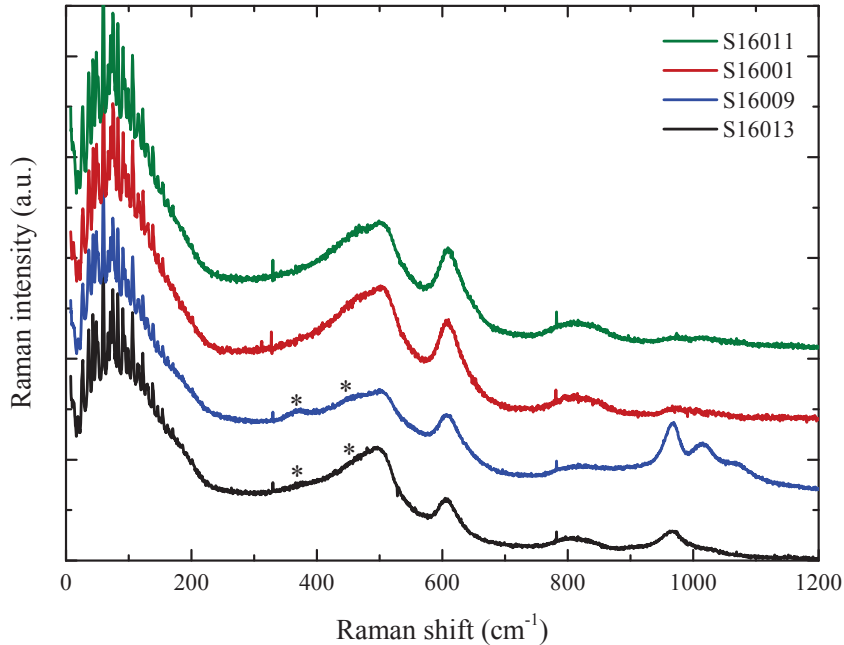


Figure 2.10 – Raman spectra of Spector silica layers deposited with different source parameters : S16013 in black ($I_b = 150$ mA), S16009 in blue ($I_b = 400$ mA), S16001 in red ($I_b = 600$ mA) and S16011 in green ($I_b = 700$ mA). The asterisks shows the position of the Molybdenum signatures due to the contamination of the layers in the fabrication process.

The following analysis of the deposition parameters is focusing on the evolution of the structure with different source intensities.

For the two samples with the lowest source intensity, S16009 and S16013, bands around 1000 cm^{-1} are clearly developed in contrast to the high source intensity deposited layers. These bands can be explained by two different ways. The grids accelerating the argon ions are made from Molybdenum. If the ion beam is not well focused, molybdenum atoms are pulled off and contaminate the deposited substrate. The signature around 1000 cm^{-1} could be coherent with this kind of contamination as Raman bands of this element can appear at this frequency, corresponding to stretching modes of the MoO_3 structure. Two bands at 360 cm^{-1} and 490 cm^{-1} (shown by the asterisks on figure 2.10) are also noticeable and are characteristic of the Molybdenum, corresponding to Mo-O bending modes [Thielemann et al., 2011, Thielemann and Hess, 2013, Verbruggen

et al., 1994, Payen et al., 1992]. A 3 μm silica sample (annealed 70 hours at $T_a = 500^\circ\text{C}$) with a small band around 1000 cm^{-1} was analyzed by Rutherford Backscattering (IPNL) (figure 2.11). A small plateau is visible at the expected channels corresponding to atoms around the Molybdenum size, reinforcing the hypothesis of a Molybdenum contamination of the samples. This signature could also come from Si-OH bonds forming at the surface of the samples after the deposition process. [Mulder and Damen, 1987] showed that vibrations at 980 cm^{-1} can be due to symmetric stretch vibrations of silanol groups. However, in the case of silanol groups, this signature must be coupled with a band at 3750 cm^{-1} characteristic of the O-H vibrations. This was verified by ATR-FTIR and no spectroscopic signatures were found at the frequencies corresponding to -OH bonds vibrations. The spectroscopic feature around 1000 cm^{-1} is then most probably linked to a Molybdenum contamination of the layers, coherent with the fact that this band seems to be only dependent on the source parameters.

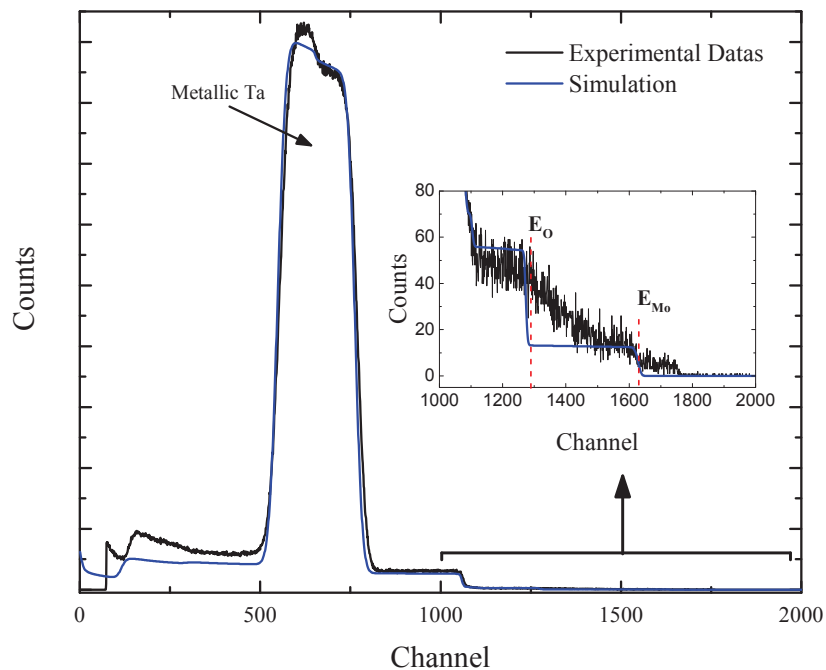


Figure 2.11 – RBS spectrum of a sputtered SiO_2 3 μm thick Spectror sample, annealed at $T_a = 500^\circ\text{C}$ during 70 hours. The area of interest is presented in the inset, with the blue line corresponding to simulations done with the SIM-NRA software, and in black the experimental results. The step corresponding to Molybdenum is shown by the E_{Mo} line, and E_{O} corresponds to the Oxygen step.

Raman bands evolution

From figure 2.10, one can see the difficulty to extract reliable quantitative positions and HWHM for the main band. Also, due to the high quantity of Molybdenum, the quantitative analysis of the Main Band proves to be even more difficult for the sample S16009. However, qualitatively we can observe on figure 2.10 a shift of the Main Band and D_1 positions for the sample S16013, deposited with the lowest source intensity.

Figure 2.12 presents the evolution of the D_1 band position as a function of the coater source intensity. When the source intensity increases, the D_1 band shifts towards higher frequencies, indicating a tendency of the 4-membered rings to shrink as the intensity increases. The large error bar on the S16009 sample comes from the deformation of the main band due to the non-trivial quantity of Molybdenum in the layer.

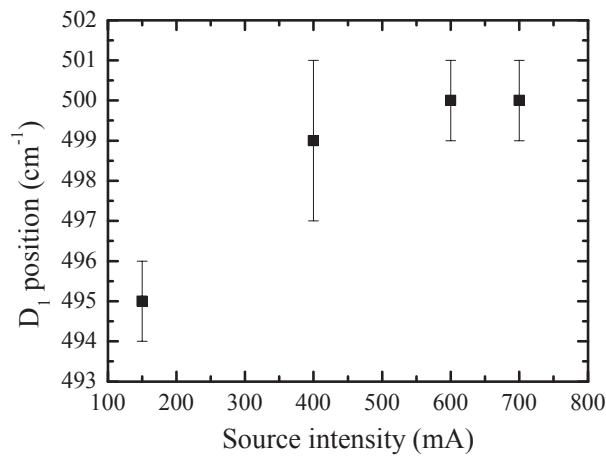


Figure 2.12 – D_1 band position following the intensity of the source.

The evolution of the D_2 band position and relative area are depicted on figure 2.13 and present a correlation with the source intensity. Indeed, its position shifts towards lower frequencies with lower source intensities, indicating an opening of the 3-membered rings structure. The relative area of the D_2 band is also correlated with the source intensity. The higher the source intensity, the higher the three-fold population, indicating a highly stressed structure [Martinet et al., 2015].

Figure 2.14 presents the evolution of the position and Raman intensity of the Boson peak for different source intensities. The position of the band does not seem to evolve with the source intensity, the only exception coming from the sample S16009 whose position is 11 cm^{-1} lower than the other samples. Unlike the position, the Raman intensity of the Boson peak is clearly correlated with the source intensity. When the intensity of the coater source decreases, the Boson peak intensity also decreases, corresponding to a smaller contrast between the cohesive domains, hence a more homogeneous elastic disorder.

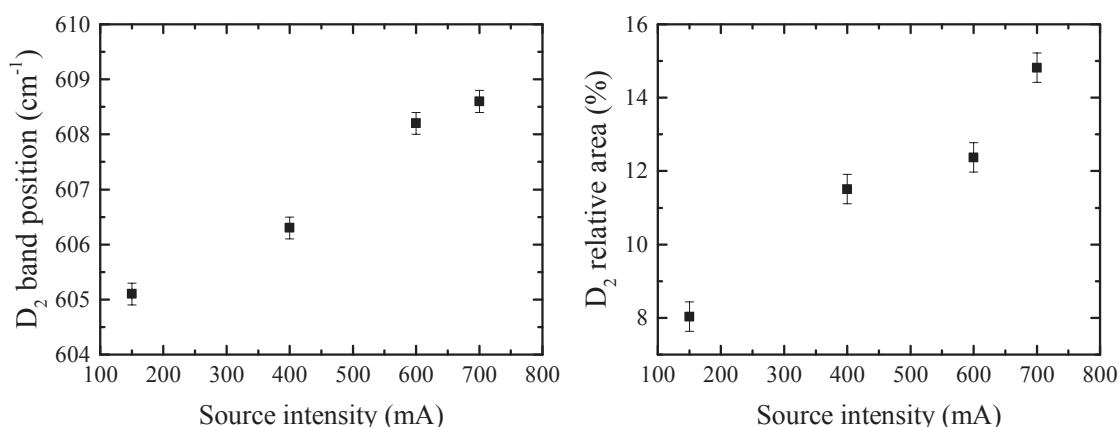


Figure 2.13 – Position and area of the D₂ band compare to the intensity of the Coater's source.

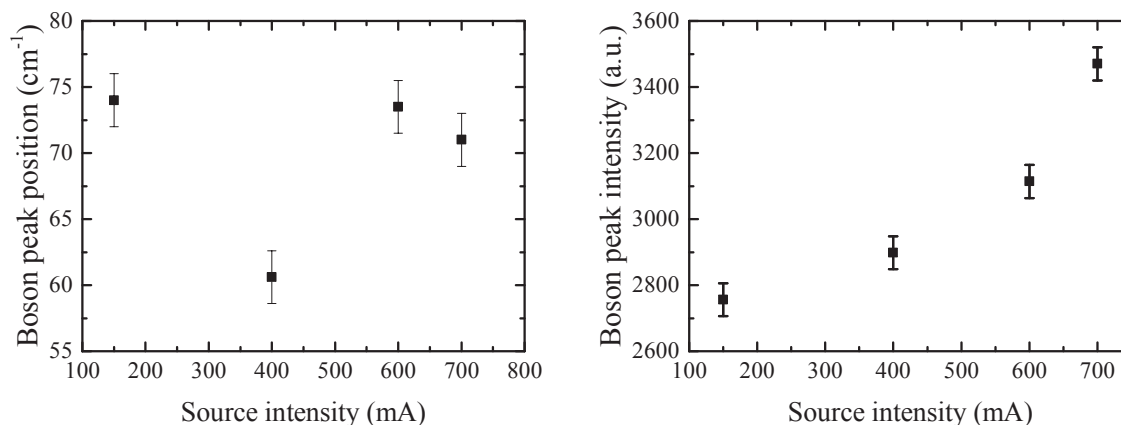


Figure 2.14 – Boson peak position and intensity compared to the Spector's source intensity.

These results show the effect of the intensity of the coater source on the structure. A low intensity seems to induce a more relaxed structure, with a smaller population of three-membered rings compared to high intensity deposition. A link seems to exist between the internal stress of the structure and the coater source intensity. However, the sample studied are deposited with different source voltage, and a more systematic study is needed. The focusing of the beam exiting the source is also essential to avoid any contamination of the samples by Molybdenum, the presence of this element inducing a strong deformation of the Raman spectra.

2.3 Effect of the annealing on the structure

Due to the fabrication processes of glasses or amorphous solids, residual stress are usually present in the solid's structure. For quenched glasses, this stress comes mainly from the differences between the cooling rates at the surface and inside the glass [Zarzycki, 1982]. In the case of physical vapor deposition, thermal stresses comes from different thermal expansion coefficients between substrates and coatings, while intrinsic stresses may originate from the distortion of the surface of the coatings due to the bombardment of energetic particles [Pauleau, 2001]. The most common way to reduce these stresses is to apply a thermal treatment to the produced non-crystalline solid. The annealing is usually done at a temperature close to the transformation temperature during a time long enough to allow the elimination of the stresses [Zarzycki, 1982].

Concerning the mirror coatings, after the deposition process the layers are annealed at $T_a = 500^\circ\text{C}$ during ten hours. This annealing, at a temperature much lower than the glass transition temperature of the fused silica glass $T_g = 1200^\circ\text{C}$, induces a stabilization of the optical properties, with a decrease of the layers absorption and mechanical losses [Penn et al., 2003].

As the annealing is reducing the losses, we studied the effect of this thermal treatment to look at a possible microscopic origin of the losses. Two samples deposited in different coaters were annealed and the evolution of the different spectroscopic signatures characteristic of the structure are compared to the mechanical losses.

2.3.1 Annealing of a Spector sample

The annealing was repeated for a $3\ \mu\text{m}$ thick sample of ion beam sputtered silica with 6 cumulative annealing times, ranging from 5 to 305 hours.

Figure 2.15 presents the evolution of the mechanical losses of the coatings depending on the annealing time. As measured by the Gentle Nodal Suspension (Chapter 1.3.2), the global losses of the coating sample are obtained by averaging the results of the mechanical characterization with respect to the mode frequency for each annealing time. The mechanical losses exhibit a quick decrease (80 %) during the first few hours, and seem to be decreasing at a slower rate even after 305 hours of annealing. Since the coating losses decrease with annealing, the structure was probed by Raman, Brillouin and Infrared spectroscopies to find if there is a structural microscopic origin of the losses.

The Raman spectra of these thermally treated silica layers are presented in figure 2.16. As a general trend, the annealing induces lower relative intensities for the boson peak and the D_2 band. The boson peak width increases with the annealing time, coupled with a shift of its position towards higher frequencies. All the remaining spectroscopic signatures of interest (MB, D_1 , D_2) are shifting towards lower frequencies, and the main

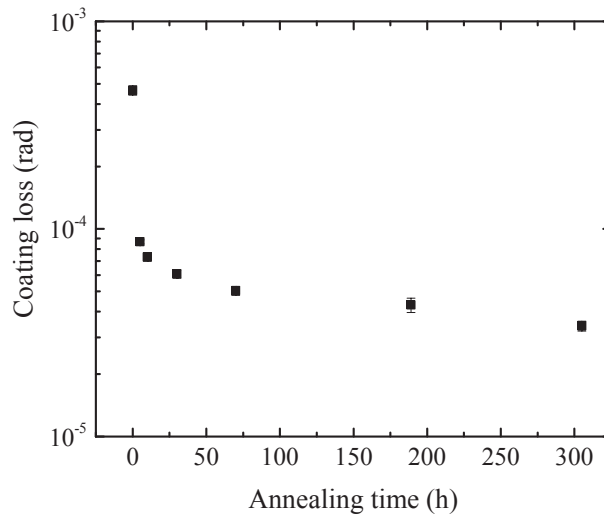


Figure 2.15 – Mechanical losses of the silica layer for the not annealed sample and six different annealing times ranging from 5 to 305 hours.

band width increases with annealing. After the first annealing, a band appears around 950 cm^{-1} . This signature could be assigned to Si-OH bonds, appearing due to the annealing under normal atmosphere.

Spectroscopic signatures evolution

Figure 2.17 displays the evolution of the main band position with annealing. It shows a significant shift towards low frequencies over the first 30 hours, then slows down to be still decreasing after 305 hours. The position goes from $477 \pm 3\text{ cm}^{-1}$ for the as-deposited film to $466 \pm 1\text{ cm}^{-1}$ after 305 hours of annealing. According to equation 2.1, it corresponds to an increase of the intertetrahedral angles from 140.7° to 141.6° . This Si-O-Si angle opening can be linked to a density decrease [Martinet et al., 2015]. The quite large error bars for these values come from the fact that the D_1 band is not clearly separated from the main band. On figure 2.17 the Half-Width at Half Maximum (HWHM), measured on the low frequency side of the main band, demonstrates a rapid increase during the first few hours, reaching a plateau around $83 \pm 3\text{ cm}^{-1}$. Compared to fused silica which displays a HWHM around 120 cm^{-1} , the layers exhibit a small intertetrahedral angle distribution and the annealed films are more homogeneous in terms of intertetrahedral angles. From figure 2.6, an increase of the Main Band HWHM implies also a density decreasing. Indeed, from a $\rho_0 = 2.37 \pm 0.03\text{ g cm}^{-3}$ estimated before annealing, the density extracted from this calibration after annealing is $\rho_{annealed} = 2.32 \pm 0.02\text{ g cm}^{-3}$. The angle opening of the intertetrahedral angles and its distribu-

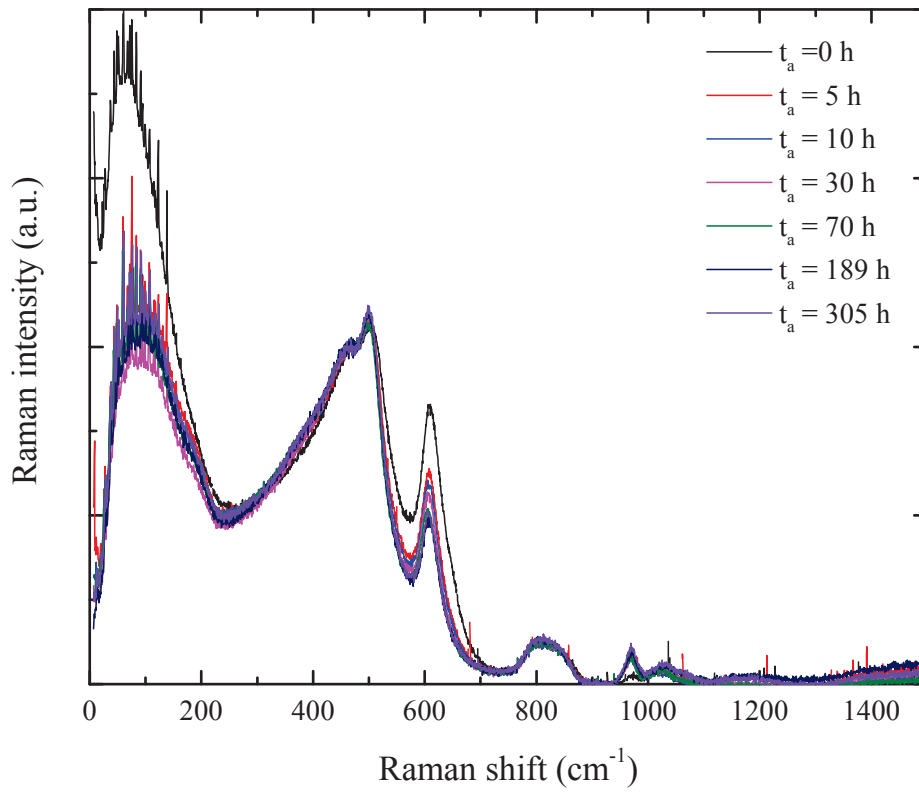


Figure 2.16 – Raman spectra of layers annealed at $T_a = 500\text{ °C}$ (5h = red, 10h = blue, 30h = pink, 70h = green, 189h = dark blue, 305h = violet) compared to the one of an as-deposited layer (in black) and normalized by the main band intensity.

tion may be linked to the mechanical losses. However, due to large error bars, no clear correlation could be defined, especially for the Main Band position.

The evolution of the D_1 and D_2 band positions with annealing are presented on figure 2.18. The D_2 position is shifted from $610 \pm 1\text{ cm}^{-1}$ before annealing to $607 \pm 1\text{ cm}^{-1}$ after 305 hours. Though very weak (0.5%), this shift toward lower frequencies is significant and is explained by an opening of the threefold rings structure.

The evolution of the four-membered rings signature (figure 2.18) is more difficult to quantify, since the D_1 band is not clearly separated from the main band, leading to larger error bars. The annealing also induces for this D_1 band a weak shift toward lower frequencies. After only 30 hours a plateau is reached at $499 \pm 1\text{ cm}^{-1}$, only 0.8% lower than the initial position at $503 \pm 2\text{ cm}^{-1}$. As for the D_2 band, a shift toward lower frequencies is explained by less puckered rings, four-fold structure in the case of the

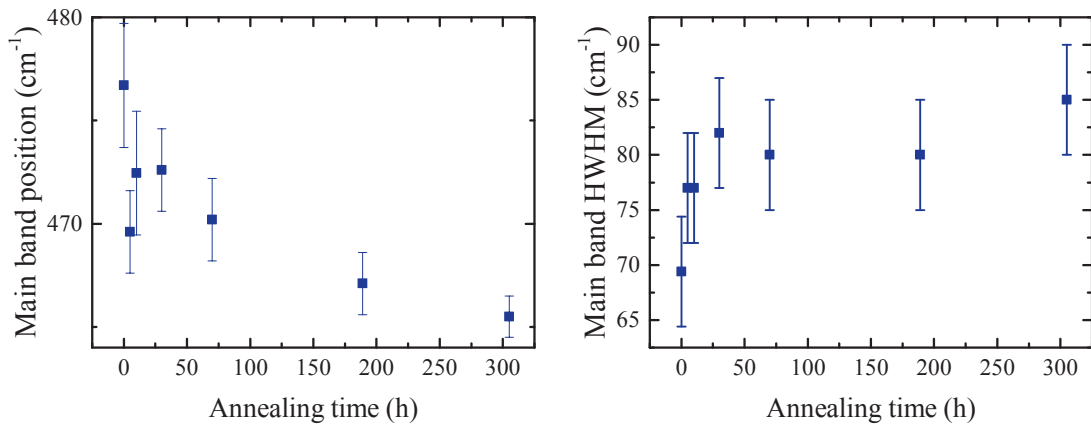


Figure 2.17 – Main band characteristics : position and Half-Width at Half-Maximum (HWHM) compared to the annealing time.

D_1 band. Due to large error bars on the D_1 band position, a correlation between this position and the coating losses is not clear.

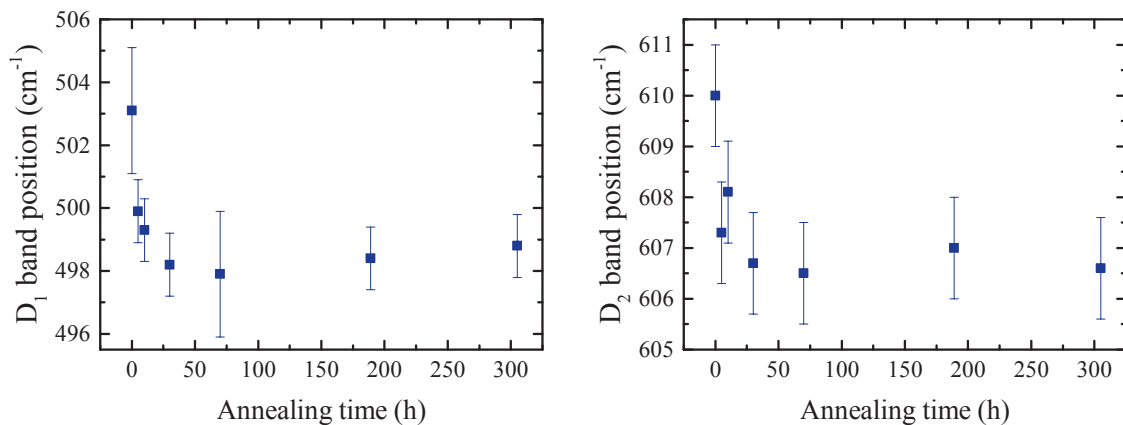


Figure 2.18 – Position of the D_1 and D_2 band following the annealing time.

The evolution of the relative D_2 band area normalized to the total area of the spectrum between 230 cm^{-1} and 700 cm^{-1} can be seen on 2.19 as a function of the annealing time and of the coating losses. This area is decreasing with annealing from $13.2 \pm 0.2\%$ to $6.4 \pm 0.2\%$ heading towards the value of fused silica at 2.3% . As we have seen earlier, the D_2 relative area is correlated to the 3-fold ring population, which means that the heat treatment of the layers leads to a significant diminution of this population. Indeed, during the first five hours of annealing, the relative area exhibits a 30 % decrease, reaching a 50 % decrease after a 305 hours heat treatment. The normalized D_2 area decrease follows a stretched exponential law, with $\tau = 6.3 \pm 1.1\text{ h}$. In contrast with the evolution of

the main band characteristics, the D_2 area presents a clear non trivial correlation with the coating losses. The larger the area of the D_2 band, the higher the coating losses. This correlation is however hindered by the relaxation rates for these two mechanisms. Indeed, when fitted by a stretched exponential function, the mechanical losses exhibit a relaxation time $\tau = 5 \pm 2$ minutes, much smaller than the 6 hours calculated from the D_2 area evolution.

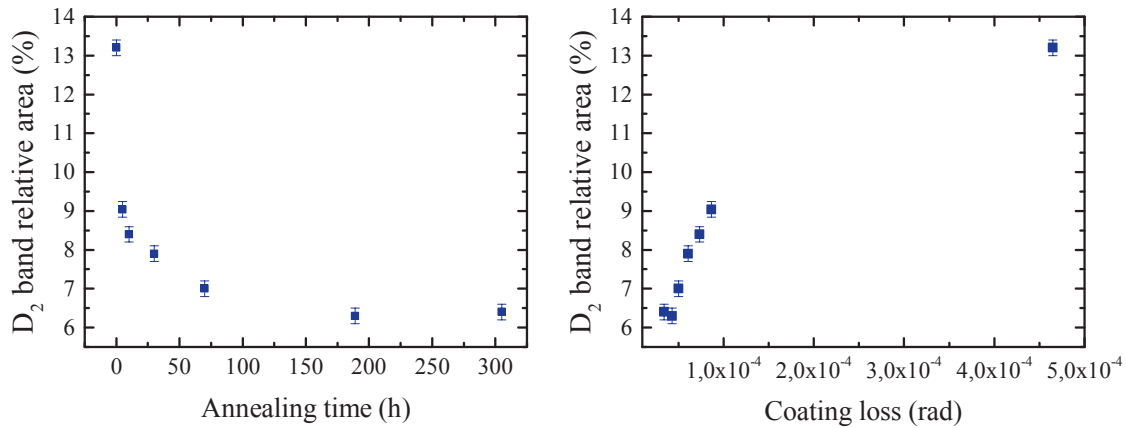


Figure 2.19 – D_2 band relative area as a function of the annealing time and coating losses.

Recent molecular-dynamics simulations [Hamdan et al., 2014] established that mechanical losses come from the twisting of chains of few tens of SiO_4 tetrahedra, with each one flipping with respect to its neighbors via rotation and stretching of Si-O bonds. Figure 2.20 shows the structure involved in this transition, with the involved atoms exhibited in colors. Between 10 and 100 atoms could be involved in this reorganization, which allows the system to explore the potential energy landscape and achieve lower local potential energy minima. However, no investigation of the ring population inside these chains was done yet.

The relaxation mechanisms that are active in energy dissipation at room temperature and at acoustic frequencies should have a barrier height of about 0.5 eV [Gilroy and Phillips, 1981]. From [Barrio et al., 1993, Shimodaira et al., 2006], the activation energy of the three-membered rings was measured around 0.43 eV. Annealing could reduce the density of metastable states with a barrier of 0.5 eV, by increasing the number of states with a lower activation energy. This is also suggested by the increase of the D_1 intensity, corresponding to an increase of the 4-membered ring population having an activation energy $E_a = 0.14$ eV [Galeener, 1985]. The correlation between the evolution of the D_2 area and the mechanical losses could be explained by these similar activation energies. However, there is an important difference between the characteristic evolution

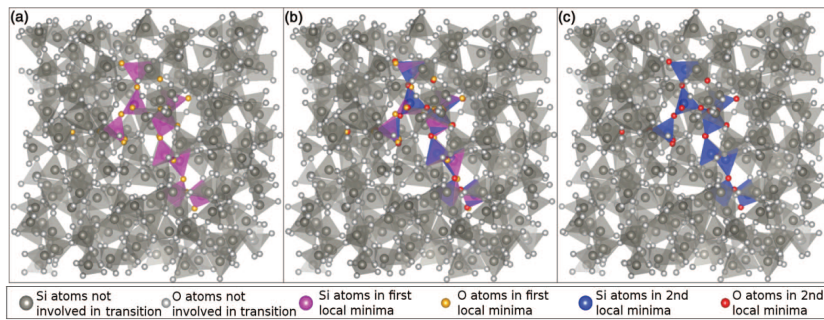


Figure 2.20 – Simulations conducted by [Hamdan et al., 2014], showing the configuration of the local minima for a two level system of silica involving 21 atoms. The Si atoms and O atoms in grey are not involved in the transition. (a) represents the atoms in their first local energy minima. (c) represents the second minimum of the same atoms and (b) highlights the two configurations differences by overlaying them.

times with annealing, suggesting that the mechanical losses are not exclusively driven by the 3-membered rings.

Figure 2.21 shows the evolution of the Boson peak for different annealing times. The evolution is a decrease of the relative intensity coupled with a slight shift towards higher frequencies with annealing. [Deschamps, 2009] showed that a fused silica glass, densified by cold compression, presents a Boson peak shifted towards higher frequencies while its intensity decreased. With the annealing, we would then expect a shift towards lower frequencies as the density of the layers decreases. However, on figure 2.22, the low frequency band position of the annealed layers is shifting towards higher frequencies with cumulative annealing time.

The relative area of the Boson peak (figure 2.22) decreases during the first few hours of annealing, indicating that the layers gets more homogeneous in terms of elastic constants with the annealing. Contrary to the evolution of the position, the relative intensity is in agreement with the other measurements done by cold compression on fused silica glass. This result is nonetheless tempered by the changing intensity of the depression around 20 cm^{-1} . These differences between the not-annealed layer and the annealed layers could come from another contribution and could deform the results. Indeed, for energies slightly lower than the one of the Boson peak, a quasi-elastic signal can be measured in Raman spectroscopy. This signal, centered on 0 cm^{-1} , is associated with fast relaxations (close to picosecond) and gets more and more important when temperature increases [Terki et al., 1999].

To complete the structural characterization at a larger scale and look at the macroscopic properties, Brillouin measurements were also conducted on the annealed layers (spectra on figure 2.23). The position of the Brillouin peaks for each annealing

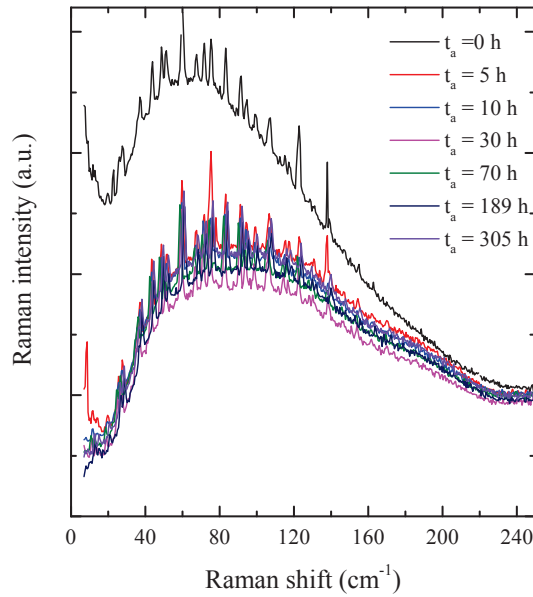


Figure 2.21 – Boson peak for every annealing time (5h = red, 10h = blue, 30h = pink, 70h = green, 189h = dark blue, 305h = violet) compared to the one of as-deposited layer (in black).

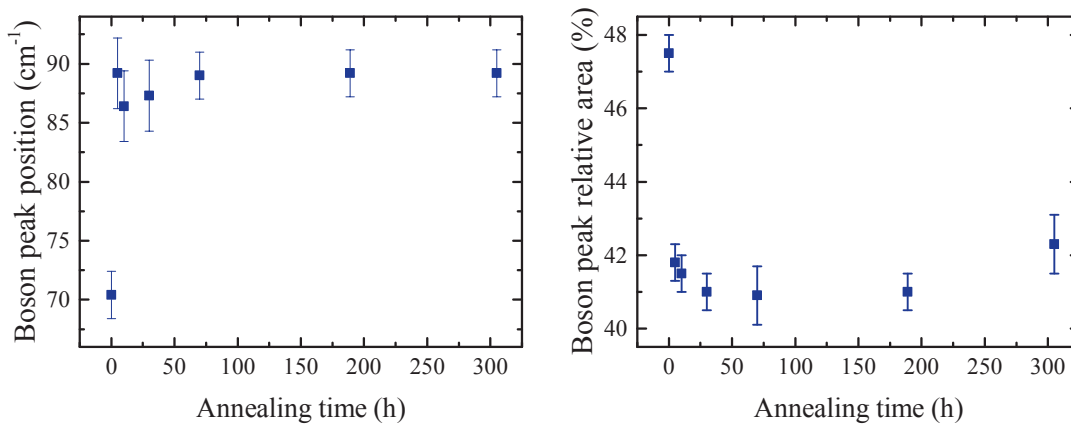


Figure 2.22 – Boson peak position and relative area as a function of the annealing time for the silica layers.

time are presented on figure 2.24 in parallel to their spectra compared to fused silica. The Brillouin peak position is shifting from 35.8 ± 0.1 GHz to 35.1 ± 0.1 GHz during the 305 hours of annealing, corresponding to a decrease of the longitudinal speed (eqn. 1.27). For comparison, the position of the Brillouin peak for fused silica is around 32.5 ± 0.1 GHz. The shift occurs faster during the first 30 hours of annealing than for

longer annealing times. As the density also decreases, from equation 1.28, the longitudinal elastic coefficient also decreases with increasing annealing time, however the error bars are too important for this evolution to be significant. Indeed, before annealing $c_{11} = 98 \pm 2$ GPa, when after a 10 hour annealing this value is only slightly lower with $c_{11} = 93 \pm 6$ GPa. These elastic coefficients are in agreement with the $c_{11} = 85 \pm 3$ GPa found by [Knapp et al., 2015] for silica deposited by physical vapor deposition and characterized by a density $\rho = 2.35 \pm 0.08$ g cm⁻³.

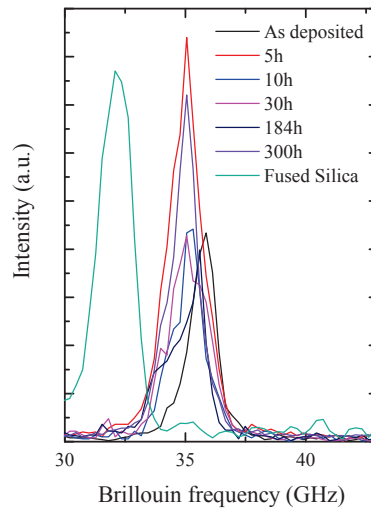


Figure 2.23 – Brillouin spectra of the annealed silica layers (5h = red, 10h = blue, 30h = pink, 189h = dark blue, 305h = violet) and the as-deposited layer (black), compared to fused-silica (light blue).

The infrared position measurements done on the samples are presented on figure 2.25, with the position of the band around 1000 cm⁻¹ corresponding to transverse-optic (TO) component of the asymmetric stretching vibration of Si-O-Si bridges [Zhang et al., 2015]. This band shifts towards higher frequencies with the annealing time, corresponding to an opening of the Si-O-Si angles [Hirose et al., 2006], in agreement with the results given by the main band position in Raman spectroscopy. Compared to the coating losses, this TO mode is shifting towards higher frequencies when the coating losses decreases. The evolution of the TO component could be linked to the mechanical losses by the Si-O-Si bonds between the SiO₄ tetrahedra reorganizing, corresponding to the SiO₄ chains flipping [Hamdan et al., 2014].

As IBS-SiO₂ presents a structure closer to densified fused SiO₂ than pristine fused SiO₂, and from the last results, table 2.2 compares the evolution of fused silica under

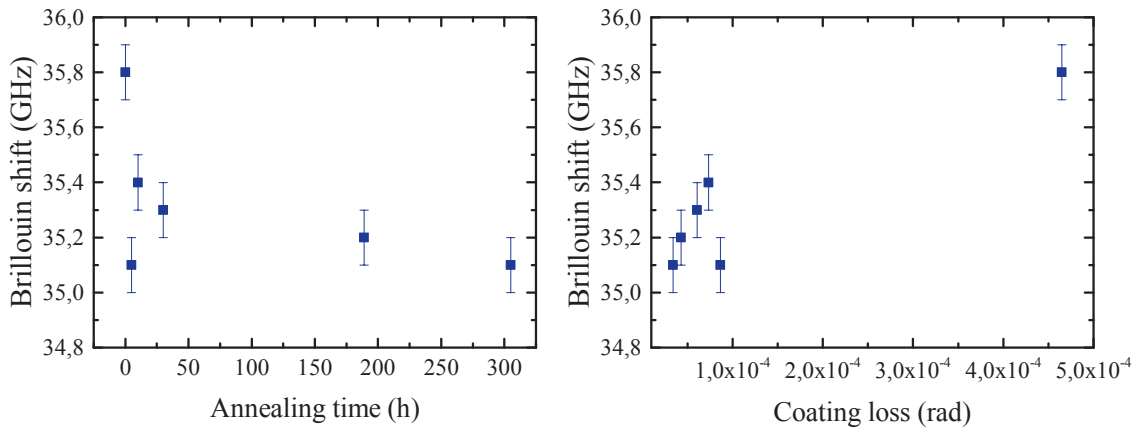


Figure 2.24 – Position of the Brillouin peak following the annealing time and the coating losses.

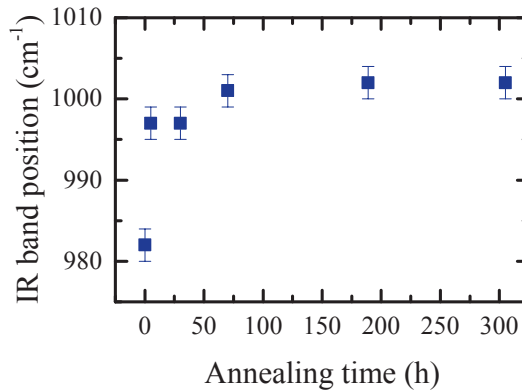


Figure 2.25 – Position of the 1000 cm⁻¹ Infrared band (TO asymmetric stretching of the Si-O-Si bonds) following the annealing time.

high pressure and IBS-silica with annealing. Every signature evolves in opposite direction as annealing induces a density decrease, while high pressure does the opposite. The only exception comes from the low frequency band. With compression, this band shifts towards higher frequencies and decreases in intensity, interpreted as a diminution of the inhomogeneities size and accompanied by an homogenization of the structure. The same effect is visible with the annealing of the IBS-silica glass, while the structure relaxes towards the structure of fused silica glass. The glass seems to become more homogeneous.

These structural evolutions are induced by an annealing at a temperature T_a much lower than the fused silica glass transition temperature T_g , during short times compared to usual relaxation times in silica glass. They indicates an over-stressed structure needing only low energy activation to reorganize itself. Following these results, the annealing induces a stress

	Fused Silica with High Pressure	IBS-silica with annealing
Main band position	↗	↘
Main band HWHM*	↘	↗
D ₁ position	↗	↘
D ₂ position	↗	↘
D ₂ area	↗	↘
Boson peak position	↗	↗
Boson peak intensity	↘	↘
Density	↗	↘

Table 2.2 – Comparison of the different silica spectroscopic signatures evolution between high pressure compression and annealing. As annealing and compression are opposite process, the spectroscopic signatures are expected to evolve in opposite directions. The only exception comes from the Boson peak evolution. Results on fused silica under compression are from [Deschamps, 2009]. *The MB HWHM is linked with the density as shown by Martinet et al., 2015.

relaxation with a decrease of the D₂ band added to an opening of the intertetrahedral angles and an homogenization in terms of elastic nanostructure of the silica layers. The mechanical losses seem to be followed by the 3-membered ring population, and maybe remotely by the intertetrahedral angles distribution.

2.3.2 Annealing of a Grand Coater sample

The annealing study was previously done on a 3 μm silica sample deposited using the Spector coater. Yet in Chapter 2.2.2, the impact of the source parameters and of the coater geometry were highlighted. To investigate how the evolution of the structure with annealing depends on the initial structure, the study formerly conducted on the 3 μm sample from the Spector was repeated on a 800 nm sample, deposited in standard conditions of the Grand Coater (GC). Measurements on Spector samples of different thicknesses were conducted and no thickness effects could be highlighted, the results are then only due to the deposition parameters.

The mechanical losses of the as-deposited GC sample, $\varphi_{GC} = 1.37 \pm 0.12 \times 10^{-4}$ are three times lower than the losses of the as-deposited Spector sample, $\varphi_S = 4.65 \pm 0.24 \times 10^{-4}$. The differences between the two coaters originate in the geometry of the setups. Indeed, with a volume of the Grand Coater chamber 20 times greater than the Spector, the atoms pulled off the target have a greater distance to cross before reaching the substrate, inducing different deposition parameters.

Figure 2.26 compares the Raman spectra of the previously studied Spector sample to the 800 nm thick sample from the Grand Coater. Both spectra have similar main band positions and HWHM. The Grand Coater layer also exhibits a more intense Boson peak shifted towards higher frequencies, corresponding to the same effect than densification, and a smaller D_2 band compared to the Spector thin film. These signatures may be interpreted in terms of a more relaxed structure for the layers deposited in the Grand Coater, added to a less homogeneous structure at the nanometric scale. An increased level of noise is noticeable on the Boson peak of the GC sample compared to the Spector, corresponding to the air spectrum, induced by the differences between the thicknesses of the samples.

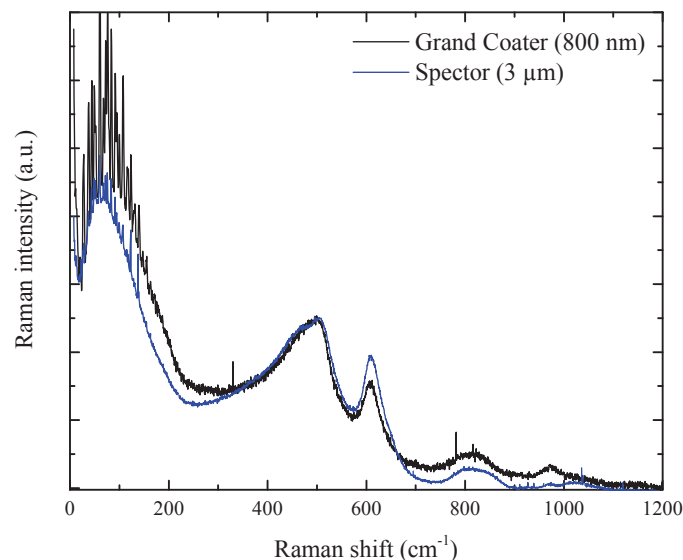


Figure 2.26 – Raman spectra of Grand Coater (GC) and Spector silica layers. The differences in the level of noise come from the different thicknesses of the two samples, the GC sample being three times thinner than the Spector one.

Figure 2.27 presents the Raman spectra of the samples annealed during different cumulative times of the Grand Coater silica. The evolution seems to be similar to that of the Spector annealed sample (figure 2.16), with the widening of the main band, the decrease of the D_2 band intensity and the increase of the D_1 intensity with annealing.

Figure 2.28 shows the evolution of the different spectroscopic features with annealing. Apart from the Boson peak, every spectroscopic signature analyzed presents no evolution after the first 5 hours of annealing. The main band position cannot be quantitatively measured with these samples as this signature overlaps with the D_1 band pre-

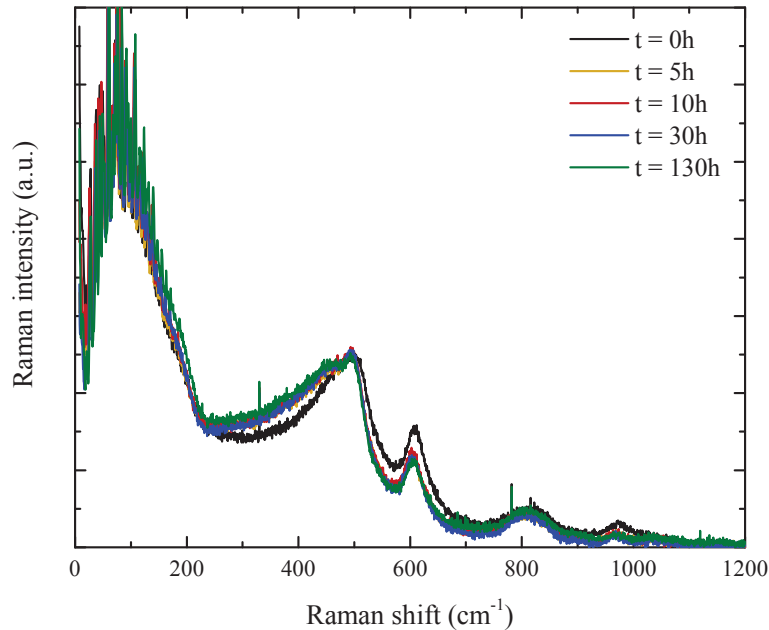


Figure 2.27 – Raman spectra of 800 nm silica layers deposited in the Grand Coater and annealed from 0 to 130 hours (Not annealed in black, 5 hours in yellow, 10h in red, 30h in blue, 130h in green).

venting any deconvolution of the main band position, or any quantitative analysis of the D_1 band relative intensity. If we compare the evolution of the Spector and the Grand Coater silica layers after 30 hours of annealing (table 2.3), the spectroscopic signatures evolve in similar ways. The annealing induces in both cases a small opening of the three and four membered rings with a population of the three-fold structures decreasing with the annealing, implying less stressed structures. In the case of the Grand Coater, only a 28% decrease is noticeable, smaller than the 40% decrease with the Spector sample, which can be explained by a more relaxed initial structure of the GC sample. The Boson peak position also presents a smaller relative shift with annealing, to reach approximately the same final position than the Spector samples. However, the Boson peak area does not evolve indicating no clear homogenization of the silica layer.

Figure 2.29 shows the area of the D_2 band for the non annealed Grand Coater sample and fused silica compared to the Spector sample, as a function of the coating losses. The correlation between the mechanical losses and the three-membered rings population still holds even with different kinds of silica.

These results are in agreement with the previous measurements on the $3\mu\text{m}$ sample de-

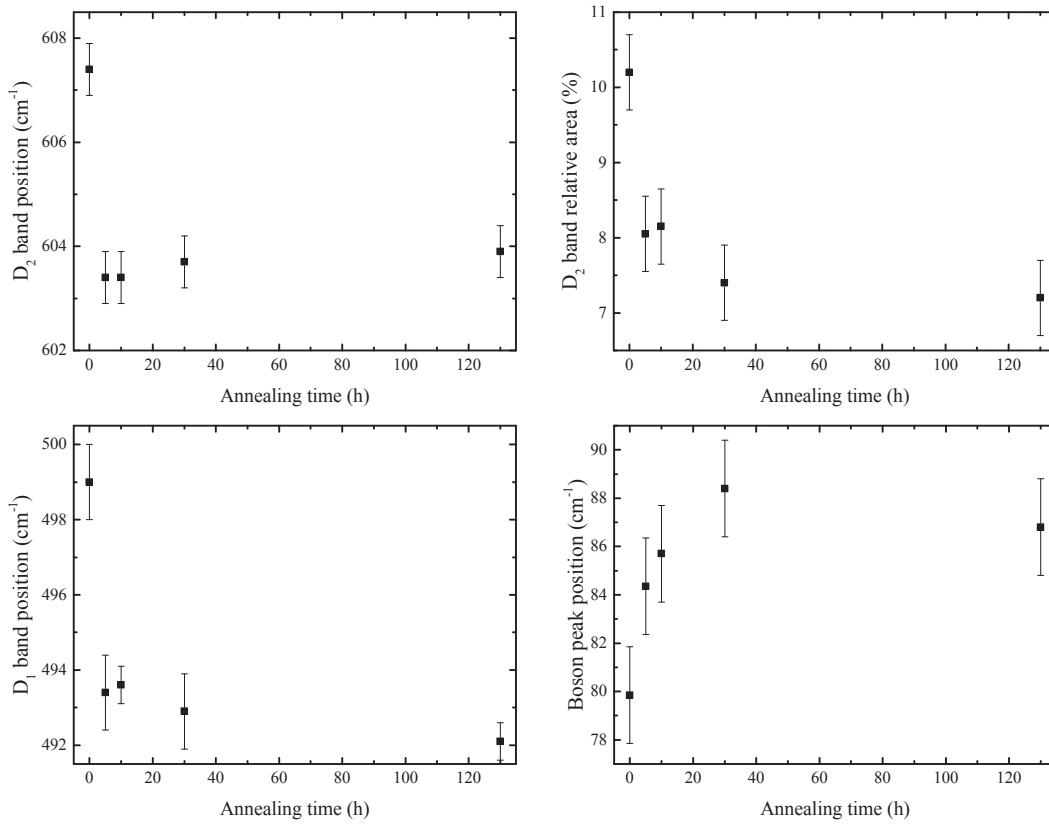


Figure 2.28 – Evolution of the position and relative area of the D₂ band for the 800 nm silica coating as a function of annealing (top). Position of the D₁ band and position of the Boson peak depending also on the annealing time (bottom).

posited in the Spector. The same evolution with annealing towards a more relaxed structure was highlighted with a ring statistics shifting towards larger rings. Moreover, the initial Grand Coater structure being more relaxed, it allows a final state, after the annealing, with a less stressed structure than at the end of the Spector sample's annealing.

	Spector		Grand Coater		Fused SiO ₂
	0h	30h	0h	30h	
D1 position (cm ⁻¹)	502 ± 3	498 ± 2	499 ± 1	493 ± 1	488.1 ± 0.2
	-0.8%		-1.2%		
D2 position (cm ⁻¹)	610 ± 1	607 ± 1	607.4 ± 0.5	603.7 ± 0.5	602.0 ± 0.2
	-0.5%		-0.6%		
D2 area (%)	13.2 ± 0.2	7.9 ± 0.2	10.2 ± 0.5	7.4 ± 0.5	2.0 ± 0.3
	-40%		-27.5%		
Boson peak position (cm ⁻¹)	70 ± 2	87 ± 3	80 ± 2	88 ± 2	60 ± 1
	+24%		+10.6%		

Table 2.3 – Evolution after 30 hours of annealing of the spectroscopic signature for the Spector and the Grand Coater silica layers, compared to the features of fused silica.

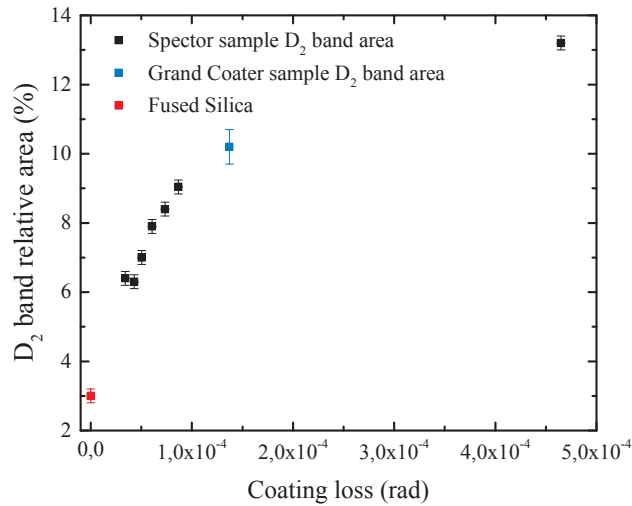


Figure 2.29 – Comparison between the D₂ area of the Spector silica layers (black), Grand Coater silica layers (red) and fused silica (red) following the mechanical losses.

2.3.3 Conclusion on the general effect of the annealing

The evolution with annealing of the structure of two silica layers deposited in different coaters were presented. An annealing at a temperature much lower than the glass transition temperature of the fused oxide, and during a short time compared to the usual relaxation times for fused oxides, is enough to cause a great evolution of the structure. Indeed, for both structures, the D_2 band area presents a strong decrease in only 5 hours, with every band position shifting towards lower frequencies, apart from the low frequency band evolving in the opposite direction. The Spector and Grand Coater silica layers present the same structural evolution with annealing. The ring statistics evolve with the annealing, the three-membered rings population decreases rapidly while the four-membered rings population seems to increase. An opening of the intertetrahedral angles, added to a widening of these angles distribution, is also observed for the two different samples. Then, from these spectroscopic features, the annealing induces a relaxation of the structure, with the main band and defect bands evolving towards the fused silica structure. The mechanical losses were found to be correlated with the three-membered rings population, while not driven by this population, which could be explained by the similarities between the activation energies of the mechanisms at stake.

2.4 Conclusion

The structure of IBS-silica has been studied, depending on the deposition parameters and annealing processes, and compared to the mechanical losses.

Ion Beam Sputtered deposition leads to dense and internally stressed silica glass layers, presenting an unusual high population of three-membered rings compared to fused silica.

One way to reduce the coatings stresses is to tune the coater source parameters. By decreasing the intensity of the source, the ring statistics shifts towards larger units with a decrease of the three-membered ring population. However, a contamination of the coatings by Molybdenum atoms, coming from the coater acceleration grids, was highlighted, hindering the results.

Due to the high internal stress of the layers, sputtered silica relaxes easily towards a less dense and less stressed structure, even if the annealing temperature is low compared to the glass transition temperature, and for short times compared to the relaxation times of fused silica. The 3-membered ring population was found to be correlated with the coatings mechanical losses, even for different deposition parameters, which could be explained by the similar activation energies.

To further look for the microstructural origin of the loss, we will pursue the study on the high index material composing the Bragg mirrors : TiO_2 -doped Ta_2O_5 non-crystalline layers, starting by the characterization of Ta_2O_5 .

Bibliography

- [Anderson, 1981] Anderson, A. C. (1981). *Thermal Conductivity*, pages 65–80. Springer Berlin Heidelberg, Berlin, Heidelberg.
- [Barrio et al., 1993] Barrio, R. A., Galeener, F. L., Martínez, E., and Elliott, R. J. (1993). Regular ring dynamics in ax_2 tetrahedral glasses. *Phys. Rev. B*, 48:15672–15689.
- [Buchenau et al., 1992] Buchenau, U., Galperin, Y. M., Gurevich, V. L., Parshin, D. A., Ramos, M. A., and Schober, H. R. (1992). Interaction of soft modes and sound waves in glasses. *Phys. Rev. B*, 46:2798–2808.
- [Buchenau et al., 1984] Buchenau, U., Nücker, N., and Dianoux, A. J. (1984). Neutron scattering study of the low-frequency vibrations in vitreous silica. *Phys. Rev. Lett.*, 53:2316–2319.
- [Burgin et al., 2008] Burgin, J., Guillon, C., Langot, P., Vallée, F., Hehlen, B., and Foret, M. (2008). Vibrational modes and local order in permanently densified silica glasses: Femtosecond and raman spectroscopy study. *Phys. Rev. B*, 78:184203.
- [Damart et al., 2016] Damart, T., Coillet, E., Tanguy, A., and Rodney, D. (2016). Numerical Study of the Structural and Vibrational Properties of Amorphous Ta_2O_5 and TiO_2 -doped Ta_2O_5 . *Journal of Applied Physics*, 119(17):175106.
- [Dávila et al., 2003] Dávila, L. P., Caturla, M.-J., Kubota, A., Sadigh, B., Díaz de la Rubia, T., Shackelford, J. F., Risbud, S. H., and Garofalini, S. H. (2003). Transformations in the medium-range order of fused silica under high pressure. *Phys. Rev. Lett.*, 91:205501.
- [Deschamps, 2009] Deschamps, T. (2009). *Étude des déformations élastique et plastique des verres de silice et silico-sodo-calciques sous hautes-pressions hydrostatiques et indentation par spectrométrie Raman*. PhD thesis, Université Claude Bernard Lyon 1.
- [Duval et al., 1990] Duval, E., Boukenter, A., and Achibat, T. (1990). Vibrational dynamics and the structure of glasses. *Journal of Physics: Condensed Matter*, 2(51):10227.
- [Elliott, 1992] Elliott, S. R. (1992). A unified model for the low-energy vibrational behaviour of amorphous solids. *EPL (Europhysics Letters)*, 19(3):201.

- [Galeener, 1985] Galeener, F. L. (1985). Raman and ESR studies of the thermal history of amorphous SiO₂. *Journal of Non-Crystalline Solids*, 71(1):373 – 386.
- [Galeener and Mikkelsen, 1981] Galeener, F. L. and Mikkelsen, J. C. (1981). Vibrational dynamics in ¹⁸O-substituted vitreous SiO₂. *Physical Review B*.
- [Galperin et al., 1987] Galperin, Y. M., Gurevich, V. L., and Parshin, D. A. (1987). Thermal expansion of glasses at low temperatures: sensitivity to the two-level- system model. *Sov. Phys. JETP*, 65:1257.
- [Gilroy and Phillips, 1981] Gilroy, K. S. and Phillips, W. A. (1981). An asymmetric double-well potential model for structural relaxation processes in amorphous materials. *Philosophical Magazine B*, 43(5):735–746.
- [Granata et al., 2016] Granata, M., Saracco, E., Morgado, N., Cajgfinger, A., Cagnoli, G., Degallaix, J., Dolique, V., Forest, D., Franc, J., Michel, C., et al. (2016). Mechanical loss in state-of-the-art amorphous optical coatings. *Physical Review D*, 93(1):012007.
- [Hamdan et al., 2014] Hamdan, R., Trinastic, J. P., and Cheng, H. P. (2014). Molecular dynamics study of the mechanical loss in amorphous pure and doped silica. *The Journal of Chemical Physics*, 141(5).
- [Hehlen, 2010] Hehlen, B. (2010). Inter-tetrahedra bond angle of permanently densified silicas extracted from their Raman spectra. *Journal of physics. Condensed matter*, 22:025401.
- [Hirose et al., 2006] Hirose, T., Saito, K., and Ikushima, A. J. (2006). Structural relaxation in sputter-deposited silica glass. *Journal of Non-Crystalline Solids*, 352(21–22):2198 – 2203.
- [Jin et al., 1994] Jin, W., Rajiv, K. K., Vashishta, P., and Rino, J. P. (1994). Structural transformation in densified silica glass : A molecular-dynamics study. *Physical Review B*, 50(1):118–131.
- [Johari, 2014] Johari, G. (2014). Calorimetric features of release of plastic deformation induced internal stresses, and approach to equilibrium state on annealing of crystals and glasses. *Thermochimica Acta*, 581:14 – 25.
- [Karpov et al., 1983] Karpov, V. G., Klinger, M. I., and Ignat'ev, F. N. (1983). Theory of the low-temperature anomalies in the thermal properties of amorphous structures. *Sov. Phys. JETP*, 57:439.

- [Knapp et al., 2015] Knapp, M., Lomonosov, A. M., Warkentin, P., Jäger, P. M., Ruile, W., Kirschner, H.-P., Honal, M., Bleyl, I., Mayer, A. P., and Reindl, L. M. (2015). Accurate characterization of SiO₂ thin films using surface acoustic waves. *IEEE transactions on ultrasonics, ferroelectrics, and frequency control*, 62(4):736–43.
- [Martin et al., 1983] Martin, P. J., MacLeod, H. A., Netterfield, R. P., Pacey, C., and Sainty, W. G. (1983). Ion-beam-assisted deposition of thin films. *Applied Optics*, 22(1):178–184.
- [Martinet et al., 2015] Martinet, C., Kassir-Bodon, A., Deschamps, T., Cornet, A., Le Floch, S., Martinez, V., and Champagnon, B. (2015). Permanently densified SiO₂ glasses: a structural approach. *Journal of physics. Condensed matter*, 27(32):325401.
- [McMillan, 1984] McMillan, P. F. (1984). Structural Studies of Silicate Glasses and Melts-Applications and Limitations of Raman Spectroscopy. *American Mineralogist*, 69:622–644.
- [Monaco et al., 2006] Monaco, A., Chumakov, A. I., Monaco, G., Crichton, W. A., Meyer, A., Comez, L., Fioretto, D., Korecki, J., and Ruffer, R. (2006). Effect of densification on the density of vibrational states of glasses. *Phys. Rev. Lett.*, 97:135501.
- [Mulder and Damen, 1987] Mulder, C. and Damen, A. (1987). The origin of the "Defect" 490 cm^{-1} Raman peak in silica gel. *Journal of Non-Crystalline Solids*, 93:387–394.
- [Pasquarello and Car, 1998] Pasquarello, A. and Car, R. (1998). Identification of raman defect lines as signatures of ring structures in vitreous silica. *Phys. Rev. Lett.*, 80:5145–5147.
- [Pauleau, 2001] Pauleau, Y. (2001). Generation and evolution of residual stresses in physical vapour-deposited thin films. *Vacuum*, 61(2):175–181.
- [Payen et al., 1992] Payen, E., Kasztelan, S., and Moffat, J. B. (1992). In situ Laser Raman Study of the Effect of water on undoped and Caesium-doped Silica-supported 12-Molybdophosphoric Acid Catalysts. *J. Chem Soc. Faraday Trans*, 88(15):2263–2267.
- [Penn et al., 2003] Penn, S. D., Sneddon, P. H., Armandula, H., Betzwieser, J. C., Cagnoli, G., Camp, J., Crooks, D. R. M., Fejer, M. M., Gretarsson, A. M., Harry, G. M., Hough, J., Kittelberger, S. E., Mortonson, M. J., Route, R., Rowan, S., and Vassiliou, C. C. (2003). Mechanical loss in tantala/silica dielectric mirror coatings. *Classical and Quantum Gravity*, 20(13):2917.
- [Pohl, 1981] Pohl, R. O. (1981). *Low Temperature Specific Heat of Glasses*, pages 27–52. Springer Berlin Heidelberg, Berlin, Heidelberg.

- [Principe et al., 2015] Principe, M., Pinto, I. M., Pierro, V., DeSalvo, R., Taurasi, I., Villar, A. E., Black, E. D., Libbrecht, K. G., Michel, C., Morgado, N., and Pinard, L. (2015). Material loss angles from direct measurements of broadband thermal noise. *Phys. Rev. D*, 91:022005.
- [Rino et al., 1993] Rino, J. P., Ebbsjö, I., Kalia, R. K., Nakano, A., and Vashishta, P. (1993). Structure of rings in vitreous SiO₂. *Phys. Rev. B*, 47:3053–3062.
- [Sainty et al., 1984] Sainty, W. G., Netterfield, R., and Martin, P. J. (1984). Protective dielectric coatings produced by ion-assisted deposition. *Applied optics*, 23(7):1116–1119.
- [Sato and McMillan, 1987] Sato, R. K. and McMillan, P. F. (1987). An Infrared and Raman Study of the Isotopic Species of α -Quartz. *J. Phys. Chem.*, 91:3494–3498.
- [Sen and Thorpe, 1977] Sen, P. and Thorpe, M. (1977). Phonons in AX₂ glasses: From molecular to band-like modes. *Physical Review B*, 15(8):4030.
- [Shcheblanov et al., 2015] Shcheblanov, N. S., Mantsi, B., Umari, P., and Tanguy, A. (2015). Detailed analysis of plastic shear in the raman spectra of sio 2 glass. *Journal of Non-Crystalline Solids*, 428:6–19.
- [Shimodaira et al., 2006] Shimodaira, N., Saito, K., Sekiya, E., and Ikushima, A. (2006). Microscopic structural changes of SiO₂ glasses as a function of temperature investigated by in situ Raman spectroscopy. *Physical Review B*, 73(21):214206.
- [Terki et al., 1999] Terki, F., Pilliez, J.-N., Woignier, T., Pelous, J., Fontana, A., Rossi, F., Montagna, M., Ferrari, M., Cicognani, G., and Dianoux, A. (1999). Low-frequency light scattering in silica xerogels: influence of the heat treatment. *Philosophical Magazine B*, 79(11-12):2081–2089.
- [Thielemann and Hess, 2013] Thielemann, J. P. and Hess, C. (2013). Monitoring Silica Supported Molybdenum Oxide Catalysts at Work : A Raman Spectroscopic Study. *Chem Phys Chem*, 14:441–447.
- [Thielemann et al., 2011] Thielemann, J. P., Ressler, T., Walter, A., Tzolova-müller, G., and Hess, C. (2011). Applied Catalysis A : General Structure of molybdenum oxide supported on silica SBA-15 studied by Raman, UV-Vis and X-ray absorption spectroscopy. *Applied Catalysis A, General*, 399(1-2):28–34.
- [Topp and Cahill, 1996] Topp, K. A. and Cahill, D. G. (1996). Elastic properties of several amorphous solids and disordered crystals below 100 K. *Zeitschrift für Physik B*, 101:235–245.

- [Verbruggen et al., 1994] Verbruggen, N. F. D., Mestl, G., von Hippel, L. M. J., Lengeler, B., and Knoezinger, H. (1994). Structure of k-doped molybdena-on-alumina catalysts as studied by x-ray absorption and raman spectroscopy. *Langmuir*, 10(9):3063–3072.
- [Weigel et al., 2016] Weigel, C., Foret, M., Hehlen, B., Kint, M., Cl, S., Polian, A., Vacher, R., and Ruffl, B. (2016). Polarized Raman spectroscopy of $v\text{-SiO}_2$ under rare-gas compression. *Physical Review B*, 93:224303.
- [Weiss et al., 1996] Weiss, G., Daum, A., Sohn, M., and Arndt, J. (1996). Vibrating reed experiments on compacted vitreous silica. *Physica B: Condensed Matter*, 219:290–292.
- [Zarzycki, 1982] Zarzycki, J. (1982). *Les verres et l'état vitreux*. Masson.
- [Zeller and Pohl, 1971] Zeller, R. C. and Pohl, R. O. (1971). Thermal conductivity and specific heat of noncrystalline solids. *Phys. Rev. B*, 4:2029–2041.
- [Zhang et al., 2015] Zhang, C.-c., Zhang, L.-j., Liao, W., and Yan, Z.-h. (2015). ATR-FTIR spectroscopic studies on density changes of fused silica induced by localized CO_2 laser treatment. *Chinese Physics B*, 24(2):024220.

Chapter 3

Tantalum pentoxide

The high index material used in the Bragg mirrors of the LIGO and VIRGO Gravitational Waves Detectors is composed of TiO_2 -doped Ta_2O_5 . This mixed oxide was chosen along silica for its high refractive index at 1064 nm, and because low mechanical and optical loss are exhibited by the layers, as required by the detectors specifications.

Tantalum oxides, outside the GWD domain, are also used in electronics due to interesting electric and dielectric properties [Lin et al., 1999]. For example, they present excellent optical properties and produce strong glass when mixed with alumina [Rosales-Sosa et al., 2015], and are also used as coatings resistant to corrosion [Zhou et al., 2005].

The structure of this non-crystalline oxide remains unclear, molecular simulations being developed in systems small compared to the typical length scale of this material, and with very high quenching rates (10^{13} K s^{-1}) [Bassiri et al., 2013].

Recent studies showed that a TiO_2 -doping between 15-25% of the Tantalum pentoxide layers reduces the loss by 20-40% [Harry et al., 2007]. Yet the origin of this mechanisms remains obscure, despite recent work showing that they could originate at medium range order [Trinastic et al., 2016].

In this Chapter, the Tantalum pentoxide structure will be explored, with a parallel study to the one conducted on silica. Indeed, the effect of annealing will be investigated. Moreover, to push further the characterization of this complex structure, a high pressure study was conducted on crystalline and non-crystalline layers. Finally, we will come back closer to the structure of the mirrors coatings, by studying the effect of the TiO_2 -doping.

3.1 Crystalline and amorphous structure

Crystalline structure

Different polymorphs of crystalline Tantalum pentoxide are presented in the literature, corresponding to low-temperature (L- Ta_2O_5) and high-temperature phases (H- Ta_2O_5),

with different polymorphs in each phase [Wu et al., 2011, Balachandran and Eror, 1982, Terao, 1967]. At ambient pressure, the L-Ta₂O₅ polymorph undergoes a phase transformation to a H-Ta₂O₅ around 1300 °C [Balachandran and Eror, 1982, Terao, 1967] with different possible structural variations (monoclinic, orthorhombic or tetragonal cells).

The most commonly observed and studied crystalline structure is the low temperature polymorph β -Ta₂O₅. Other low temperature polymorphs exist, such as the δ -Ta₂O₅ which presents a tetragonal structure, or γ -Ta₂O₅ with a centered-face cubic structure. Every crystalline sample studied in this work presents a β -Ta₂O₅ structure as compared with [Balachandran and Eror, 1982], we will then focus on this polymorph. The crystalline structure of the β polymorph is not uniquely determined, even though the major part of the studies agree on an orthorhombic structure [Sahu and Kleinman, 2004, Terao, 1967, Dobal et al., 2000, Aleshina and Loginova, 2002]. The difficulty of defining the crystalline structure of this oxide is mainly due to the important size of the unit cells, presenting no simple symmetry.

A common consensus describes the structure as a chain of corner and edge-sharing distorted TaO₆ octahedra and TaO₇ pentagonal bipyramids [Balachandran and Eror, 1982, Lü et al., 2013, Guo and Robertson, 2015, Joseph et al., 2012]. First-neighbor interatomic distances are around 1.95 Å for Ta-O bonds, and between 3.5 Å and 4 Å for Ta-Ta bonds [Sahu and Kleinman, 2004]. In the unit cell, if we consider the one presented by [Lü et al., 2013], polyhedra are connected by one oxygen along the *b*-axis, and by one or two oxygens (corner or edge) along the *a* and *c* axis (figure 3.1). The density of β -Ta₂O₅ is close to 8.39 g cm⁻³ with a Young's modulus around 180 GPa [Wu et al., 2011].

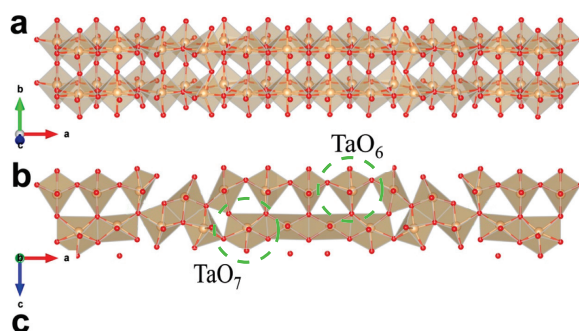


Figure 3.1 – One possible schematic view of the β -Ta₂O₅ unit cell [Lü et al., 2013], view along *c* axis (up) and *b* axis (down). The unit cell presents edge- and corner-shared TaO₆ and TaO₇ units.

Amorphous structure

The tantalum pentoxide processed at the LMA, and studied here, consists of thin non-crystalline films about 3 μm thick. The structure of the amorphous tantalum pentoxide (a-Ta₂O₅), represented on figure 3.2, is close to the crystal, and only small modifications in the amorphous structure allow to reach a crystalline one. Indeed, in a-Ta₂O₅ as described by [Damart et al., 2016, Bassiri et al., 2016, Guo and Robertson, 2015], the first-neighbor atoms of each tantalum are oxygen atoms, forming a chain-like structure of polyhedra similar to the crystalline structure. Table 3.1 presents the coordination numbers for the Tantalum and Oxygen atoms. Around 70 % of the tantalum atoms are surrounded by six oxygen atoms, forming Ta-centered octahedra, and around 30 % are surrounded by five oxygen atoms, forming bipyramids. The proportion of TaO₇ is much smaller compared to the crystalline structure, and two new kind of oxygen cages exist in the amorphous one : TaO₄ and TaO₅.

Tantalum	%	Oxygen	%
Coord. 4	0.5	Coord. 2	69.9
Coord. 5	28.5	Coord. 3	30.1
Coord. 6	69.4		
Coord. 7	1.6		

Table 3.1 – Average coordination numbers in amorphous Ta₂O₅ for the first-neighbor Ta-O bonds (from Damart 2016 [Damart et al., 2016]).

Most of these polyhedra are linked by vertex, but they can also be linked together by edge or face as required by stoichiometry. Links by an edge or a face between polyhedra correspond to the 2 or 3 oxygen atoms shared by 2 tantalum atoms.

These structural arrangements do not follow the rules from [Zachariasen, 1932]. Indeed, there are too many oxygen atoms around the Tantalum and they can be linked to more than two cations. Moreover, the different polyhedra can be linked by edges or faces, which does not correspond to the definition of a glass. We can then conclude that the non-crystalline form of Tantalum pentoxide is an amorphous solid and not a glass.

The inner structure of the polyhedra is quite ordered with $\widehat{\text{O-Ta-O}}$ angles centered on 90° and 180°. The connectivity is however less ordered, with a broad distribution of $\widehat{\text{Ta-O-Ta}}$ angles. A peak at 105° can be linked to the oxygen atoms having three tantalum neighbors, and the distribution between 120° and 180° is correlated with the oxygen linked to two tantalum atoms.

The inter-atomic bonds are similar to the ones of the crystalline structure. Damart et al. simulated these bond lengths, which are around 1.92 Å for the Ta-O bonds, 3.76 Å for the Ta-Ta bonds and 2.76 Å for the O-O bonds [Damart et al., 2016], similar to ex-

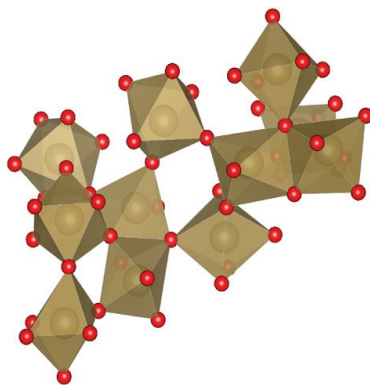


Figure 3.2 – Schematic view of the amorphous structure of tantalum pentoxide from Damart 2016 [Damart et al., 2016]. The network structure of the amorphous is mostly composed by TaO_6 polyhedra (Ta atoms in brown, O atoms in red) linked either by vertex, edge or face.

perimental values [Bassiri et al., 2015].

To our knowledge, no bulk amorphous samples were synthesized yet. The tantalum pentoxide thin films studied here have a density close to $7.6 \pm 0.1 \text{ g cm}^{-3}$. The experimental Young's modulus of the studied thin films was measured around 110 GPa via the mechanical losses measurements at the LMA. Simulation indicated a Young's modulus of 140 GPa [Damart et al., 2016], closer to the experimental values on films deposited by magnetron sputtering around $140 \pm 15 \text{ GPa}$ [Alcalá et al., 2002].

Raman spectra

As for the silica study, the main tool used to probe the structure of the Tantalum oxide layers was Raman spectroscopy. This analysis method gives insight on the vibrational modes of the short and medium range order structure. One way to understand the link between the structure and Raman signatures is to explore the vibrational density of states (vdos) via simulations. The difference between the two spectra comes from the fact that the VDOS covers all possible vibration modes in the structure, while selection rules apply in Raman scattering.

The vibrational density of states of amorphous Tantalum pentoxide was simulated by [Damart et al., 2016], and is compared on figure 3.3 to the experimental Raman spectrum of crystalline and amorphous Tantalum Pentoxide. The amorphous spectrum being very similar to the VDOS, most of the vibrational modes seem to be active in Raman spectroscopy for this material. Inactive modes in Raman may be located around 170 cm^{-1} , between 300 and 500 cm^{-1} and in the shoulder above 800 cm^{-1} .

The crystalline spectrum is also quite similar to the amorphous one. This is mainly due to the similarities between the two structures, and the complexity of the crystalline

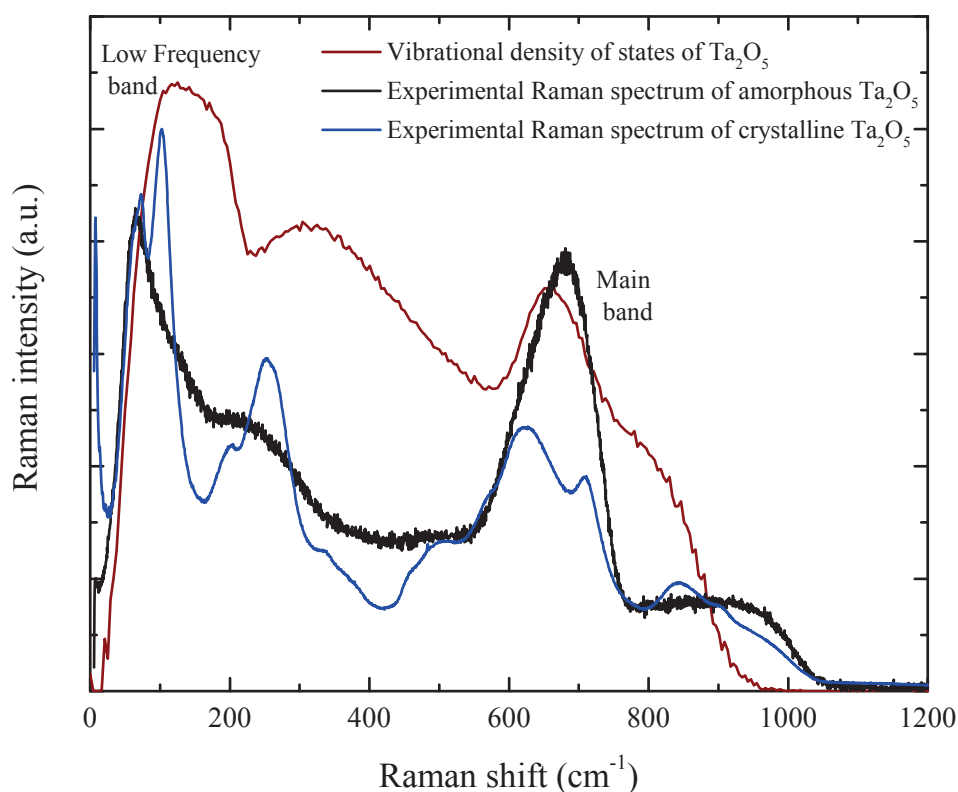


Figure 3.3 – Simulated vibrational density of states by molecular dynamics [Damart et al., 2016], compared to the Raman spectra of Amorphous Ta_2O_5 and crystalline Ta_2O_5 .

cells. The crystalline spectrum presents only slightly thinner signatures compared to the amorphous one, with overlaid large bands. This spectrum was compared to those of other crystalline samples found in the literature and correspond to $\beta\text{-Ta}_2\text{O}_5$ [Joseph et al., 2012, Balachandran and Eror, 1982]. From the Raman spectra, every crystalline sample studied in this work is $\beta\text{-Ta}_2\text{O}_5$.

The vibrational density of states can be decomposed in different vibrational modes, coming from the various atoms and structures present in the sample. The partial vibrational density of states can be seen on figure 3.4, with the partial VDOS of the oxygen atoms decomposed into rocking, stretching and bending of the O-2Ta and O-3Ta bonds (as shown on figure 3.5). The Raman band attribution found in the literature, for crystalline and amorphous tantalum pentoxide, describes possible attribution for large areas without defining exactly each Raman peak [Balachandran and Eror, 1982, Joseph et al., 2012, Dobal et al., 2000, Ono et al., 2001, Tsuchiya et al., 2011]. These attributions

are correlated with the decomposed VDOS from [Damart et al., 2016], and the vague attribution is consistent with the overlapping bands of each vibrational mode.

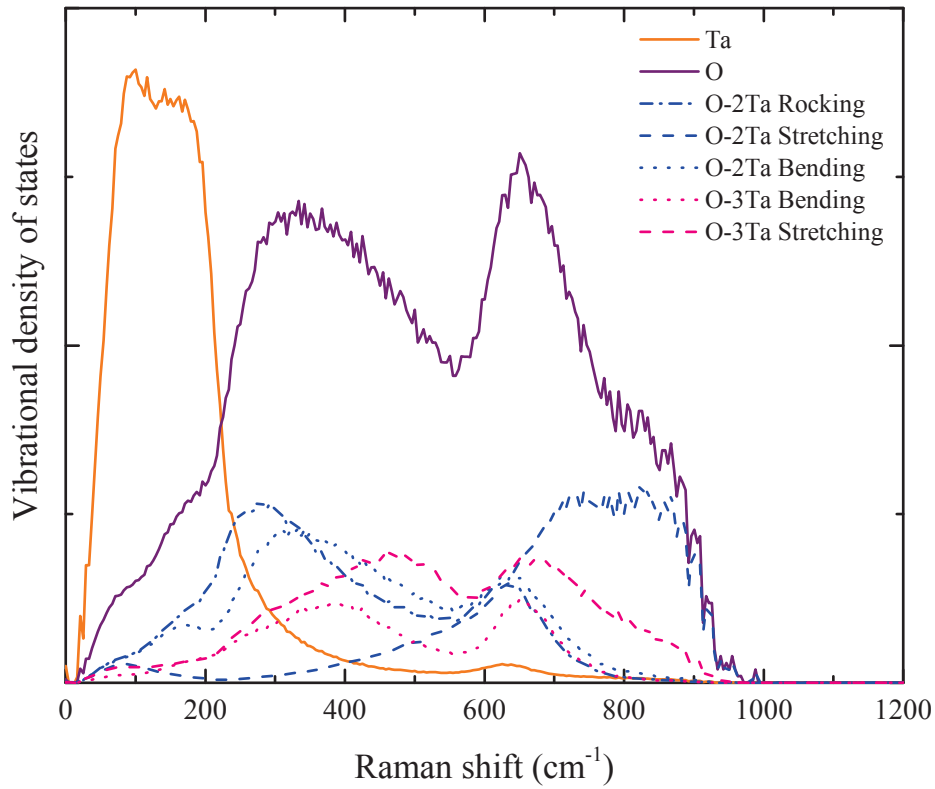


Figure 3.4 – Partial vibrational density of states in Ta_2O_5 with the decomposition into the rocking, bending and stretching modes of O-2Ta and O-3Ta bonds [Damart et al., 2016].

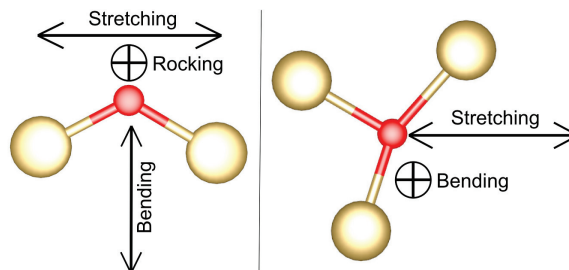


Figure 3.5 – O-2Ta and O-3Ta bonds with the vectors defining rocking, bending and stretching vibration modes [Damart et al., 2016].

The band attribution used in this work and found via the VDOS comparison with

literature is resumed on table 3.2. The attribution will be the same for crystalline and amorphous structure, considering the imprecise band attribution and the resemblance between the spectra and the structures. For the amorphous spectrum, the low frequency band, between 50 cm^{-1} and 150 cm^{-1} , may also be coupled with the Boson peak, which is a characteristic of all non-crystalline samples and which should appear in the same frequency range. However, due to the presence of a low frequency band also in the crystalline spectrum, the differentiation of the Tantalum and Boson signatures is complex. A more specific band attribution will be necessary in the future to discriminate the origin of the multiple peaks in the crystalline spectra, in order to get a better understanding of the experimental results.

Above 200 cm^{-1} , vibrations come from the oxygen atoms' displacement. Apart from the shoulder above 770 cm^{-1} which seems to be dominated by the O-2Ta stretching, other bands are a convolution of rocking, bending and stretching of the O-2Ta and O-3Ta units. The large band centered at 680 cm^{-1} will be called "main band" (MB) in this thesis.

Crystalline bands	Amorphous bands	Band attribution
70 cm^{-1} 100 cm^{-1}	70 cm^{-1}	Tantalum atoms vibrations in their oxygen cage Maybe a Boson peak underlying the amorphous band
205 cm^{-1} 250 cm^{-1}	$200\text{-}300\text{ cm}^{-1}$	Mainly bending of Ta-O-Ta bonds added to O-3Ta stretching
510 cm^{-1} 620 cm^{-1} 705 cm^{-1}	680 cm^{-1}	Vibrations from the oxygen atoms' displacement (rocking, bending and stretching modes of O-3Ta and O-2Ta)
845 cm^{-1} $800\text{-}1000\text{ cm}^{-1}$	$800\text{-}1000\text{ cm}^{-1}$	Mainly O-2Ta stretching

Table 3.2 – Band attribution for the Raman spectrum of Ta_2O_5 [Damart et al., 2016, Balachandran and Eror, 1982, Joseph et al., 2012, Dobal et al., 2000, Ono et al., 2001, Tsuchiya et al., 2011].

3.2 Annealing

As we have seen in Chapter 2.3.1, the mirrors are annealed during 10 hours at $T_a = 500^\circ\text{C}$ after the deposition, in order to improve the optical properties and lower the mechanical losses. In silica glass (Chapter 2.3), the annealing induces a stress release and a structural relaxation linked to the decrease of the mechanical losses. The same study was conducted on tantalum pentoxide in order to find a possible link between the evolution of the structure and the mechanical losses, evolution depending on the annealing time and on the annealing temperature.

3.2.1 Evolution with annealing time

A $3\ \mu\text{m}$ thick layer of pure amorphous Tantalum oxide was annealed at $T_a = 500^\circ\text{C}$ during 10 to 50 h. During the first ten hours of annealing, the coating losses decrease from $11.9 \pm 0.4 \times 10^{-4}$ rad to $4.69 \pm 0.33 \times 10^{-4}$ rad (figure 3.7), corresponding to a 60 % decrease of the losses, lower than the 80 % decrease in the case of IBS-silica (see 2.3.1). After 10 hours, no more evolution of the mechanical losses can be measured. To investigate if the annealing has an effect on the structure, $3\ \mu\text{m}$ samples of amorphous tantalum pentoxide were annealed up to 50 hours and analyzed by Raman spectroscopy. The Tantalum pentoxide layers studied here are deposited on fused silica, with no metallic Tantalum layer in between the coating and the substrate. Consequently, the signal of the fused silica substrate appears on the spectra, with the presence of a band around $490\ \text{cm}^{-1}$.

Figure 3.6 presents the Raman spectra of the non annealed sample compared to samples annealed during 10h, 20h and 50h at $T_a = 500^\circ\text{C}$. As all the annealed Raman spectra are superposed to each other, the only visible structural effect happens during the first few hours of annealing. This absence of evolution in the structure after a 10 hour annealing is similar to the stability of the mechanical losses.

During the first hours of annealing, the relative area of the low frequency band increases from $17.2 \pm 0.2\%$ to $19.0 \pm 0.2\%$, while its position stays the same within the spectrometer's resolution. The area of the main band is also slightly increasing (figure 3.7), from $13.4 \pm 0.1\%$ to $14.4 \pm 0.1\%$ with the position staying also the same. The measured areas are drawn on figure 3.6 and divided by the total area (more details in appendix). The evolution of these area follows the mechanical losses, as nothing evolves after the first 10 hours of annealing.

Contrary to silica layers, annealing does not induce ample structural changes. With a density around $7.6 \pm 0.1\ \text{g cm}^{-3}$ before annealing, the tantalum pentoxide structure is much compact than silica, which could lead to smaller changes with annealing. The annealing temperature is quite low compared to the melting temperature of this ox-

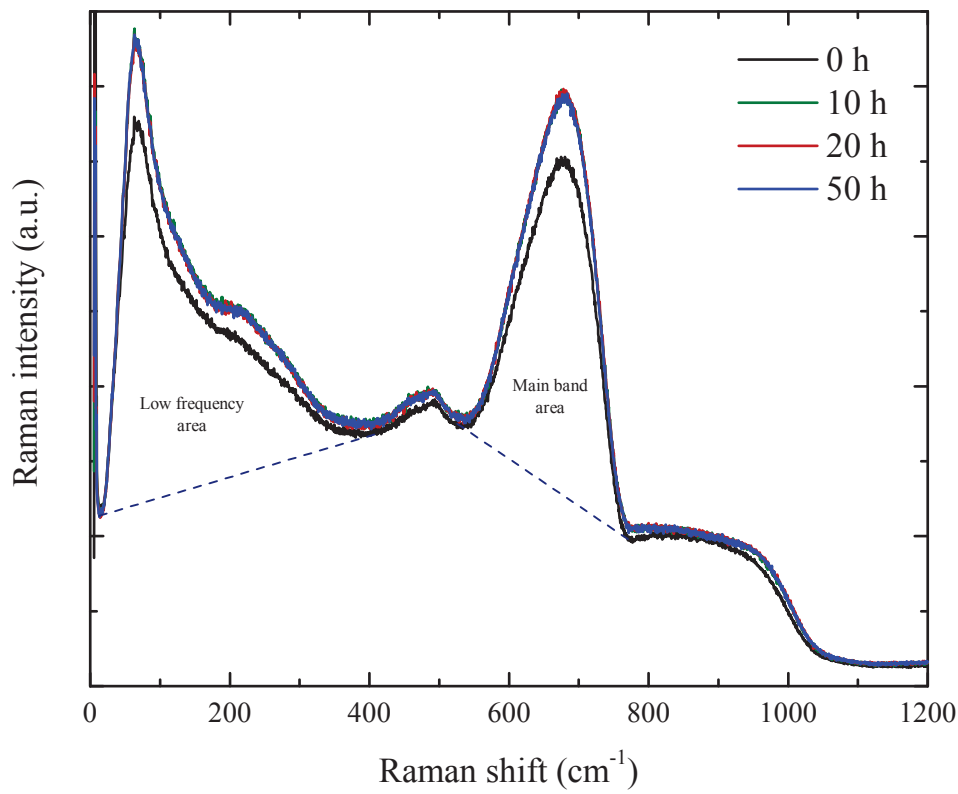


Figure 3.6 – Raman spectra of annealed Ta_2O_5 layers during 0 hours (black), 10 hours (green), 20 hours (red), and 50 hours (blue) at $T_a = 500^\circ\text{C}$. The 10h, 20h and 50h annealing are superposed on top of each other, normalized by the total area.

ide ($T_{\text{fus}}(\text{Ta}_2\text{O}_5) = 1860^\circ\text{C}$ [Balachandran and Eror, 1982], higher than $T_{\text{fus}}(\text{SiO}_2) = 1723^\circ\text{C}$), which could explain the small changes seen on the Raman spectra. The slight evolution of the spectra could come from a stress release, the temperature being too low to induce structural changes in this amorphous oxide. However, no annealing can be done at higher temperature to increase the possibility of structural changes as crystallization happens.

Contrary to the annealing of silica layers, the evolution of the Ta_2O_5 coatings structure is not clear, but still correlated with the evolution of the coating losses. Indeed, for the mechanical losses and the Raman relative intensity, there is an evolution during the first hours of annealing, and nothing happens after 10 hours. However, in the case of tantalum pentoxide, no precise structural change can explain the origin of the coating losses in amorphous tantalum pentoxide.

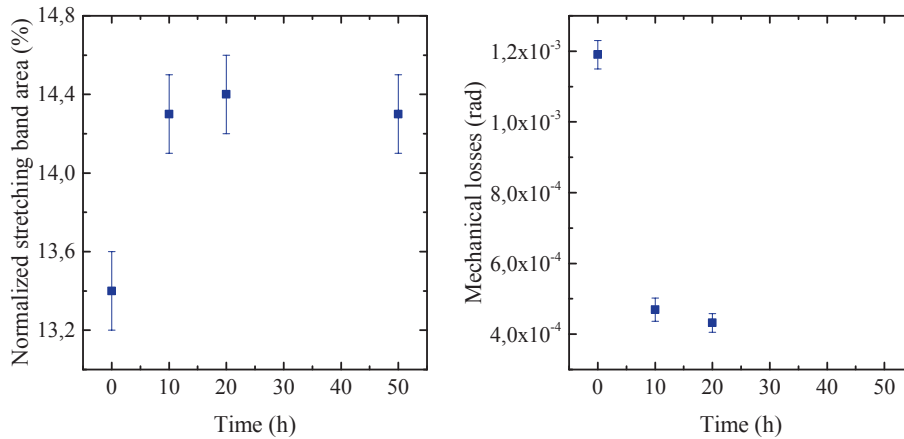


Figure 3.7 – Evolution of the stretching band area (left) and of the mechanical losses (right) compared to the annealing time ($T_a = 500\text{ °C}$).

3.2.2 Evolution with temperature of annealing

The usual annealing temperature is $T_a = 500\text{ °C}$, inducing no visible structural relaxation in Ta_2O_5 thin films. In order to see if the temperature has a strong effect, annealing at different temperatures between 400 °C and 700 °C were conducted on the same layers.

Figure 3.8 presents the Raman spectra of the samples annealed during 10 hours at different temperatures. There are no notable differences between the different spectra from 400 °C to 600 °C , either in position or relative area, and for all spectroscopic features. For a temperature higher than 600 °C , the spectra show significant differences. New bands appear with annealing and other shift to evolve towards a crystalline spectrum. As shown by the Raman spectra, the samples annealed at $T_a = 650\text{ °C}$ and $T_a = 700\text{ °C}$ are partially crystallized into a β low temperature phase, as expected from [Zhu et al., 2005, Joseph et al., 2012]. Non-crystalline Ta_2O_5 being an amorphous oxide, the sudden transition between a disordered structure and a crystalline one is coherent with the absence of a glass transition phenomenon.

As displayed by these spectra, no structural changes with annealing below the crystallization temperature were highlighted at the distances probed by Raman spectroscopy. This could come from the low annealing temperature compared to the melting temperature ($T_a = 500\text{ °C} \ll T_{fus} = 1872\text{ °C}$), inducing only small effects.

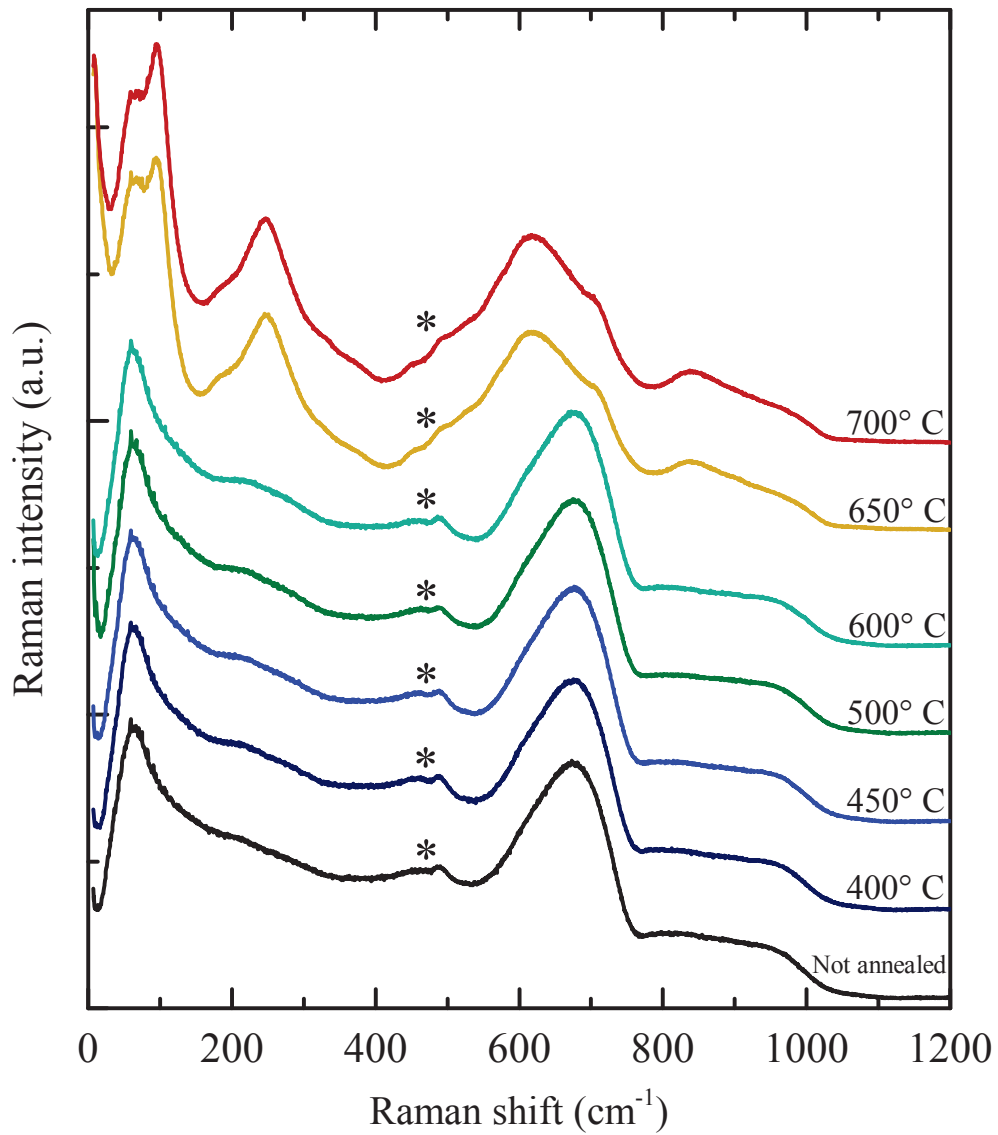


Figure 3.8 – Raman spectra of Ta₂O₅ annealed between 400 °C and 700 °C during 10 hours compared to the spectrum of a not annealed sample. The asterisks show the position of the silica substrate signature.

3.3 Reference Ta₂O₅

The analysis on silica was based on the comparison with fused silica glass. For Ta₂O₅ however, no bulk amorphous sample has ever been synthesized. To understand how the amorphous tantalum pentoxide could evolve with different external parameters, bulk samples were needed and different fabrication processes tested.

3.3.1 Fused Ta₂O₅

Mathieu Allix (CEMHTI, Orléans) tried to process fused amorphous tantalum pentoxide with an aerodynamic levitation device associated with a CO₂ laser heating [Landron et al., 2000, Winborne et al., 1976]. Two marbles were processed during the test, however the quenching rate, 300 K s⁻¹ seems to be too low to get a glass.

Figure 3.9 shows the surface of the tantalum pentoxide marbles. The surface presents some kind of microscopic structures which could be due to crystalline arrangements.

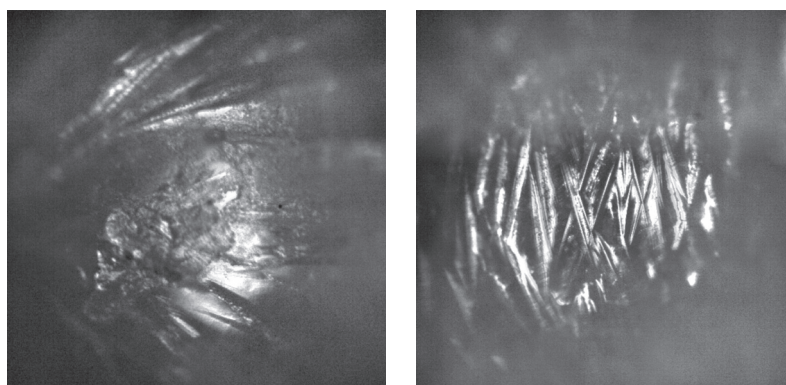


Figure 3.9 – Surfaces of the two processed tantalum pentoxide marbles. Both photos are 1000 μm * 1000 μm in size.

Raman spectra of different spots on the smallest marble are presented on figure 3.10, with the spectra of the reference crystalline powder and of amorphous tantalum pentoxide for comparison. No marble spectrum corresponds totally to the crystalline or amorphous reference spectra, however the different probed spots are closer to the crystalline spectra than to the amorphous one. Indeed, the spectra of the spots 1 and 2 present the characteristic double band of crystalline samples for the low frequency band and the main band. The third spot presented here exhibits four bands between 400 cm⁻¹ and 800 cm⁻¹, revealing a structure close to a crystalline one.

The try to process a fused amorphous sample of tantalum pentoxide leads to the formation of non-homogeneous crystalline marbles. However, a bulk amorphous sample being needed to

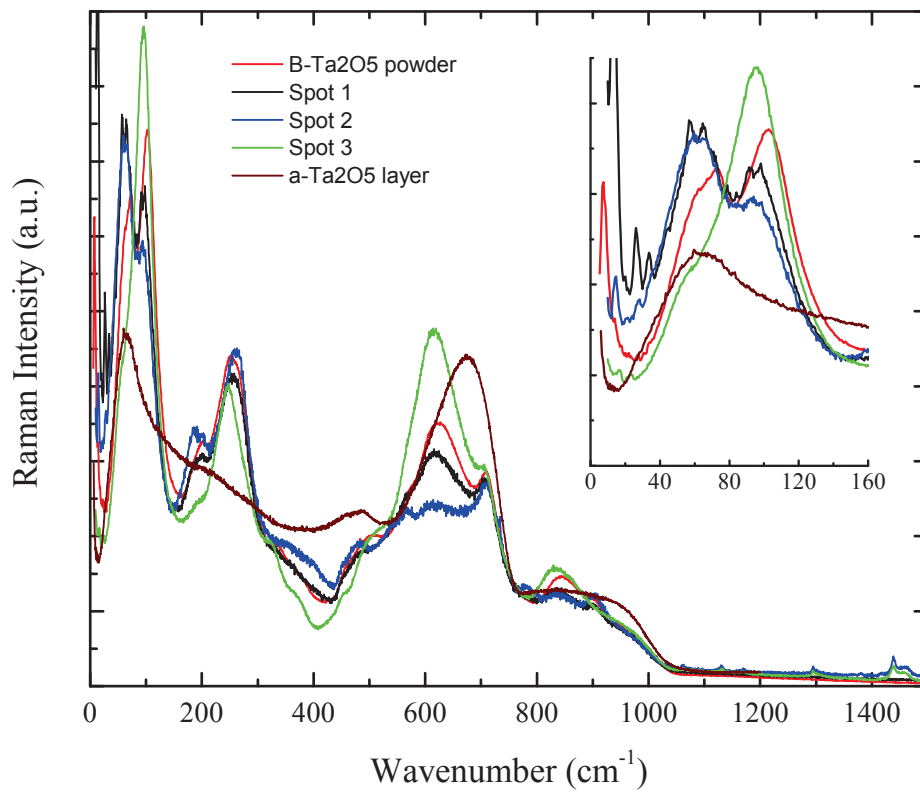


Figure 3.10 – Raman spectra of different spots (spot 1 to 3) on a Ta₂O₅ marble compared to crystalline β -Ta₂O₅ and amorphous Ta₂O₅.

complete our knowledge on this material, processing methods other than melt and quench will be considered.

3.3.2 Thick Ion Beam Sputtered sample

As a reference sample is needed to achieve additional experiments on amorphous Ta₂O₅, a 15 μ m thick layer was processed at the LMA with a Dual Ion Beam Sputtering coater. The coating was deposited on a silicon substrate and, using an etching technique, the substrate has been removed in order to get a free-standing layer. This method allowed experiments that needed micro-metric sized samples. Due to manufacturing constraints for a layer that thick, the sample presents some differences with the usual amorphous Ta₂O₅ thin films. Indeed, to process a 15 μ m layer, a week of deposition process would be needed. To lower the experimental time, the substrate is drawn closer to the target. However in this case the oxygen flux in the deposition chamber was not optimized

inducing under stoichiometry in oxygen.

Photos on figure 3.11 show the sample before and after a 25 hour annealing at $T_a = 600\text{ }^\circ\text{C}$. The as-deposited sample (left) presents an opaque red color due to the oxygen deficiency. After annealing, the sample looks like the usual studied Ta_2O_5 layers, being colorless and transparent. Both photos also have a reddish coloration due to the camera, and the annealed sample does not seem colorless on the photo, as we see for the crucible and its scratches through the a- Ta_2O_5 .

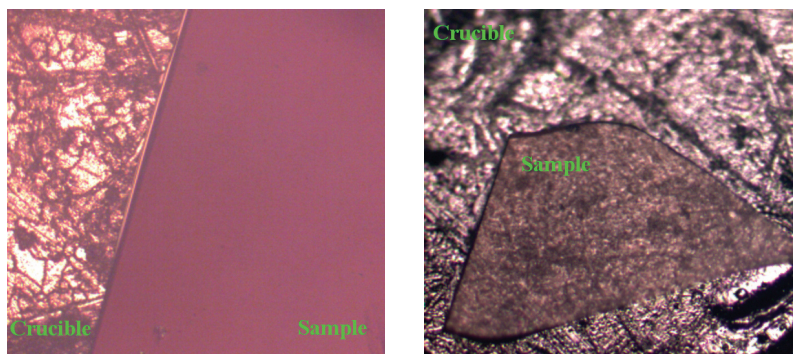


Figure 3.11 – Photos of the $15\text{ }\mu\text{m}$ Ta_2O_5 layer, as deposited (left) and after 25 hours of annealing at $T_a = 600\text{ }^\circ\text{C}$ (right).

The as-deposited Raman spectrum of the sample can be observed in black on figure 3.12. The initial structure is quite different from the amorphous Ta_2O_5 layer studied in Chapter 3.1. The low frequency band and the main band are present and at the same position than the one on figure 3.3. The band around 220 cm^{-1} is similar to the one found in crystalline samples, but cannot be seen in stoichiometric amorphous samples. The shoulder of the main band is replaced by a new band around 810 cm^{-1} . This Raman spectrum was compared to the spectra presented in [Tsuchiya et al., 2011], studying the evolution of the structure with different oxygen contents in amorphous tantalum pentoxide. With this comparison, the composition of the amorphous TaO_x thin film studied here is found to be similar to $\text{TaO}_{2.2}$, lower than the stoichiometric $\text{TaO}_{2.5}$ value. The non stoichiometric structure induces more polyhedra linked by edges or faces, and the presence of double bonds or dangling bonds [Tsuchiya et al., 2011].

In order to have the right stoichiometry and a structure similar to the previously studied thin layers of amorphous Ta_2O_5 , the sample was annealed at $T_a = 600\text{ }^\circ\text{C}$ under normal atmosphere.

Figure 3.12 presents the evolution of Raman spectra during the annealing up to 94 hours. After only 20h hours of annealing, the bands at 220 cm^{-1} and 810 cm^{-1} disappeared, and the Raman spectrum exhibits the same structure than amorphous Ta_2O_5 samples deposited in standard conditions. Following the annealing, the structure begins to reorganize itself between 44h and 53h. The band at 220 cm^{-1} , which was present be-

fore annealing and disappeared quickly, reappears. The low frequency band separates in two bands and the main band shifts towards lower frequencies. These signatures indicate a transformation towards a crystalline structure, which is still not completed after 94h of annealing.

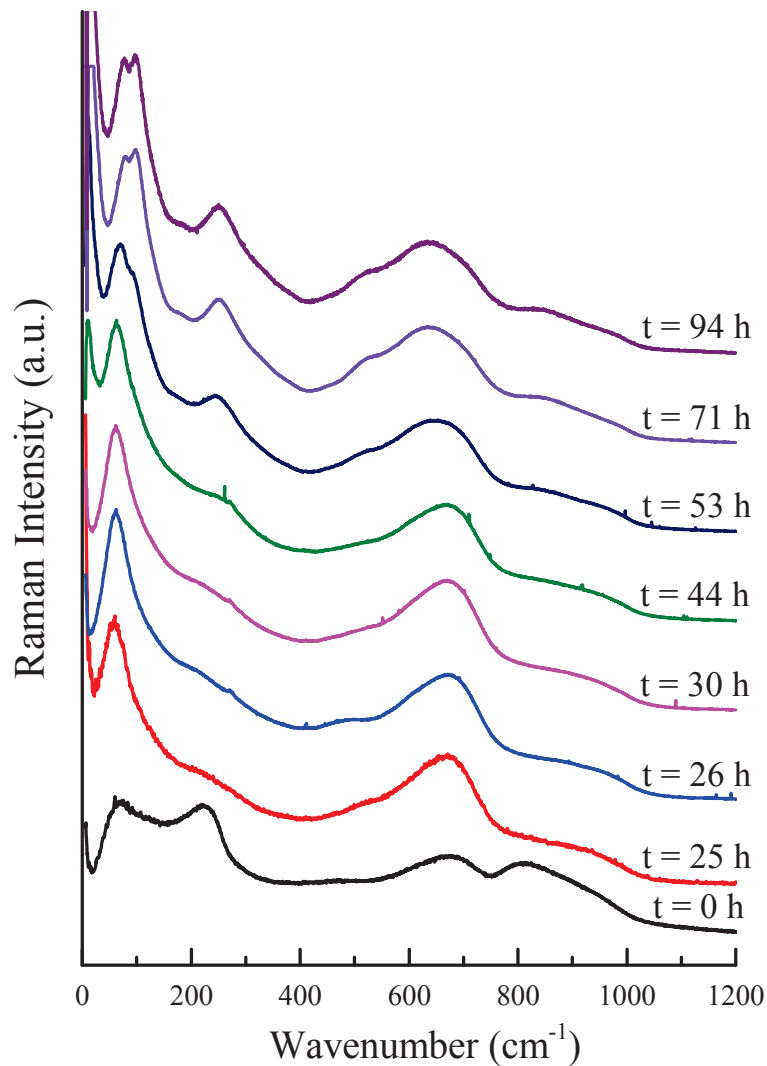


Figure 3.12 – Raman spectra of a 15 μm sample as-deposited and annealed at $T_a = 600$ °C up to 94 hours.

A 15 μm sample was processed with no substrate, in order to allow different experiments to be conducted. The as-deposited sample presents a non stoichiometric composition around TaO_{2.20}. The 15 μm samples used in the remaining work will be annealed 25 hours to reach stoichiometry and considered to have the same structure than 3 μm thick samples on substrates.

3.4 High pressure study

To get more information on how the Ta_2O_5 structure could evolve, we already applied controlled modifications on the sample via studies through different annealing time and temperature, and through the study with a modified stoichiometry. In Chapter 2.1.2, the structure of IBS- SiO_2 structure was found to be close to a densified fused SiO_2 structure, which gave insight on the silica coatings structure. Then, to complete our structural analysis of the tantalum pentoxide, high pressure measurements were conducted on Ta_2O_5 , in order to get some indications on the possible evolution of the structure with this controlled modification of the environment.

By applying pressure on a material, we could expect the positions of the spectroscopic signatures to shift smoothly. In most glasses the structure undergoes important modification, e.g. SiO_2 [Deschamps, 2009], GeO_2 [Durben and Wolf, 1991], LBG [Coussa-Simon et al., 2010]. For silica glass, the evolution of the main spectroscopic signatures present an anomaly at low pressure. Indeed, for example from Brillouin measurements, below 2.5 GPa, the more you apply pressure on the glass, the easier it gets to compress [Sonneville et al., 2012]. Also, beyond 9 GPa, the structure gets permanently modified [Rouxel et al., 2008, Deschamps et al., 2013]. To compare the evolution of Ta_2O_5 under an isotropic high pressure and probe the densification ability of this material, the results of Raman and Brillouin spectroscopic measurements on amorphous and crystalline Ta_2O_5 will be presented. The effect of high pressure on other kinds of glasses will then be described and compared to amorphous Ta_2O_5 for discussion.

The sample used during the high pressure experiments is the 15 μm thick amorphous Ta_2O_5 sample (see Section 3.3.2), annealed 25 hours at $T_a = 600^\circ\text{C}$ to get stoichiometry. Concerning the crystalline results, a NEYCO powder with a 99.99 % purity powder (TA2O54N3-6MM) was analyzed.

3.4.1 Structural evolution by Raman and Brillouin spectroscopy

In situ Raman spectra of amorphous Ta_2O_5 during a compression and decompression cycle up to 13.2 GPa are presented on Figure 3.13.

Under compression, the material undergoes a structural deformation. If the deformation is elastic, the sample structure before and after a compression / decompression cycle should be identical. The elastic limit corresponds to the pressure point beyond which the deformation is permanent, after the release of the mechanical stress. Spectra at ambient pressure before and after the compression / decompression cycles are different, indicating irreversible changes in the structure, and a crossover of the elastic limit. To estimate the elastic limit, the ex-situ Raman spectra before and after the application of different maximum pressure are compared. From experiments on our sample, the

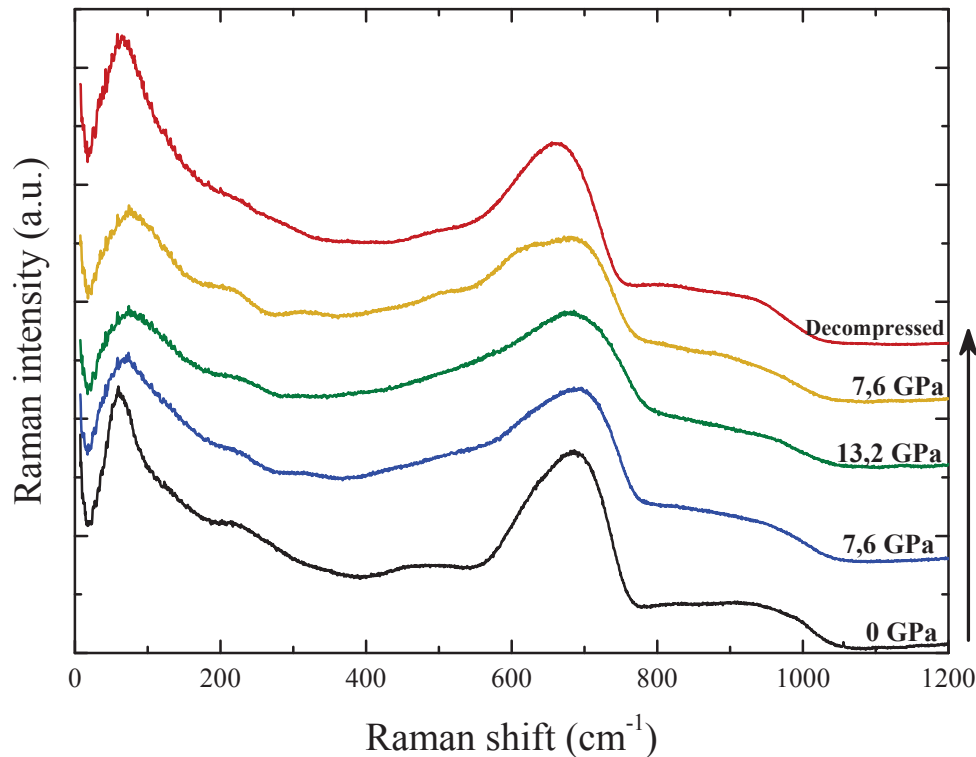


Figure 3.13 – In situ Raman spectra of amorphous Ta_2O_5 during compression up to 13.2 GPa and decompression.

elastic limit was estimated between 4 GPa and 7 GPa. This limit is lower than for silica glass, in which the elastic limit is around 9 GPa [Deschamps et al., 2013].

During compression, a broadening of the low frequency band, added to a shift towards higher frequencies, occurs. The main band also broadens and shifts towards higher frequencies during the compression phase. The shoulder of the main band gets bigger during the compression phase, decreasing again during decompression without reaching its initial form after the cycle.

Figure 3.14 shows the evolution of the low frequency band with pressure, interpreted in terms of Ta atoms vibrations in their oxygen cages, with a possible Boson peak hidden below. The stability of this band around 62 cm^{-1} during compression below 5 GPa could be explained by the pressure too low to deform the polyhedra as the space between polyhedra is more easily compressed than polyhedra themselves [Li et al., 2014]. For a compression higher than 5 GPa, the band is shifting towards higher frequencies from $62 \pm 3 \text{ cm}^{-1}$ to $77 \pm 3 \text{ cm}^{-1}$ at the highest pressure reached (13.2 GPa). As the pressure further increases, Ta-O bonds shortens, inducing a Raman shift increase [Lü et al., 2013]. During the decompression phase, there is no significant shift until 3 GPa, the last

point at ambient pressure being at $70 \pm 3 \text{ cm}^{-1}$. After the compression / decompression cycle, the low frequency band shifts of approximately 7 cm^{-1} (+ 10 %) from its initial position, indicating an irreversible change in the structure which could be explained by smaller polyhedra. This hysteresis may imply coordination changes in the structure, the respective polyhedra population may then be evolving through pressure.

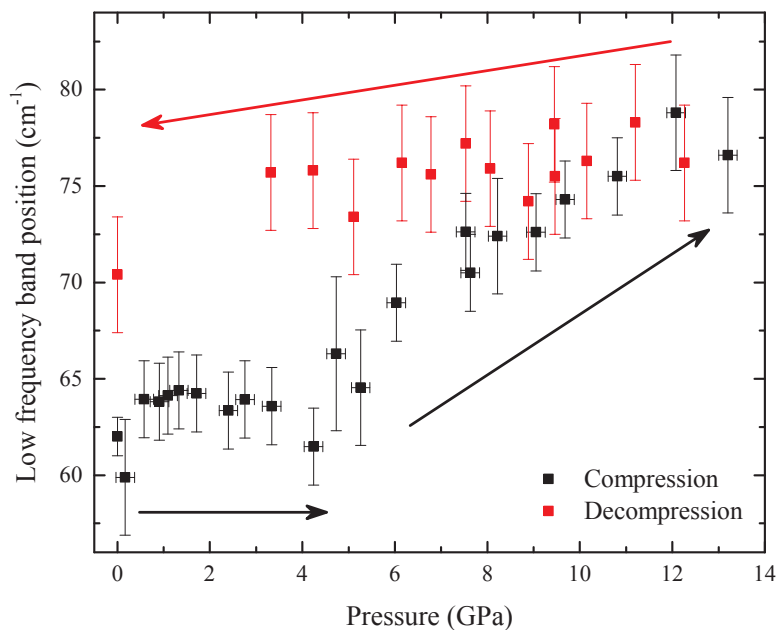


Figure 3.14 – Low frequency band position evolution with pressure for amorphous Ta_2O_5 . This band was attributed to Tantalum atoms vibrations in their oxygen cages, and may be convoluted with a Boson peak.

Figure 3.15 presents the evolution of the main band with pressure, corresponding to the different vibrational modes implying oxygen atoms motions. At first, the band shifts towards higher frequencies with the pressure increase, which can be linked to a bond shortening [Lü et al., 2013], and to a reorganization of the polyhedra. Around 5 GPa, as for the low frequency band, a sudden change occurs with the band position back to a lower frequency. No significant evolution happens when the pressure increases from 6.5 GPa to 13.2 GPa with the position around 680 cm^{-1} . This plateau can be explained by the impossibility of the polyhedra to reorganize more than the position they reached. The evolution inside the polyhedra may be more important at this point, highlighted by the fast shift of the low frequency band towards higher frequencies.

When the pressure decreases, a slight shift towards higher frequencies occurs down to 10.5 GPa, preceding a fast displacement towards lower frequencies down to 5 GPa.

For the decompression phase lower than 5 GPa, the band position shows no significant evolution with a frequency around 660 cm^{-1} .

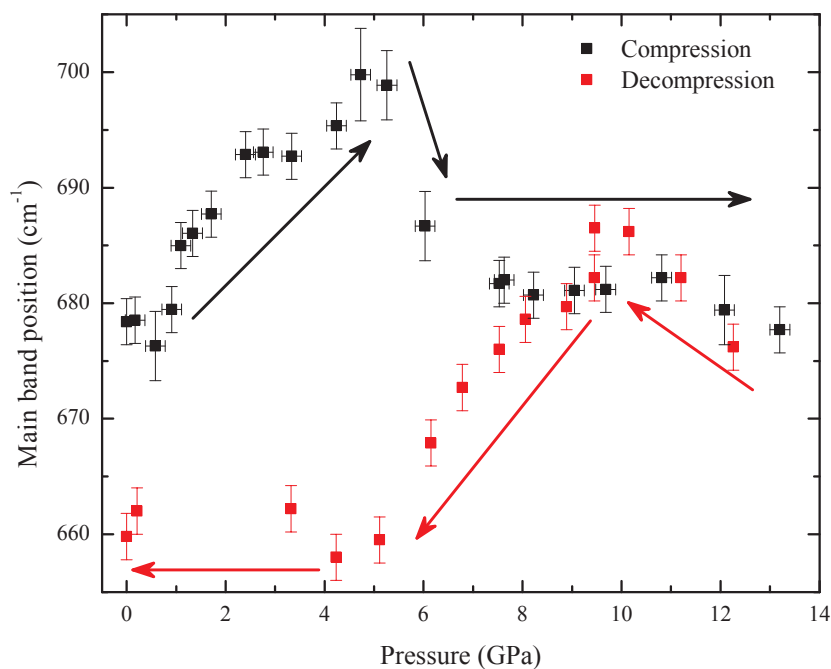


Figure 3.15 – Main band position evolution with pressure for amorphous Ta_2O_5 .

A few studies showed that a break in the evolution of the main band position could come from a coordination number change. Filonenko et al. showed in crystalline V_2O_5 , which presents a similar structure than Ta_2O_5 , a coordination number change from 5 to 6 with increasing pressure [Filonenko et al., 2004]. The 5-fold vanadium atoms form a squared pyramid with the vanadium at the center of the polyhedra. When pressure is applied, the vanadium atom shifts towards the base of the pyramid (see fig. 3.16), allowing bonding with an oxygen atom and forming then a 6-fold structure [Grzechnik and Supe, 1998]. In an other glass, the LaBGeO_5 oxide, the Raman feature attributed to anti-symmetric stretching of M-O bonds (the M corresponding to four-fold coordinated boron and germanium atoms) evolves in the same way under pressure as the main band in Ta_2O_5 . Indeed, with applied pressure, the band shifts towards higher frequencies, with a slope inversion around 7.5 GPa, to finally form an hysteresis after decompression. A coordination number change of the GeO_4 units into GeO_6 , seen by XANES, explains the sudden change in the bands evolution [Coussa-Simon et al., 2010].

The comparison with other glasses leads us to think that for amorphous tantalum pentoxide, a coordination number change is happening around 5 GPa. The polyhedra reorganize themselves (figure 3.17) below 5 GPa, which could correspond to the coordination number of the oxygen atoms slowly evolving from O-2Ta to O-3Ta. At higher pressure, the evolution of the structure is more important inside the polyhedra. The re-

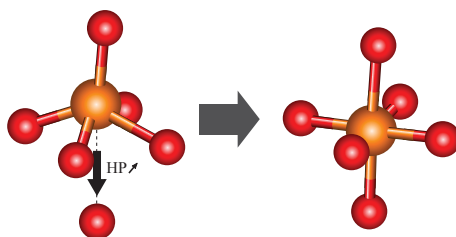


Figure 3.16 – The Vanadium atom shifts towards the base of the pyramid when pressure is applied, allowing bonding with an oxygen atom. Coordination number then changes from 5 to 6 for the Vanadium atom.

organization of the polyhedra structure could be correlated with a coordination number evolution from TaO_5 to TaO_6 , and later on from TaO_6 to TaO_7 . Moreover, simulations done at the ILM by T. Damart indicated a slow progression of the O-2Ta into O-3Ta during compression, in addition to a decrease of the TaO_5 in favor to the TaO_6 and TaO_7 polyhedra. These simulations corroborates the assumptions made previously. EXAFS measurements should be performed to experimentally back up these hypothesis.

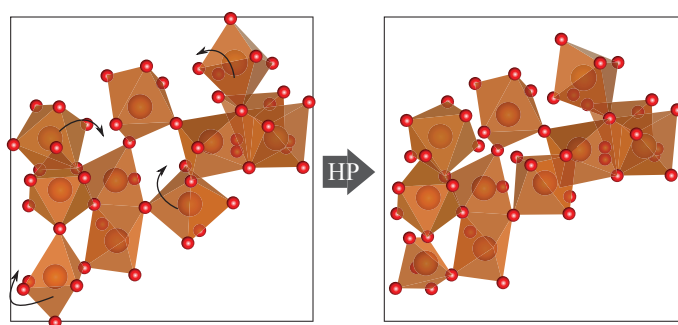


Figure 3.17 – With pressure increasing, the polyhedra reorganizes themselves so that the structure gets more compact.

The evolution of the Brillouin peak position as a function of pressure is shown on Figure 3.18, presenting a similar evolution than the low frequency band in Raman spectroscopy. No significant evolution can be seen during the compression up to 5 GPa. Then the Brillouin peak is shifting towards higher frequencies until a 40 % displacement at 14 GPa. During the decompression, the position of the peak shifts back to lower frequencies, to reach an irreversible 6 % final shift (from 36.5 ± 0.1 GHz to 38.8 ± 0.1 GHz). With Raman spectroscopy, the final spectra from compression / decompression cycles up to 13.2 GPa and 14.9 GPa are similar. This may indicate that we reached the densest ex-situ structure. The final shift of the Brillouin peak for Ta_2O_5 is about 6 % from its initial position. This value is quite small compared to the maximum shift for silica glass, around 25 %, and vitreous germanium oxide, around 20 %. This could be explained by

a more rigid structure of sputtered amorphous tantalum pentoxide.

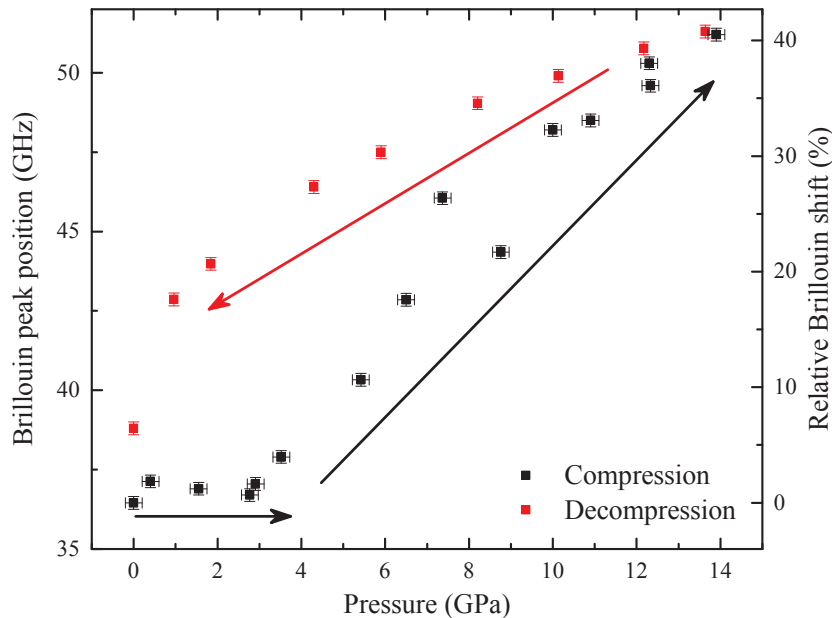


Figure 3.18 – Brillouin peak evolution with pressure for amorphous Ta_2O_5 .

As the structure of Ta_2O_5 is not clear yet, and in order to further interpret the high-pressure behavior of a- Ta_2O_5 , the same high pressure experiments was conducted on crystalline Ta_2O_5 . In situ Raman spectra presenting the evolution of the sample are shown on Figure 3.19. The initial spectrum and the decompressed one are similar, implying an elastic deformation of the structure for applied pressure lower than 14.9 GPa. During compression, the spectrum seems to evolve towards an amorphous structure, with the two doubled bands at low frequencies and around the main band trying to merge together, added to the bands between 200 and 400 cm^{-1} decreasing in intensity. The evolution of the spectra towards amorphous signatures is in agreement with Lü et al., 2013, Li et al., 2014, who both described a total amorphization of crystalline tantalum pentoxide induced by pressure around 19 GPa.

Figure 3.20 presents the evolution of the two low frequency bands with pressure up to 14.9 GPa. Both bands present two regimes during compression. The band at 70 cm^{-1} evolves from the beginning, shifting towards higher frequencies. Around 5 GPa, the evolution pace slows down, while the band is still shifting. The band at 100 cm^{-1} however, does not evolve until 5 GPa, and then shifts towards lower frequencies. Both signatures evolve towards a merging.

The evolution with pressure of the two peaks of the main bands is presented on Fig-

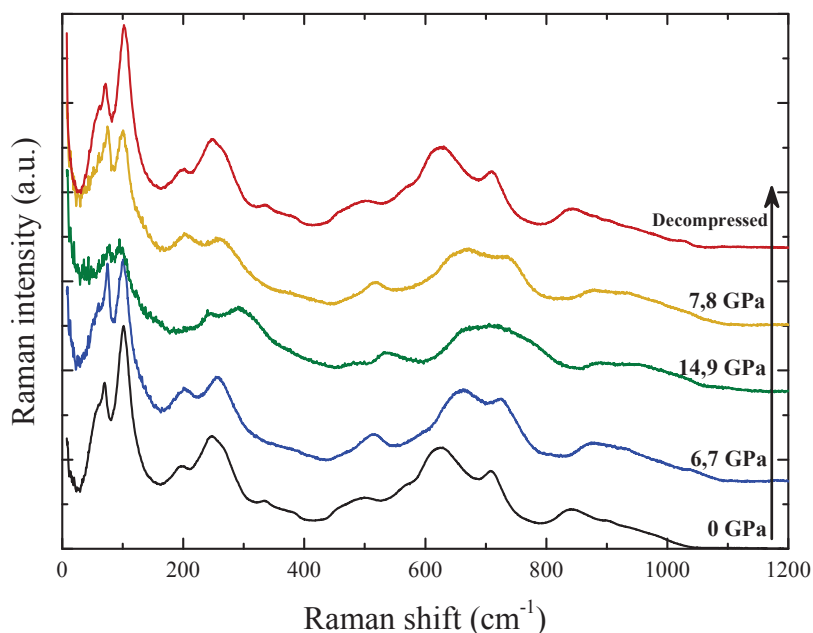


Figure 3.19 – In situ Raman spectra of crystalline Ta_2O_5 during compression up to 14.9 GPa and decompression.

ure 3.21. Both bands shift monotonically towards higher frequencies when pressure is applied, with a slower pace for the 700 cm^{-1} signature. No band position could be extracted from Raman spectra for pressure higher than 8.5 GPa. Indeed, the bands are merging together and the form of the poorly defined band could not be linked to a position (as can be seen on figure 3.19, at 14.9 GPa).

In Chapter 3.1, the low frequency features were assigned to the Tantalum atoms movement in their oxygen cages. The spectroscopic features between 600 cm^{-1} and 800 cm^{-1} were also linked to O-2Ta and O-3Ta rocking, stretching and bending modes.

During the high pressure experiment, an isotropic pressure is applied on the samples. If we consider the $\beta\text{-Ta}_2\text{O}_5$ structure from [Lü et al., 2013], this implies as much pressure on the b axis (see fig. 3.1, polyhedra connected by one oxygen) than along the a and c axis (polyhedra linked by one or two oxygen atoms). The pressure applied on the b axis induces a shrinking of the polyhedra, highlighted by the evolution of the low frequency signatures. Along the a and c axis, polyhedra have more space to reorganize. Under pressure the O-2Ta and O-3Ta bonds shorten and evolve towards a more condensed structure, as shown by the monotonic evolution of the bands between 600 cm^{-1} and 800 cm^{-1} .

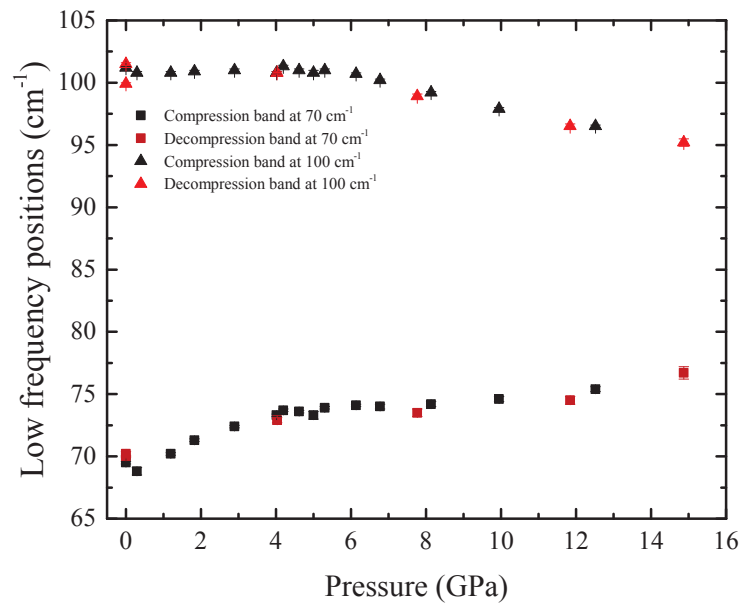


Figure 3.20 – In situ positions of the doubled low frequency signatures following compression up to 14.9 GPa and decompression cycles. Error bars are within the size of the points.

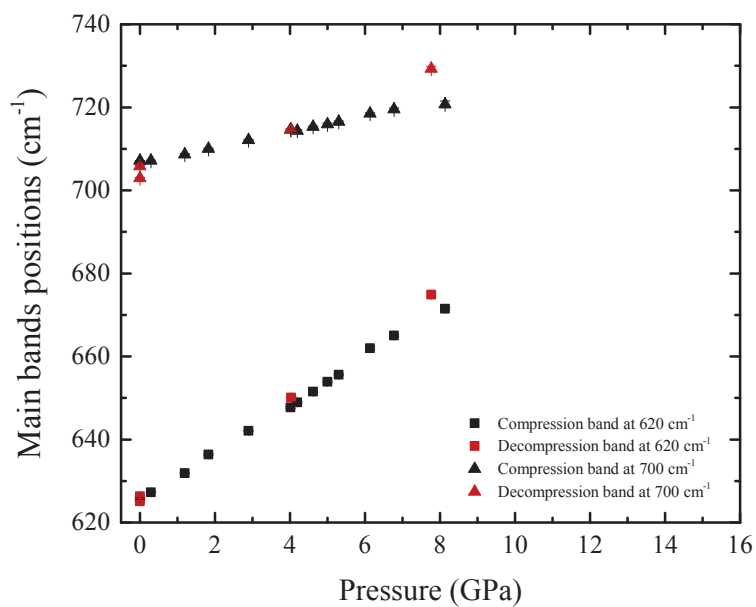


Figure 3.21 – In situ positions of the doubled main band signatures following compression up to 14.9 GPa and decompression cycles. At higher pressure than 8 GPa, the two bands are too close for their position to be extracted.

From high pressure experiments, the elastic limit of amorphous Ta_2O_5 was found between 4 GPa and 7 GPa. A coordination number change from TaO_5 to TaO_6 , and from TaO_6 to TaO_7 , may begin around 5 GPa. EXAFS measurements are needed to support these hypothesis. Brillouin measurements support the assumption of a maximum densification ratio lower than 15%. Amorphous Tantalum pentoxide presents then a densification ability lower than fused silica glass. Opposed to the evolution of the amorphous structure, crystalline Ta_2O_5 presents a pure elastic behavior below 15 GPa, with a reorganization between the polyhedra and a shrinking of the polyhedra themselves.

3.5 TiO₂ doping

As seen earlier, the high-refractive index material used for the Bragg mirrors of the GW detector is TiO₂-doped Tantalum pentoxide. Earlier studies shows that a 25% titania doping induces a decrease of the layers mechanical losses about 20% lower than pure tantalum pentoxide layers, while keeping the low absorption properties [Harry et al., 2007, Cimma et al., 2006, Comtet et al., 2007]. A more recent study showed via classical molecular dynamics simulations, that a 62 % Titania doping gives the lowest mechanical losses [Trinastic et al., 2016]. This study shows that, at room temperature, the mechanical losses are linked to TLS transitions ($V = 350 - 550$ meV), involving around 130 atoms, and corresponding to oxygen rotations at medium range order .

The structure of pure titanium oxide will be described and compared to tantalum pentoxide. The mixed oxide structure will also be discussed with an analysis of the atomic concentrations. To explore the evolution of structure at medium range order as simulated by [Trinastic et al., 2016], the effect of the doping on the Raman spectra will be presented.

3.5.1 Structure

The structure of amorphous TiO₂ is similar to the one of amorphous Tantalum pentoxide [Pham and Wang, 2015]. Amorphous titanium oxide consists of a chain-like structure of mainly TiO₆ octahedra sharing edges or corners (Figure 3.22). The differences with amorphous Tantalum pentoxide comes from the coordination numbers of the oxygen atoms (Table 3.3). Indeed, around 80 % of the oxygen atoms are linked to three metal atoms in the case of titanium oxide, while in Ta₂O₅ the oxygen atoms are mostly linked to two tantalum atoms.

Titanium	%	Oxygen	%
Coord. 4	9	Coord. 2	6
Coord. 5	76	Coord. 3	83
Coord. 6	15	Coord. 4	11

Table 3.3 – Averaged coordination numbers for titanium and oxygen atoms in simulated amorphous TiO₂ [Pham and Wang, 2015].

Upon doping with titanium, the Ti atoms seem to replace the Tantalum atoms in the amorphous structure. This is possible as the Titanium atoms present approximately the same size than the Tantalum atoms, allowing a substitution of the Tantalum by a Titanium with increasing doping (Figure 3.23).

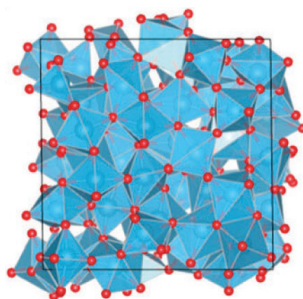


Figure 3.22 – Structure of amorphous TiO₂, obtained by melt-quenched simulation and after relaxation, using DFT [Pham and Wang, 2015]. Oxygen atoms are in red, Titanium atoms in blue.

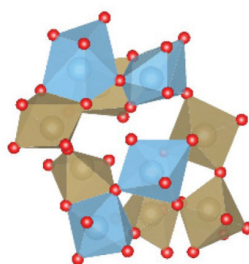


Figure 3.23 – Structure of amorphous TiO₂-doped Ta₂O₅, obtained by molecular dynamic simulation [Damart et al., 2016]. Oxygen in red, Titanium in blue and Tantalum in orange.

The coordination number for the standard mixed oxide, doped with 20% of TiO₂, is presented on table 3.4. These coordination numbers are closer to those of pure a-TiO₂ than the one simulated for pure a-Ta₂O₅. The inter-atomic distances are similar to the one of pure a-Ta₂O₅, with length values around 1.88 ± 0.02 Å for Ta-O, 3.12 ± 0.03 Å for Ta-Ta and 3.10 ± 0.03 Å for Ta-Ti distances [Bassiri et al., 2016]. The angle distribution is also close to the one of pure amorphous Ta₂O₅, as the intrapolyhedra angles are centered on 90° and 180° with a broadening of the distribution. The Ta-O-Ta and Ti-O-Ti angles evolve compared to pure Ta₂O₅, they are centered on 100° and 125°. The second value reflects the differences in Oxygen as they are mainly coordinated with three cations instead of two as in pure Ta₂O₅.

Raman spectra

[Trinastic et al., 2016] showed, via simulations, that the transitions characterizing the mechanical losses at room temperature happens at medium range order. To get insight in the medium range order and to begin the experimental analysis in parallel to the simulations conducted, Raman experiments were performed. Figure 3.24 presents the spectra of pure TiO₂ and pure Ta₂O₅ thin layers, both deposited by IBS. The Raman

Tantalum	%	Titanium	%	Oxygen	%
Coord. 4	1.1	Coord. 4	4.1	Coord. 2	33.6
Coord. 5	27.6	Coord. 5	45.0	Coord. 3	65.0
Coord. 6	68.7	Coord. 6	50.4	Coord. 4	1.2
Coord. 7	2.6	Coord. 7	0.5		

Table 3.4 – Coordination numbers for tantalum, titanium and oxygen atoms in simulated amorphous Ta₂O₅ doped with 20 % of TiO₂ [Damart et al., 2016].

spectra present some similarities, both presenting two large bands with a shoulder on the side of the high frequency band (called the main band as previously done for the Ta₂O₅ analysis). The a-TiO₂ spectrum is also similar to TiO₂ sol-gel Raman spectrum (previous to any annealing) [Bahtat, 1996]. No clear attribution of the spectroscopic features of amorphous TiO₂ was found in the litterature, except as compared to the crystalline structures with a crystallographic attribution [Fischer, 2016]. As the structures are similar between the two considered oxides, we will base the interpretation of the spectroscopic features of TiO₂ on the band attribution of Ta₂O₅. Then, the main band and its shoulder will be considered as O-2Ti, O-3Ti and O-4Ti bending, stretching and rocking modes. The low frequency band will be attributed to Ti atoms motion in their oxygen cage. The latter is justified by the molecular dynamics simulations, as the frequency of the Ti movements ($8.5 \text{ THz} = 280 \text{ cm}^{-1}$) corresponds to the position of the band [Damart et al., 2016].

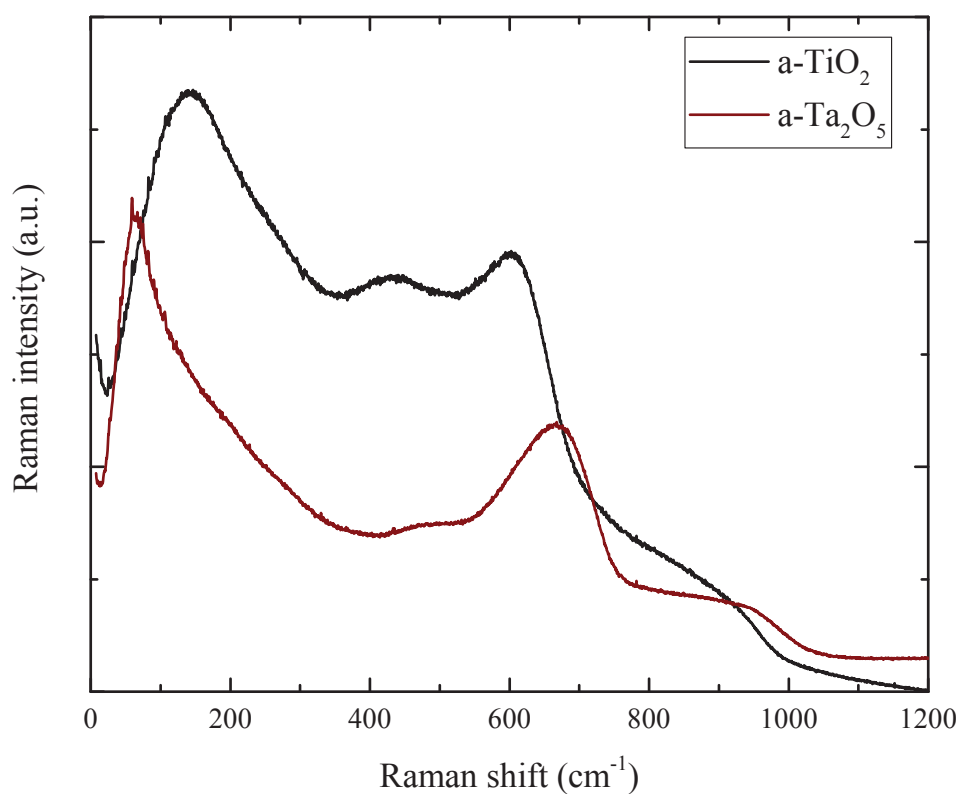


Figure 3.24 – Raman spectra of crystalline anatase form of Ta₂O₅, amorphous TiO₂ and amorphous Ta₂O₅.

3.5.2 Doping effect

To study the effect of Titania doping on the structure, six samples with different doping were processed in the Grand Coater. On these six samples, one is pure Ta₂O₅, four are Ta₂O₅ containing an increasing content of TiO₂, and the last one is pure TiO₂. The samples thicknesses vary between 500 and 1300 nm (see Table 3.5).

Their elemental composition was quantitatively analyzed by RBS spectra, and results are discussed in the following part. Then the evolution of the structure with increasing TiO₂ concentration will be presented via vibrational spectroscopy results.

Rutherford Backscattering Spectroscopic measurements

As presented in Chapter 1.6, RBS allows the analysis of the chemical composition of thin layers. The measurements were conducted twice on each sample with two different beam energies : 2.50 MeV and 3.00 MeV. This kind of spectroscopy is extremely precise to quantify heavy atoms, however, the analysis of oxygen is more difficult as the error bars are quite high for this element.

Figure 3.25 compares two spectra acquired at two beam energies for the same sample with an intermediate concentration of Titania. As can be seen, different energies induce different band widths and different calibrations (equivalence between channel and energy of the back-scattered particles). The intensity (counts) of the signal also differs depending on the incident particles energy. From simulation [Mayer et al., 1999], 15.1 ± 0.4 % of Tantalum atoms are present in this Doped 3 layer, 12 ± 2 % of Titanium, 3 ± 2 % of Argon and 70 ± 5 % of Oxygen. The oxygen signal presents a step at the surface of the sample, which may correspond to an excess of this element at the surface of the layer, over approximately 70 nm.

From the atomic concentration, the molecular concentration can be deduced by attributing 2 oxygen atoms to one titanium and 5 oxygen to one tantalum. This simple calculation gives 53 ± 2 % Ta₂O₅ and 35 ± 3 % TiO₂. The concentrations in TiO₂ are also estimated at the LMA considering a linear evolution of the refractive index at a given wavelength, compared to the concentration of elements in the layers. The concentrations found via RBS are similar to these estimated at the LMA, considering the presence of Argon in the layers and the large error bars on the oxygen content.

As the analysis is the same between 2.50 MeV and 3.00 MeV, only the spectra of each sample acquired with an energy beam at 3.00 MeV are presented on Figure 3.26. The measurements at this energy allows a better separation between the Ti and Ta signals.

As some samples are thicker than others, a superposition of the Ti and Ta signals can be observed between the channels 1250 and 1400, for the samples Doped 1 and 4. As for the sample Doped 3 presented on Figure 3.25, every layer presents an excess

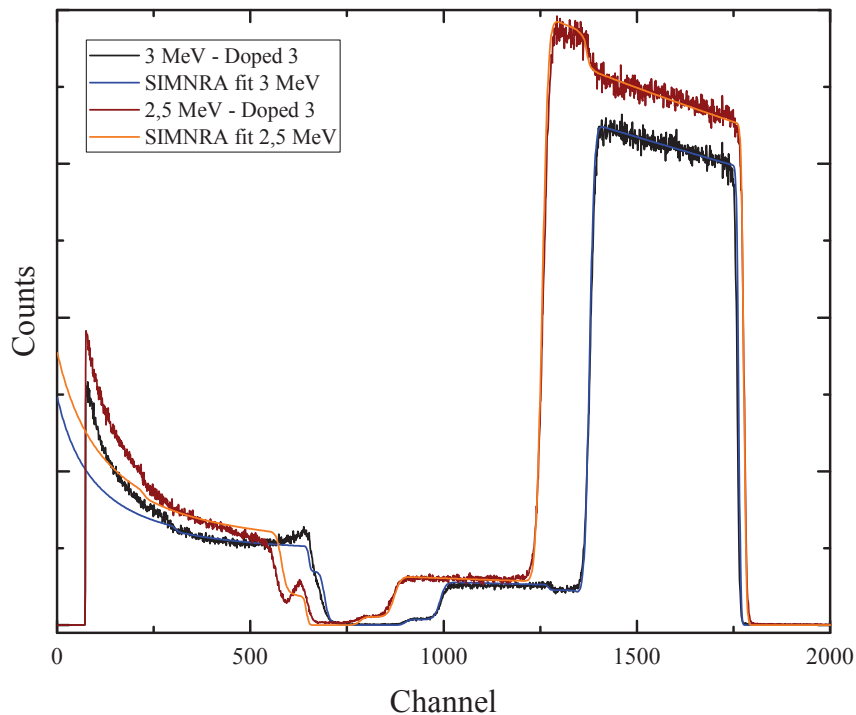


Figure 3.25 – RBS spectra of the Doped 3 sample obtained at 2.50 MeV and 3.00 MeV. The lines in blue and orange correspond to the fit calculated with SIMNRA [Mayer et al., 1999], with 15% of Ta atoms, 12% of Ti, 3% of Ar, 7% of O, and 6800 At/cm² in both cases.

of Oxygen at the surface. Table 3.5 summarizes the concentrations obtained for every composition. The simulated concentrations found via RBS measurements correspond to the one measured at LMA via the refractive index. The standard doping presented in the table corresponds to the composition of the VIRGO and LIGO mirrors. The RBS spectrum of this sample is not presented on Figure 3.26 as the measurements were only conducted at 2.50 MeV for this particular layer.

From the concentrations of each layers, the structure can now be analyzed via Raman spectroscopy. The composition values used in the following part are corresponding to the LMA percentages.

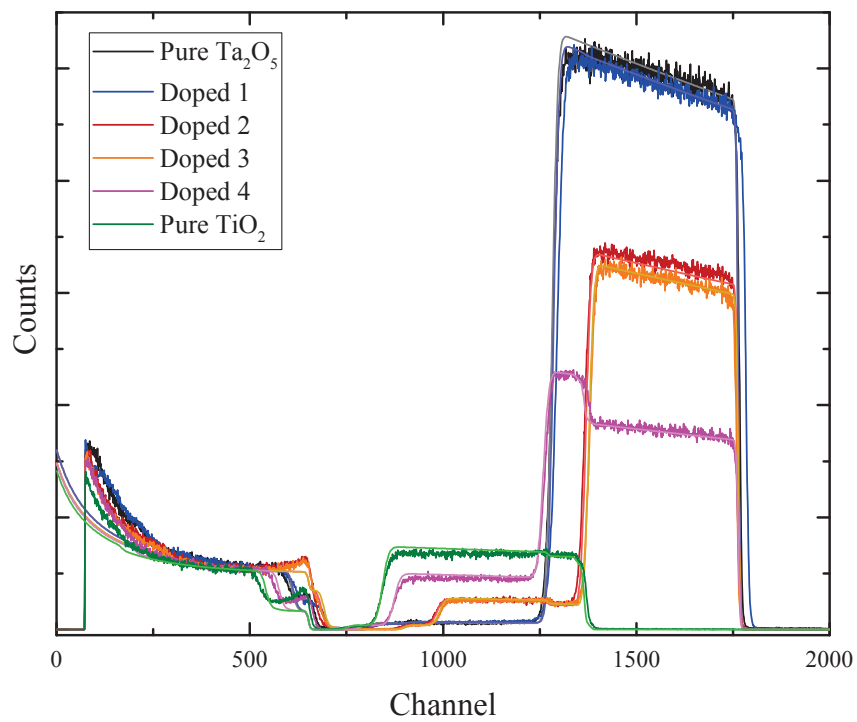


Figure 3.26 – RBS spectra of all the samples obtained at 3.00 MeV for 500 000 counts. The lighter color fits are simulated by SIMNRA for the corresponding measurement conditions and allow the extraction of the layers' compositions and densities.

Sample	Thickness (nm)	[TiO ₂] _{LMA} (%)	[atomic] _{RBS} (%)	[Ta ₂ O ₅] _{RBS} [TiO ₂] _{RBS} (%)	Density (g·cm ⁻³)	C ₁₁ (GPa)
Pure Ta ₂ O ₅	1081	0	Ta : 25.9 ± 0.7 O : 69 ± 5 Ar : 5 ± 2	Ta ₂ O ₅ : 91 ± 3 TiO ₂ : 0	7.3 ± 0.3	171 ± 10
Doped 1	1084	8.3	Ta : 25.5 ± 0.5 Ti : 1.0 ± 0.5 O : 69 ± 7 Ar : 4 ± 2	Ta ₂ O ₅ : 89 ± 2 TiO ₂ : 3 ± 2	7.3 ± 0.3	170 ± 10
Std doping	514	20	Ta : 22.2 ± 0.7 Ti : 6 ± 0.6 O : 68 ± 5 Ar : 3 ± 2	Ta ₂ O ₅ : 78 ± 3 TiO ₂ : 18 ± 2	6.7 ± 0.3	
Doped 2	939	40.2	Ta : 15.7 ± 0.3 Ti : 12.0 ± 1.5 O : 69 ± 7 Ar : 4 ± 2	Ta ₂ O ₅ : 55 ± 2 TiO ₂ : 36 ± 5	6.7 ± 0.3	188 ± 10
Doped 3	913	43.7	Ta : 15.1 ± 0.4 Ti : 11.5 ± 1.5 O : 70 ± 5 Ar : 3 ± 2	Ta ₂ O ₅ : 53 ± 2 TiO ₂ : 35 ± 3	6.7 ± 0.3	186 ± 10
Doped 4	1204	70.7	Ta : 8.2 ± 0.2 Ti : 20.5 ± 1.5 O : 68 ± 5 Ar : 3 ± 2	Ta ₂ O ₅ : 29 ± 1 TiO ₂ : 62 ± 5	5.6 ± 0.3	176 ± 10
Pure TiO ₂	1280	100	Ti : 32 ± 1 O : 65 ± 5 Ar : 3 ± 2	Ta ₂ O ₅ : 0 TiO ₂ : 96 ± 3	3.5 ± 0.3	163 ± 10

Table 3.5 – Description of the doped samples. Thicknesses are measured via ellipsometry (LMA). The atomic and molecular concentrations are measured by RBS, the density is retrieved from the SIMNRA simulations via equation 1.47 [Mayer et al., 1999].

Raman measurements

Raman measurements were conducted to look at the evolution of the structure with doping. Raman spectra of each as-deposited (not annealed) sample are presented on Figure 3.27. The spectra seem to be evolving in a monotonous shift between the features of a Ta₂O₅ structure and the TiO₂ one.

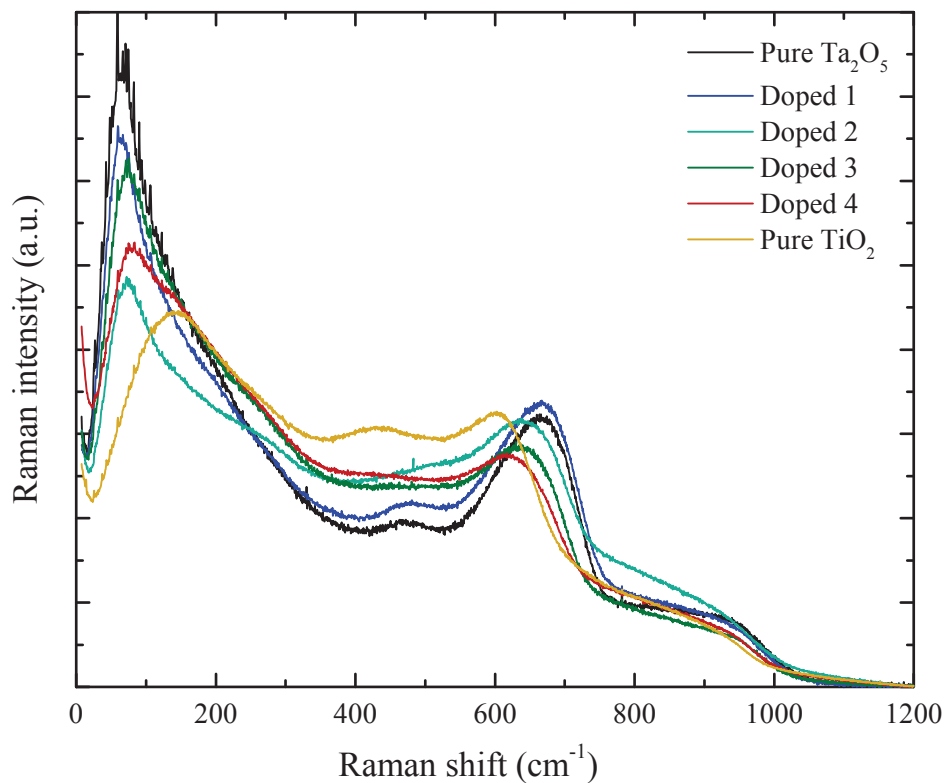


Figure 3.27 – Raman spectra of not annealed pure Ta₂O₅ (black), pure TiO₂ (yellow) and doped samples, normalized by the total area.

The evolution of the positions of the Low Frequency band and of the Main Band depending on the concentration of Titania are displayed on Figure 3.28. The Low frequency band does not vary much except when the proportion of Titanium atoms is higher than the Tantalum atoms. The Main Band position is monotonically evolving with the TiO₂ content, and seems to be a suitable signature of this concentration.

The Brillouin shift was also measured for these samples. With the addition of Titanium atoms to the structure, the Brillouin peak is shifting towards higher frequencies with a nonlinear behavior. From the position of this peak and the densities simulated via the RBS results, the elastic coefficient c_{11} can be evaluated with the equation 1.28 (cf

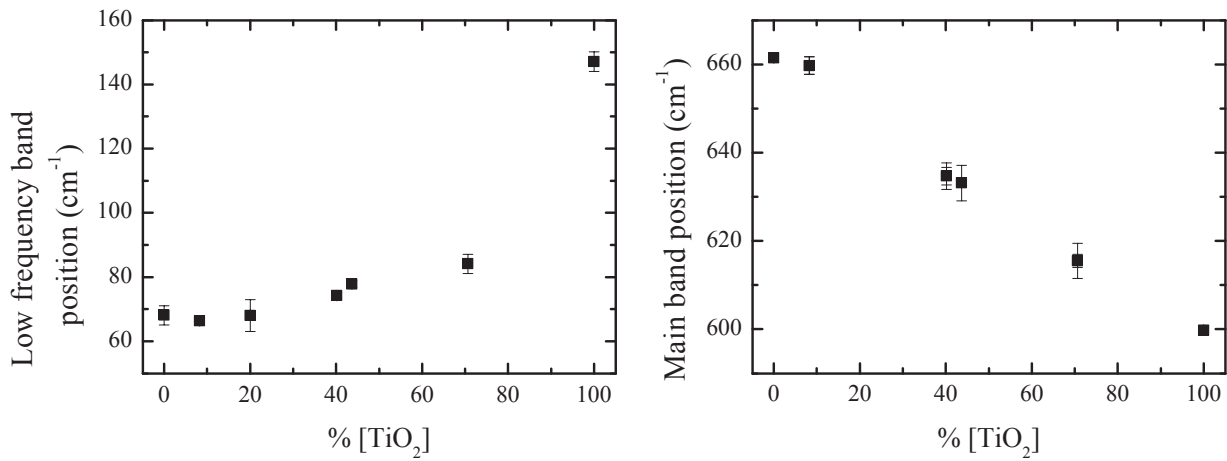


Figure 3.28 – Evolution of the low frequency band and Main band position depending on the TiO₂ content for the not annealed layers.

Table 3.5). The elastic constant of these glasses present no evolution between the two pure structures, even if the density shows a 50% decrease.

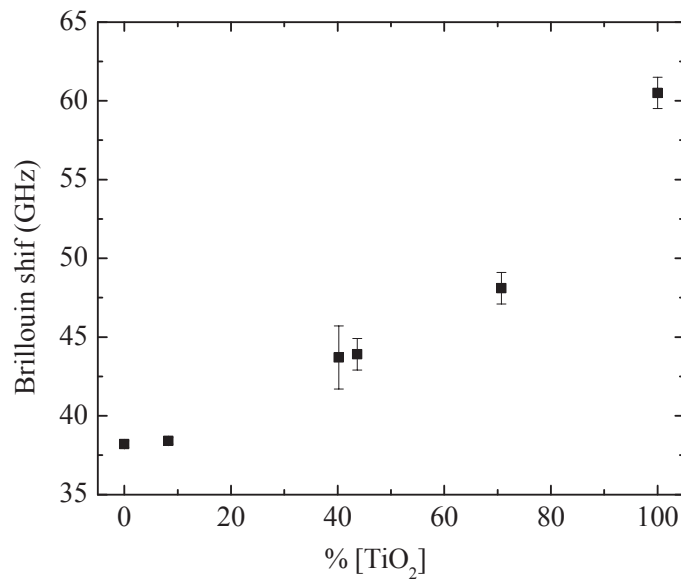


Figure 3.29 – Evolution of the Brillouin shift depending on the TiO₂ content for the not annealed layers.

As for SiO₂ and Ta₂O₅ layers, doped thin films were annealed during 10 hours at $T_a=500\text{ }^\circ\text{C}$. The Raman spectra of the annealed samples (figure 3.30) were acquired on the disk resonator used to measure the mechanical losses, implying thicknesses two times lower than for the non-annealed samples. Due to the smaller thicknesses, the silica substrate signal is visible on every spectra with the main band appearing between 400 and 550 cm^{-1} . The structure of the amorphous TiO₂ seems to be less stable than the doped and Ta₂O₅ samples. Indeed, the pure TiO₂ sample presents a crystalline spectrum after annealing, corresponding to the anatase polymorph of crystalline Titania. To conserve the amorphous structure, a lower annealing temperature may be needed for this oxide.

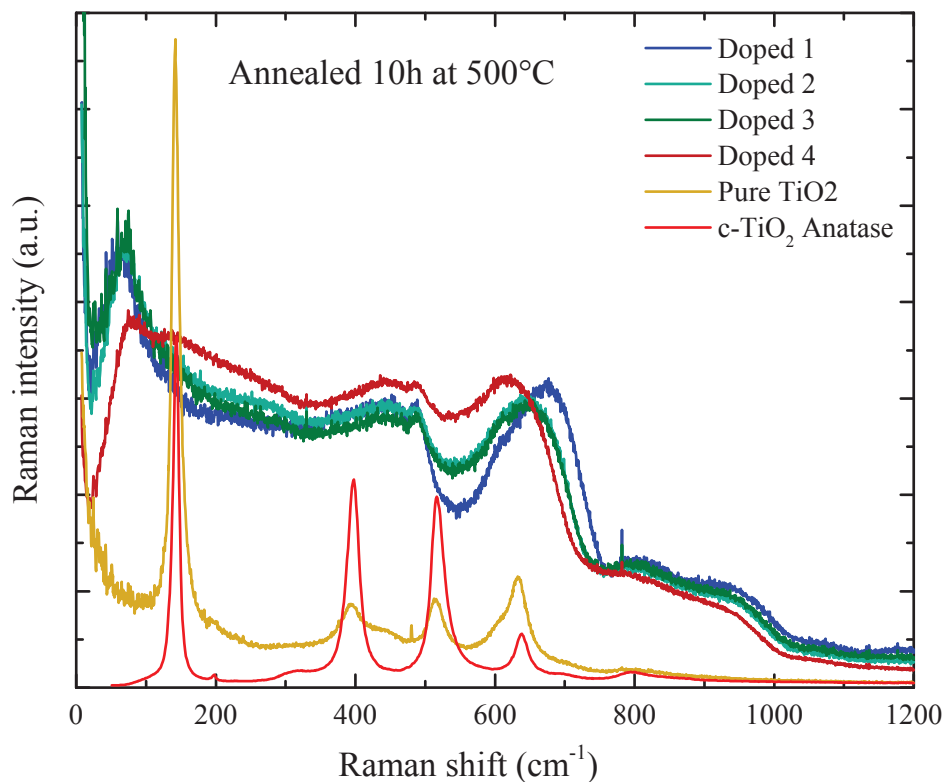


Figure 3.30 – Raman spectra of pure TiO₂ (yellow) and doped samples annealed during 10 hour at $T_a=500\text{ }^\circ\text{C}$, normalized by the total area.

The evolution of the band positions (Figure 3.31) is quite similar to the one of as-deposited samples. The only exception coming from the last composition, pure TiO₂, which is crystallized. The main band is also linearly correlated with the Titania content except for the crystallized sample as expected. The low frequency positions also exhibits

a non-linear behavior due to the crystallized sample.

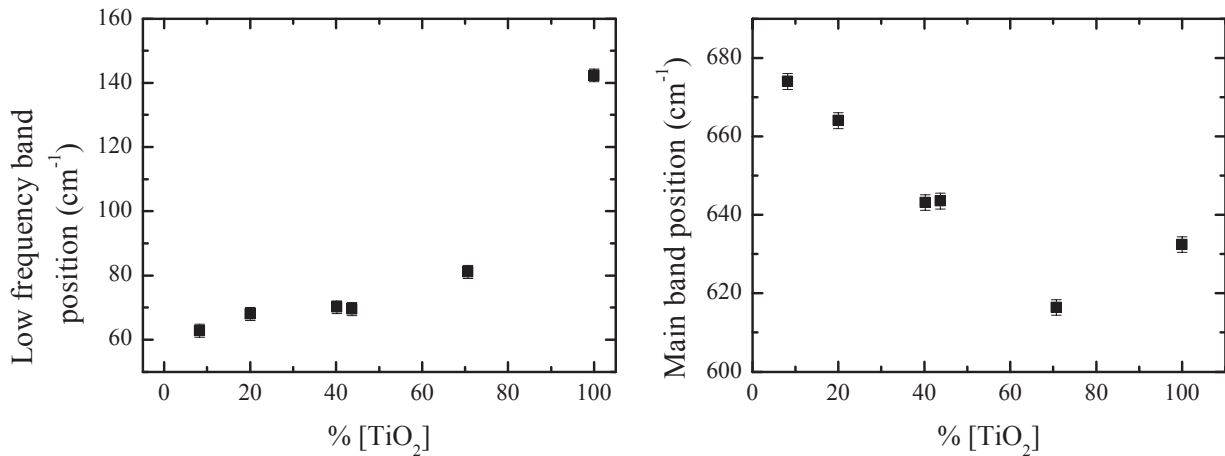


Figure 3.31 – Evolution of the low frequency band and Main band position depending on the TiO₂ content for samples annealed 10 hours at T_a=500 °C.

Figure 3.32 presents the mechanical losses of each annealed sample. The lowest point corresponds to the standard doping used for the mirrors. The 100% doped sample (pure TiO₂) presents mechanical losses 1.5 times higher than other samples. As previously observed on the Raman spectrum, the sample crystallizes during the annealing process explaining the higher losses. The samples at higher Titania doping than the standard one also present lower losses than pure Tantalum oxide, highlighting the effect of the doping. This is coherent with [Trinastic et al., 2016] who showed via molecular dynamics simulations that the lowest losses could be obtained through a 62 % doping.

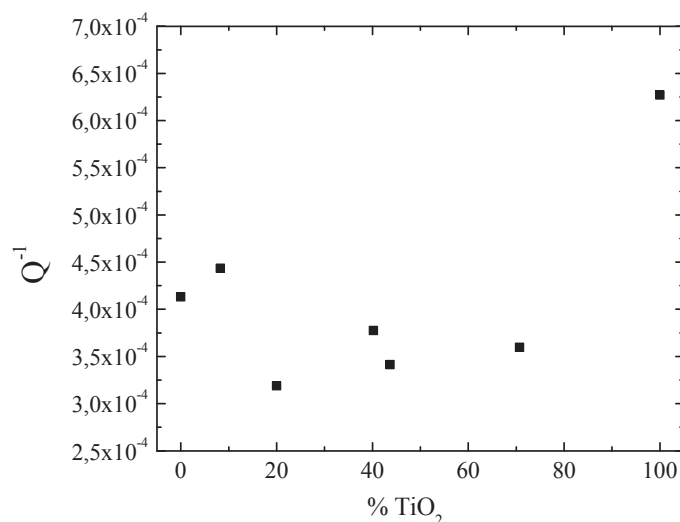


Figure 3.32 – Mechanical losses of each annealed (10 hours at T_a = 500 °C) doped coatings (from 0% to 100% TiO₂ content).

3.6 Conclusion

The Tantalum pentoxide layers present a complex amorphous structure, close to the crystalline one, with high cations coordination numbers. No evident evolution of the coatings structure was exhibited during annealing, opposite to the silica coatings. The layers crystallize easily even at low temperature $T_a = 650^\circ\text{C}$, indicating a unstable structure. High pressure experiments disclose a non-elastic behavior of the amorphous structure, with probably a coordination number change beginning around 5 GPa. EXAFS measurement will be needed to back up this hypothesis. Moreover, the elastic limit of $\alpha\text{-Ta}_2\text{O}_5$ was found to be between 4 and 7 GPa. To improve our knowledge of this oxide, the same high pressure measurements were conducted on a β polymorph of the crystalline structure. A linear evolution was found for all spectroscopic signatures, indicating a pure elastic behavior for this crystal in this pressure range.

Added to the exploration on the Tantalum pentoxide, the effect of the TiO_2 doping was also studied since the mechanical losses decrease with the addition of TiO_2 . The evaluation of the elemental concentrations of the layers, added to the spectroscopic measurements gave a calibration curve to evaluate the concentration of TiO_2 .

Bibliography

- [Alcalá et al., 2002] Alcalá, G., Skeldon, P., Thompson, G. E., Mann, A. B., Habazaki, H., and Shimizu, K. (2002). Mechanical properties of amorphous anodic alumina and tantalum films using nanoindentation. *Nanotechnology*, 13:451–455.
- [Aleshina and Loginova, 2002] Aleshina, L. A. and Loginova, S. V. (2002). Rietveld Analysis of X-ray Diffraction Pattern from β -Ta₂O₅ Oxide. *Crystallography Reports*, 47(3):460–464.
- [Bahtat, 1996] Bahtat, A. (1996). *Elaboration et étude spectroscopique de couches minces de TiO₂ optiquement guidantes : Role du dopage par les ions Eu³⁺ et Er³⁺*. PhD thesis, Université Claude Bernard Lyon 1.
- [Balachandran and Eror, 1982] Balachandran, U. and Eror, N. (1982). A study of the crystal structure of B-Ta₂O₅ by vibrational spectroscopy and X-ray diffraction. *Journal of Materials Science Letters*, 1:219–222.
- [Bassiri et al., 2016] Bassiri, R., Abernathy, M. R., Liou, F., Mehta, A., Gustafson, E. K., Hart, M. J., Isa, H. N., Kim, N., Lin, A. C., MacLaren, I., Martin, I. W., Route, R. K., Rowan, S., Shyam, B., Stebbins, J. F., and Fejer, M. M. (2016). Order, disorder and mixing: The atomic structure of amorphous mixtures of titania and tantalum. *Journal of Non-Crystalline Solids*, 438:59–66.
- [Bassiri et al., 2013] Bassiri, R., Evans, K., Borisenko, K. B., Fejer, M. M., Hough, J., MacLaren, I., Martin, I. W., Route, R. K., and Rowan, S. (2013). Correlations between the mechanical loss and atomic structure of amorphous TiO₂-doped Ta₂O₅ coatings. *Acta Materialia*, 61(4):1070–1077.
- [Bassiri et al., 2015] Bassiri, R., Liou, F., Abernathy, M. R., Lin, A. C., Kim, N., Mehta, A., Shyam, B., Byer, R. L., Gustafson, E. K., Hart, M., MacLaren, I., Martin, I. W., Route, R. K., Rowan, S., Stebbins, J. F., and Fejer, M. M. (2015). Order within disorder: The atomic structure of ion-beam sputtered amorphous tantalum (a-Ta₂O₅). *APL Materials*, 3:036103.
- [Cimma et al., 2006] Cimma, B., Forest, D., Ganau, P., Lagrange, B., Mackowski, J.-M., Michel, C., Montorio, J.-L., Morgado, N., Pignard, R., Pinard, L., et al. (2006). Ion

- beam sputtering coatings on large substrates: toward an improvement of the mechanical and optical performances. *Applied optics*, 45(7):1436–1439.
- [Comtet et al., 2007] Comtet, C., Forest, D., Ganau, P., Harry, G. M., Mackowski, J.-M., Michel, C., Montorio, J.-L., Morgado, N., Pierro, V., Pinard, L., et al. (2007). Reduction of tantala mechanical losses in Ta_2O_5/SiO_2 coatings for the next generation of VIRGO and LIGO interferometric gravitational waves detectors. In *42th Rencontres de Moriond-Gravitational Waves and Experimental Gravity*.
- [Coussa-Simon et al., 2010] Coussa-Simon, C., Martinet, C., De Ligny, D., Deschamps, T., Trapananti, A., and Champagnon, B. (2010). Permanent Ge Coordination Change Induced by Pressure in $La_2O_3\text{-}B_2O_3\text{-}GeO_2$ Glass. *Journal of the American Ceramic Society*, 93(9):2726–2730.
- [Damart et al., 2016] Damart, T., Coillet, E., Tanguy, A., and Rodney, D. (2016). Numerical Study of the Structural and Vibrational Properties of Amorphous Ta_2O_5 and TiO_2 -doped Ta_2O_5 . *Journal of Applied Physics*, 119(17):175106.
- [Deschamps, 2009] Deschamps, T. (2009). *Étude des déformations élastique et plastique des verres de silice et silico-sodo-calciques sous hautes-pressions hydrostatiques et indentation par spectrométrie Raman*. PhD thesis, Université Claude Bernard Lyon 1.
- [Deschamps et al., 2013] Deschamps, T., Kassir-Bodon, A., Sonnevile, C., Margueritat, J., Martinet, C., de Ligny, D., Mermet, A., and Champagnon, B. (2013). Permanent densification of compressed silica glass: a Raman-density calibration curve. *Journal of physics. Condensed matter*, 25(2):025402.
- [Dobal et al., 2000] Dobal, P. S., Katiyar, R. S., Jiang, Y., Guo, R., and Bhalla, a. S. (2000). Raman scattering study of a phase transition in tantalum pentoxide. *J Raman Spectrosc*, 31:1061.
- [Durben and Wolf, 1991] Durben, D. J. and Wolf, G. H. (1991). Raman spectroscopic study of the pressure-induced coordination change in GeO_2 glass. *Physical Review B*, 43(3):2355.
- [Filonenko et al., 2004] Filonenko, V. P., Sundberg, M., Werner, P.-E., and Zibro (2004). Structure of a high-pressure phase of vanadium pentoxide, $\beta - V_2O_5$. *Acta Crystallographica Section B*, B60:375–381.
- [Fischer, 2016] Fischer, D. (2016). Influence of substrate temperature and silver-doping on the structural and optical properties of TiO_2 films. *Thin Solid Films*, 598:204–213.

- [Grzechnik and Supe, 1998] Grzechnik, A. and Supe, Ä. N. (1998). Local Structures in High Pressure Phases of V_2O_5 . *Chemistry of Materials*, 10:2505–2509.
- [Guo and Robertson, 2015] Guo, Y. and Robertson, J. (2015). Comparison of oxygen vacancy defects in crystalline and amorphous Ta_2O_5 . *Microelectronic Engineering*, 147:254–259.
- [Harry et al., 2007] Harry, G. M., Abernathy, M. R., Becerra-Toledo, A. E., Armandula, H., Black, E., Dooley, K., Eichenfield, M., Nwabugwu, C., Villar, A., Crooks, D. R. M., Cagnoli, G., Hough, J., How, C. R., MacLaren, I., Murray, P., Reid, S., Rowan, S., Sneddon, P. H., Fejer, M. M., Route, R., Penn, S. D., Ganau, P., Mackowski, J.-M., Michel, C., Pinard, L., and Remillieux, A. (2007). Titania-doped tantala/silica coatings for gravitational-wave detection. *Classical and Quantum Gravity*, 24(2):405.
- [Joseph et al., 2012] Joseph, C., Bourson, P., and Fontana, M. D. (2012). Amorphous to crystalline transformation in Ta_2O_5 studied by Raman spectroscopy. *Journal of Raman Spectroscopy*, 43:1146–1150.
- [Landron et al., 2000] Landron, C., Hennet, L., Coutures, J.-p., Jenkins, T., Alétru, C., Greaves, N., Soper, A., and Derbyshire, G. (2000). Aerodynamic laser-heated contactless furnace for neutron scattering experiments at elevated temperatures. *Review of Scientific Instruments*, 71(4):1745.
- [Li et al., 2014] Li, Q., Zhang, H., Cheng, B., Liu, R., Liu, B., Liu, J., Chen, Z., Zou, B., Cui, T., and Liu, B. (2014). Pressure-induced amorphization in orthorhombic Ta_2O_5 : An intrinsic character of crystal. *Journal of Applied Physics*, 115(19):193512.
- [Lin et al., 1999] Lin, J., Masaaki, N., Tsukune, A., and Yamada, M. (1999). Ta_2O_5 thin films with exceptionally high dielectric constant. *Applied physics letters*, 74(16):2370–2372.
- [Lü et al., 2013] Lü, X., Hu, Q., Yang, W., Bai, L., Sheng, H., Wang, L., Huang, F., Wen, J., Miller, D. J., and Zhao, Y. (2013). Pressure-induced amorphization in single-crystal Ta_2O_5 nanowires: A kinetic mechanism and improved electrical conductivity. *Journal of the American Chemical Society*, 135(37):13947–13953.
- [Mayer et al., 1999] Mayer, M., Duggan, J. L., Stippec, B., and Morgan, I. L. (1999). SIM-NRA, a simulation program for the analysis of NRA, RBS and ERDA. In *AIP Conference Proceedings*, volume 475, pages 541–544. AIP.
- [Ono et al., 2001] Ono, H., Hosokawa, Y., Shinoda, K., Koyanagi, K., and Yamaguchi, H. (2001). Ta-O phonon peaks in tantalum oxide films on Si. *Thin Solid Films*, 381(1):57–61.

- [Pham and Wang, 2015] Pham, H. H. and Wang, L.-W. (2015). Oxygen vacancy and hole conduction in amorphous TiO_2 . *Phys. Chem. Chem. Phys.*, 17:541–550.
- [Rosales-Sosa et al., 2015] Rosales-Sosa, G. A., Masuno, A., Higo, Y., Inoue, H., Yanaba, Y., Mizoguchi, T., Umada, T., Okamura, K., Kato, K., and Watanabe, Y. (2015). High elastic moduli of a $54\text{Al}_2\text{O}_3 - 46\text{Ta}_2\text{O}_5$ Glass Fabricated via containerless processing. *Scientific reports*, 5:15233.
- [Rouxel et al., 2008] Rouxel, T., Ji, H., Hammouda, T., and Moréac, A. (2008). Poisson's ratio and the densification of glass under high pressure. *Physical Review Letters*, 100(22):225501.
- [Sahu and Kleinman, 2004] Sahu, B. R. and Kleinman, L. (2004). Theoretical study of structural and electronic properties of $\beta - \text{Ta}_2\text{O}_5$ and $\delta - \text{Ta}_2\text{O}_5$. *Physical Review B*, 69:165202.
- [Sonneville et al., 2012] Sonneville, C., Mermet, A., Champagnon, B., Martinet, C., Margueritat, J., de Ligny, D., Deschamps, T., and Balima, F. (2012). Progressive transformations of silica glass upon densification. *The journal of Chemical Physics*, 137:124505.
- [Stone et al., 2001] Stone, C. E., Hannon, A. C., Ishihara, T., Kitamura, N., Shirakawa, Y., Sinclair, R. N., Umesaki, N., and Wright, A. C. (2001). The structure of pressure-compacted vitreous germania. *Journal of Non-Crystalline Solids*, 293–295:769 – 775. 8th Int. Conf. on Non-Crystalline Materials.
- [Terao, 1967] Terao, N. (1967). Structure des oxides de tantale. *Japanese Journal of Applied Physics*, 6(1):21.
- [Trinastic et al., 2016] Trinastic, J. P., Hamdan, R., Billman, C., and Cheng, H.-P. (2016). Molecular dynamics modeling of mechanical loss in amorphous tantalum and titania-doped tantalum. *Physical Review B*, 93(1):014105.
- [Tsuchiya et al., 2011] Tsuchiya, T., Imai, H., Miyoshi, S., Glans, P.-a., Guo, J., and Yamaguchi, S. (2011). X-Ray absorption, photoemission spectroscopy, and Raman scattering analysis of amorphous tantalum oxide with a large extent of oxygen nonstoichiometry. *Physical Chemistry Chemical Physics*, 13:17013–17018.
- [Winborne et al., 1976] Winborne, D. A., Nordine, P. C., Rosner, D. E., and Marley, N. F. (1976). Aerodynamic Levitation Technique for Containerless High Temperature Studies on Liquid and Solid Samples. *Metallurgical Transactions B*, 7B:711–713.

- [Wu et al., 2011] Wu, Y.-N., Li, L., and Cheng, H.-P. (2011). First-principles studies of Ta_2O_5 polymorphs. *Physical Review B*, 83:144105.
- [Zachariasen, 1932] Zachariasen, W. H. (1932). The atomic arrangement in glass. *Journal of the American Chemical Society*, 54(10):3841–3851.
- [Zhou et al., 2005] Zhou, Y. L., Niinomi, M., Akahori, T., Fukui, H., and Toda, H. (2005). Corrosion resistance and biocompatibility of Ti–Ta alloys for biomedical applications. *Materials Science and Engineering: A*, 398(1):28–36.
- [Zhu et al., 2005] Zhu, Y., Yu, F., Man, Y., Tian, Q., He, Y., and Wu, N. (2005). Preparation and performances of nanosized Ta_2O_5 powder photocatalyst. *Journal of Solid State Chemistry*, 178:224–229.

Conclusion

During this work, the structure was explored of thin non-crystalline layers composed of SiO_2 , Ta_2O_5 and TiO_2 -doped Ta_2O_5 , in order to look for the micro-structural origin of mechanical loss, i.e. thermal noise.

The experiments conducted on silica highlighted the particular structure of Ion Beam Sputtered layers, being denser and over-stressed compared to fused silica. The Si-O-Si angle distribution is narrower and is centered on smaller angles than for fused silica, and the ring statistics is shifted towards small units, with a strong population of 3-membered rings. Fused silica presents extremely low mechanical losses compared to other materials. In order to lower the mechanical losses of the coatings, the fabrication of a structure as close as possible to fused silica is needed. Then, an analysis of the influence of the deposition parameters, and post-deposition annealing parameters, was conducted. A low intensity of the coating source was found to lower the internal stress of the layers. Post-deposition annealing also releases the internal stress even if $T_a \ll T_g$ and induces a structural relaxation. The same evolution was seen for layers with different deposition parameters. A rapid decrease of the 3-membered ring population happens during the annealing, coupled with an increase of the 4-membered ring population. The Si-O-Si angle distribution broadens, with a mean value increasing. These characteristics exhibit a structural evolution towards a fused silica structure. The 3-membered ring population is correlated with the mechanical losses. Correlation which still holds even when the coating deposition parameters are different. The close activation energies of the mechanisms at stake can explain this correlation.

The features one can observe at low frequency in the Raman spectra of silica coatings needs further investigations at low temperature. Indeed, around 5 cm^{-1} , [Wiedersich et al., 2001] performed Brillouin spectroscopic measurements at low temperature and they showed a signature of the relaxation mechanisms, being the origin of mechanical losses. Moreover, the effect of annealing can be explore in more details. If the annealing temperature increases, the stress and structural relaxation should happen more easily, with a final structure closer to fused SiO_2 . In the future, it would also be interesting to study the impact of the substrate temperature during the deposition process. Indeed, new results from [Queen et al., 2015] showed a strong impact of the deposition temper-

ature on the mechanical losses.

The structure of the second oxide composing the Bragg mirrors, Ta_2O_5 , is still not well known, for the amorphous configuration as much as for the crystalline one. Contrary to silica coatings, the annealing process does not impact much on the structural motifs depicted by the Raman spectra. The temperature may be too low to release internal stresses, but crystallization happens easily even at low temperature compared to the T_{fus} . High pressure measurements exhibit a pure elastic behavior of the crystalline Ta_2O_5 structure, below 14.9 GPa. Concerning the amorphous material, a break appears around 5 GPa in the evolution of the spectroscopic signatures. This break may be induced by a coordination change in the TaO_x polyhedra, EXAFS measurements are needed to back up this hypothesis. One limitation of the analysis done on this amorphous material comes from the unclear band attribution of the Raman spectrum. More simulations are needed to precisely attribute the vibrational modes seen with the spectroscopic techniques.

Upon doping by Titania, the Tantalum pentoxide coating structure stays similar, with the Ti atoms replacing the Ta atoms in the polyhedra. The analysis via Raman spectroscopy, compared to the concentrations estimation via RBS, introduced a calibration curve to estimate the TiO_2 concentration in the layers. The elastic coefficient does not evolve upon doping. The structure of pure TiO_2 crystallizes at lower temperature than pure Ta_2O_5 , indicating less stabilized layers. An analysis of the effect of annealing on the structure for different TiO_2 concentrations, compared to the mechanical losses, could be pursued in the future to complete this work. Moreover, a question stays open for this material, how the TiO_2 -doping does lower the mechanical losses compared to the pure amorphous Ta_2O_5 .

This work presents the first steps to look at the micro-structural origin of the mechanical losses. Different mechanisms seem to happen in each material. Further studies on other kinds of coatings presenting low mechanical losses, like Si_3N_4 , a-Si, ZrO_2 or HfO_2 , could improve our knowledge on these mechanisms.

Bibliography

- [Queen et al., 2015] Queen, D. R., Liu, X., Karel, J., Jacks, H. C., Metcalf, T. H., and Hellman, F. (2015). Two-level systems in evaporated amorphous silicon. *Journal of Non-Crystalline Solids*, 426:19–24.
- [Wiedersich et al., 2001] Wiedersich, J., Surovtsev, N., Novikov, V., Rössler, E., and Sokolov, a. (2001). Light scattering spectra of fast relaxation in silica and $\text{Ca}_{0.4}\text{K}_{0.6}(\text{NO}_3)_{1.4}$ glasses. *Physical Review B*, 64(6):1–15.

Appendix A

Band analysis

The analysis conducted in this work are based on the evolution of the Raman features under different parameters. The method to extract positions and relative area, for each samples, will be presented here.

A.1 Silica glass spectra

For this study, the positions of the spectroscopic features, along the relative area of the D_2 band were observed. The positions are obtained through a gaussian fit of the top of the considered bands. The relative area of the D_2 band corresponds to the area of this defect band (crossed on figure A.1), over the total area of the Main band, D_1 and D_2 bands, i.e. between 200 and 700 cm^{-1} . The baselines used to delimit these area are shown with the dashed lines.

The last signature analyzed on the Raman silica spectra is the the Half Width at Half Maximum (HWHM) of the Main Band. A line is drawn horizontally from the deep between the Boson peak and the Main band, delimiting the height of the Main Band. Then, the HWHM is measured on the left side of the band as shown by the arrow on figure A.1.

A.2 Amorphous Tantalum oxide spectra

Concerning the Ta_2O_5 spectra, the positions are also extracted via a Gaussian fit of the peak's heights. The area analyzed are the one notified by the dashed lines on figure A.2 : the low frequency area and the main band area. For comparison, these area are divided by the total area over the whole range of frequencies, from 10 to 1200 cm^{-1} .

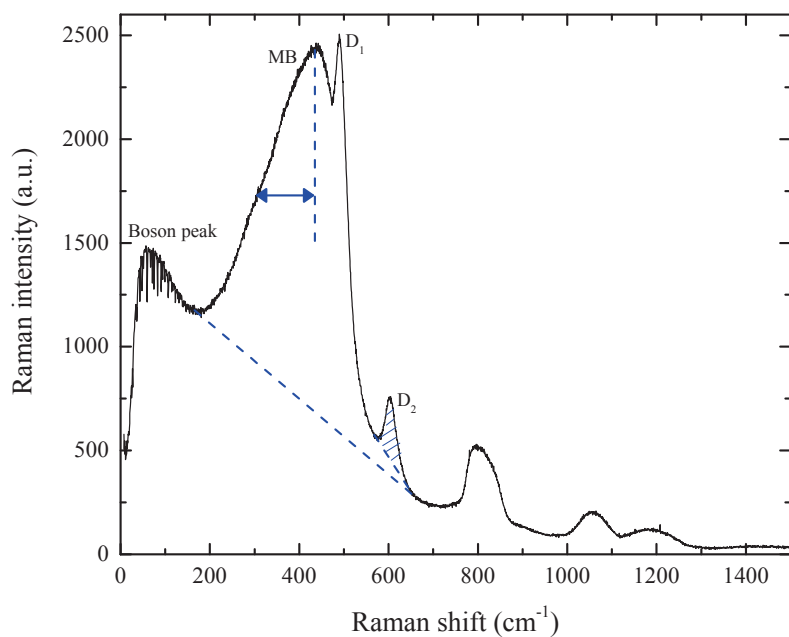


Figure A.1 – Fused silica Raman spectrum. The crossed area correspond to the D₂ area studied, the dashed lines to the limit of the area considered. The arrow indicates the HWHM measurement.

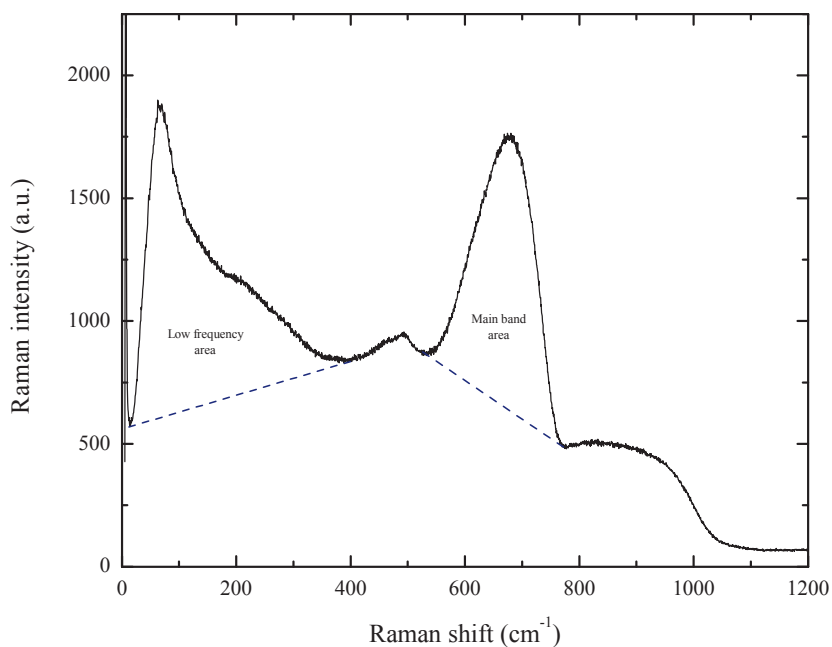


Figure A.2 – Amorphous Ta₂O₅ Raman spectrum. Dashed lines show the limits of the considered area.